Synaptic targets of photoreceptors specialized to detect color and skylight polarization in *Drosophila*

Emil Kind[1,*], Kit D. Longden[2,*], Aljoscha Nern[2,*], Arthur Zhao[2,*], Gizem Sancer[1,3], Miriam Flynn[2], Connor Laughland[2], Bruck Gezahegn[2], Henrique Ludwig[2], Alex Thomson[2], Tessa Obrusnik[1], Paula G. Alarcón[1], Heather Dionne[2], Davi D. Bock[2,4], Gerald M. Rubin[2], Michael B. Reiser[2,#], and Mathias F. Wernet[1,#]

1 : Instititut für Biologie – Abteilung Neurobiologie, Fachbereich Biologie, Chemie & Pharmazie, Freie Universität Berlin, Königin-Luise Strasse 1-3, 14195 Berlin, Germany.

2 : Janelia Research Campus, Howard Hughes Medical Institute, Ashburn, USA

3: Current address: Department of Neuroscience, Yale University School of Medicine, Sterling Hall of Medicine C-400, 333 Cedar Street, New Haven, CT 06510, USA.

4: Current address: Department of Neurological Sciences, University of Vermont, Burlington, VT 05405, USA.

* These authors contributed equally

Corresponding authors:

reiserm@janelia.hhmi.org

mathias.wernet@fu-berlin.de

Abstract

Color and polarization provide complementary information about the world and are detected by specialized photoreceptors. However, the downstream neural circuits that process these distinct modalities are incompletely understood in any animal. Using electron microscopy, we have systematically reconstructed the synaptic targets of the photoreceptors specialized to detect color and skylight polarization in *Drosophila*, and we have used light microscopy to confirm many of our findings. We identified known and novel downstream targets that are selective for different wavelengths or polarized light, and followed their projections to other areas in the optic lobes and the central brain. Our results revealed many synapses along the photoreceptor axons between brain regions, new pathways in the optic lobes, and spatially segregated projections to central brain regions. Strikingly, photoreceptors in the polarization-sensitive dorsal rim area target fewer cell types, and lack strong connections to the lobula, a neuropil involved in color processing. Our reconstruction identifies shared wiring and modality-specific specializations for color and polarization vision, and provides a comprehensive view of the first steps of the pathways processing color and polarized light inputs.

Introduction

Both the wavelength and the polarization angle of light contain valuable information that can be exploited by many visual animals. For instance, color gradients across the sky can serve as navigational cues, and skylight's characteristic pattern of linear polarization can also inform navigation by indicating the orientation relative to the sun (Heinze 2017; Figure 1A). The spectral content of light is detected by groups of photoreceptor cells containing Rhodopsin molecules with different sensitivities, often organized in stochastic retinal mosaics (Rister and Desplan 2011), and specialized, polarization-sensitive photoreceptors have been characterized in many species, both vertebrates and invertebrates (Nilsson and Warrant 1999). These two visual modalities, color and polarization vision, require the processing of signals over a wide range of spatial and temporal scales, and many questions remain about how the signals from functionally specialized photoreceptors are integrated in downstream neurons. Are color and polarization signal mixed at an early stage, or are they processed by different, modality-specific cell types? Do separate pathways exist that selectively process and convey information from photoreceptor types in the retinal mosaic to targets in the central brain? The full scope of the early synaptic stages of color and polarization circuitry is unknown in any animal, and the analysis of electron microscopy (EM) connectomes is ideally suited to exhaustively answer these questions, especially when corroborated with genetic labelling of cell types and circuit elements imaged with light microscopy. We make significant progress on the questions by mapping the neuronal connections of specialized, identified photoreceptors within the *Drosophila* Full Adult Fly Brain (FAFB) data set (Zheng et al. 2018) and validate many of these results by using the powerful genetic tools available in *Drosophila*.

While studies in many insects have contributed to the understanding of polarized light and color vision (Homberg 2015; Dacke and El Jundi 2018; Heinze 2017; Hempel de Ibarra et al. 2014), the visual system of *Drosophila* offers many advantages for the exploration of neural circuits (Wernet et al. 2014). Anatomical studies are facilitated by the stereotyped, repetitive structure of the optic lobes, with many cell types, the so-called columnar neurons, found in repeated circuit units, called visual columns, that are retinotopically arranged and

each correspond to one of the ~800 unit eyes (ommatidia) of the compound eye. Over one hundred optic lobe cell types have been described in classical Golgi work (Fischbach and Dittrich 1989), by more recent studies combining genetic labeling with light microscopy (Morante and Desplan 2008; Otsuna and Ito 2006; Wu et al. 2016; Nern et al. 2015) and, for some cell types, through EM reconstructions that have revealed not only cell morphologies but also detailed synaptic connectivity (Takemura et al. 2008, 2013, 2015; Meinertzhagen and O'Neil 1991; Rivera-Alba et al. 2011; Shinomiya et al. 2014). Furthermore, genetic tools (Jenett et al. 2012; Pfeiffer et al. 2008; Kvon et al. 2014; Dionne et al. 2018; Tirian and Dickson 2017), and, most recently, gene expression data (Davis et al. 2020; Konstantinides et al. 2018; Ozel et al. 2021; Kurmangaliyev et al. 2020) are available for many optic lobe cell types. An enabling feature of this emerging body of work is that in nearly all cases, distinct cell types can be reliably identified across data sets, such that new studies often directly enrich prior ones.

Each *Drosophila* ommatidium contains eight photoreceptors whose output is processed in a series of neuropils called the lamina, medulla, lobula and lobula plate that together form the optic lobes of the fly (Fischbach and Dittrich 1989). Outer photoreceptors R1-6 project to the lamina neuropil, and serve as the main input to the motion vision circuitry (Mauss et al. 2017); inner photoreceptors R7 and R8 pass through the lamina without connections and project directly to the deeper medulla neuropil, that also receives lamina projections (Fischbach and Dittrich 1989). In the main part of the retina, R7 and R8 differ in their axonal target layers, with R7 projecting to layer M6, and R8 to layer M3 (Fischbach and Dittrich 1989). R7 and R8 also differ in their rhodopsin expression, being sensitive to short wavelength UV (R7) and blue (R8), respectively, in so-called ‘pale’ ommatidia (Chou et al. 1996; Papatsenko et al. 1997), and to long wavelength UV (R7) and green (R8) in ‘yellow’ ommatidia (Salcedo et al. 1999; Huber et al. 1997). Pale and yellow ommatidia are distributed randomly throughout the main part of the retina (Feiler et al. 1992; Fortini and Rubin 1990), at an uneven ratio that is conserved across insects (Wernet, et al. 2015; Kind et al. 2020). Meanwhile, along the dorsal rim area (DRA) of the eye, the ommatidia are morphologically and molecularly specialized for detecting skylight polarization (Wernet et al. 2003, 2012; Wada

74 1974a), that *Drosophila* can use to set a heading (Mathejczyk and Wernet 2019, 2020; Warren
75 et al. 2018; Weir and Dickinson 2012). In the DRA, the inner photoreceptors express the same
76 UV rhodopsin (Rh3; Fortini and Rubin 1991, 1990) and detect perpendicular angles of
77 polarized UV light (Weir et al. 2016). In contrast to the rest of the medulla, R7-DRA and R8-
78 DRA project to the same medulla layer (M6; Chin et al. 2014; Pollack and Hofbauer 1991;
79 Fischbach and Dittrich 1989), where their targets include polarization-specific cell types
80 (Sancer et al. 2019, 2020; Hardcastle et al. 2021). Across insects, a 'compass pathway'
81 connects the DRA to the central brain via the anterior optic tubercle (AOTU; Homberg 2015;
82 Hardcastle et al. 2021; Pfeiffer and Kinoshita 2012). Anatomical and functional data from
83 *Drosophila* suggests that the central medulla is also connected to the compass pathway
84 (Omoto et al. 2017; Hardcastle et al. 2021; Otsuna et al. 2014), potentially forming parallel
85 pathways for processing different celestial cues (Timaeus et al. 2020; Tai et al. 2021).
86 EM studies have already revealed some of the circuitry downstream of R7 and R8
87 (Takemura et al. 2013, 2015; Gao et al. 2008). For example, axons of R7 and R8 from the
88 same ommatidium are reciprocally connected with inhibitory synapses (Takemura et al. 2013),
89 leading to color-opponent signals in their presynaptic terminals (Schnaitmann et al. 2018).
90 Interestingly, R7-DRA and R8-DRA also inhibit each other (Weir et al. 2016). Other known R7
91 and R8 targets in the main medulla include local interneurons (e.g. Dm8; Gao et al. 2008;
92 Karuppudurai et al. 2014; Pagni et al. 2021; Menon et al. 2019) and projection neurons that
93 provide connections to deeper optic lobe regions (e.g. Tm5 and Tm20 neurons; Karuppudurai
94 et al. 2014; Meinertzhagen et al. 2009; Gao et al. 2008). A previous light microscopy study
95 (Karuppudurai et al. 2014) identified a single cell type, Tm5a, that is specific for yellow medulla
96 columns; this neuron has been used to identify pale and yellow columns in an EM volume
97 (Menon et al. 2019; Takemura et al. 2015; Karuppudurai et al. 2014). Using genetic labelling
98 techniques, four classes of TmY cells have also been reported as specific targets of pale
99 versus yellow photoreceptors (Jagadish et al. 2014), yet previous connectomic studies did not
100 reveal similar cells. The currently most comprehensive EM study of the medulla reconstructed
101 the connections between neurons in 7 neighboring medulla columns (Takemura et al. 2015),

102 revealing a detailed, yet incomplete, inventory of cell types connected to R7-8. This data set,
103 now publicly available (Clements et al. 2020), is remarkable for its dense reconstruction of
104 columnar circuits, but could not be used to identify many multicolumnar neurons, that were
105 cut-off at the edge of the data volume, leaving ~40% of R7-8 synapses onto unidentified cell
106 types. In addition, no EM-based reconstructions of DRA neurons and their connections is
107 currently available.

108 Here we present a comprehensive reconstruction of all inner photoreceptor synaptic
109 outputs and inputs, from pairs of pale and yellow columns and from three DRA columns in the
110 FAFB data set. These reconstructions were carried out within a full brain volume, such that,
111 for the first time, nearly all neurons connected to these photoreceptors were identified. We
112 discovered, through light microscopy, a large visual projection neuron with distinctive
113 morphology, named accessory medulla cell type 12 (aMe12), that selectively innervates pale
114 ommatidia across the medulla. We then reconstructed and then used this cell in the FAFB
115 data set to identify pale and yellow columns, from which we enumerated the connectivity of
116 R7 and R8 with known and novel cell types within the optic lobes and projecting to the central
117 brain, including more cells with pale-yellow specificity, and synapses on axons between
118 neuropils. In the DRA, we show that cellular diversity is reduced, with local interneurons and
119 projection neurons to the AOTU dominating, and connections to the lobula virtually missing.
120 We identify circuit motifs shared between DRA and central columns, and describe modality-
121 specific cell types, including cells with interhemispheric connections and projections to the
122 central brain. Together, we identify the connected neurons that account for 96% of these inner
123 photoreceptor synapses, a comprehensive set of the neurons that comprise the first step of
124 the pathways through which color and polarization signals are transduced to the rest of the
125 brain.

126

127 **Results**

128 <u>Systematic reconstruction of all synaptic targets of inner photoreceptor subtypes</u>

129 We reconstructed R7 and R8 photoreceptor axons in the central region of the right
130 optic lobe, as well as inner photoreceptors from 27 DRA columns from the FAFB data set
131 (Zheng et al. 2018; Figure 1C). From these, we selected seven 'seed columns' (four central,
132 three DRA), for which all pre- and postsynaptic sites of the photoreceptor axons were identified
133 and manually reconstructed, that is annotated and assembled across EM images (Figure 1F;
134 Material and Methods). There were 422 skeletons, corresponding to individual cells, contacted
135 by the seed column photoreceptors, and we focused our analysis on the 245 individual cells
136 with >2 synapses to or from the photoreceptors. We reconstructed the morphology of these
137 cells with a sufficient degree of completeness to ascribe a unique cell type to 92% (225/245)
138 or to identify a cell class (Dm, Mi, Tm, or TmY cell class) for an additional 6.5% (16/245), so
139 that 98% (241/245) of these cells were identified. We also traced and uniquely identified the
140 cell type of all 30 cells that provided >2 synaptic inputs to the photoreceptors. In total, we
141 identified 4043 synaptic connections from the seed column R7 and R8 photoreceptors, and
142 970 synaptic inputs to them, summarized in Figure 1H.
143 To distinguish between pale and yellow columns we took advantage of our discovery
144 of one specific cell type from the accessory medulla that widely arborised in the medulla with
145 ascending branches that align with the photoreceptors (Figure 1Ei-iii). The cell type was
146 selective for R8 input and showed a strong preference for innervating pale columns (Figure
147 1D, Eiii). We identified three of these cells per hemisphere (hereinafter referred to as aMe12),
148 that had heavily overlapping arbors, but only rarely shared ascending branches in the same
149 columns (3/779 columns). Using the presence of aMe12 branches, we were able to assign as
150 pale 38% (297/779) of the medulla columns, in good agreement with studies on the retinal
151 mosaic of *Drosophila* (Feiler et al. 1992; Fortini and Rubin 1990; Bell et al. 2007; Hilbrant et
152 al. 2014). Since further analysis identified a total of 42 DRA columns (see below), we assigned
153 the remaining columns as nominally yellow (Figure 1C). Our reconstructions also revealed
154 another new pale-selective visual projection neuron, that we named ML-VPN1, and confirmed
155 the previously reported yellow-selectivity of Tm5a cells (Menon et al. 2019; Karuppudurai et

156 al. 2014), findings that further supported the designations of pale and yellow seed columns
157 (see below).

158 After mapping the pale and yellow columns, we selected four adjacent central seed
159 columns, two nominally pale and two nominally yellow (Figure 1C). Across the four central
160 seed columns, the absolute number of both synaptic inputs and outputs for R7 and R8
161 photoreceptors were in good agreement with previous reports analyzing a medulla FIB-SEM
162 (focused ion beam scanning electron microscopy) data set (Takemura et al. 2015; Figure 1 –
163 figure supplement 2A-D). As we had access to the complete brain volume, we additionally
164 found substantial numbers of synapses in the axon bundles projecting between the lamina
165 and the medulla, which accounted for 14% and 12% of the output synapses for R7 and R8
166 respectively, and 16% and 27% of their input synapses (Figure 1 F, Figure 1 – figure
167 supplement 2G).

168 We readily identified columns in the DRA region of the medulla since it is only there
169 that both inner photoreceptors terminate in medulla layer M6 (Figure 1F, arrow; Pollack and
170 Hofbauer 1991; Fortini and Rubin 1991; Sancer et al. 2019; Chin et al. 2014; Fischbach and
171 Dittrich 1989). The morphology of DRA-specific Dm-DRA1 cells differs significantly between
172 central and polar positions of the DRA (Sancer et al. 2019), and we therefore chose one polar
173 DRA seed column and two more equatorial columns (Figure 1C). Beyond the 27 DRA columns
174 with manually traced R7-DRA and R8-DRA photoreceptors we mapped the full extent of the
175 DRA region of the medulla by systematically probing for the presence of two inner
176 photoreceptor profiles in layer M6 without reconstruction (see Materials and Methods), which
177 resulted in a total of 42 identified DRA columns (Figure 1C). Direct comparison of the absolute
178 number of pre- versus postsynaptic sites between central and DRA photoreceptors revealed
179 drastic differences: while the numbers of R7 and R7-DRA presynapses were comparable
180 (mean 279, range 262 – 284 for R7-DRA vs mean 297, range 274 - 322 for R7), the number
181 of R8-DRA presynapses was reduced by ~60% compared to those of R8 (mean 166, range
182 157 - 172 for R8-DRA vs mean 380, range 356 - 417 for R8). In particular, there was a striking

183 reduction in the number of synapses from R8-DRA to cells intrinsic to the medulla and to cells
184 that projected to the lobula compared to R8 (see below and Figure 1G, H).
185 We have endeavored to make this comprehensive data set as accessible and
186 navigable as possible. In the following sections we first describe the connections of the central
187 column R7 and R8 cells (Figure 2 – 5), following the sequence of cell classes in Figure 1G-H,
188 before presenting the connections of the DRA (Figures 6 – 9). For brevity, we refer to the
189 region of the medulla innervated by DRA inner photoreceptors as the DRA region, and for
190 clarity we refer to the central column inner photoreceptors as R7 and R8, and the DRA inner
191 photoreceptors as R7-DRA and R8-DRA. The synaptic outputs from and inputs to the central
192 pale and yellow R7-8 cells are summarized in Tables 1-2, for R7-DRA and R-8-DRA in Tables
193 3-4, and presentations of individual cell types include summaries of total photoreceptor
194 synapse counts (e.g., Figure 1Eiii for aMe12). The text highlights downstream cell types that
195 are selective for inputs from either R7 or R8 or are preferentially found in pale or yellow
196 columns. We used 65% as the threshold to consider an input selective and tables of
197 connectivities of the individual cells are arranged by cell type and collected together in
198 Supplementary File 1. The main figures show the morphology of reconstructed exemplars,
199 with the many full reconstructions noted (and listed in Materials and Methods), while the
200 morphologies of individual cells are collected together in Supplementary File 2. The numbers
201 of synapses outside the medulla are summarized in Supplementary File 3. For the cell types
202 for which we are unaware of published, detailed descriptions, we endeavored to produce light
203 microscopic images of single cell clones which were matched largely based on the cell body
204 location, the extent and neuropil-layer-specific branching patterns, and comparisons to any
205 other know cell types (see Materials and Methods). In a few cases, we also use light
206 microscopy to illustrate specific features of known neurons or to explore additional properties
207 (such as direct co-labeling with markers for pale and yellow columns) that are not readily
208 accessible by EM.
209
210 <u>Synapses between R7 and R8, and with lamina cell types</u>

211 The inner photoreceptors inhibit each other via histaminergic synapses, a key
212 mechanism for converting their sensitivity to specific wavelengths into presynaptic color-
213 opponency (Schnaitmann et al. 2018). We annotated a large proportion of the synapses
214 between R7 and R8 along the axons between the lamina and the medulla (Figure 2A, Figure
215 1 – figure supplement 2G). For R8, ~80% of the synaptic input from R7 was found outside the
216 medulla (mean 11.5 synapses per cell, range 9-17), and the R8 inputs to R7 in this region
217 were as frequent (mean 10.3 synapses per cell, range 5-13). These results were not
218 anticipated by prior EM reconstructions of individual neuropils, and our counts are substantial
219 increases in the numbers of inter-photoreceptor synapses (Figure 1 – figure supplement 2D;
220 Takemura et al. 2015; Meinertzhagen and O'Neil 1991).
221 R7-8 pass through the lamina without forming synapses (Meinertzhagen and O'Neil
222 1991), and instead form synapses with lamina cell types in the medulla (Takemura et al. 2008,
223 2013). Our reconstructions revealed that 58% of R7-8 inputs to the lamina cells L1 and L3
224 were also located within the optic chiasm (Figure 1 – figure supplement 1B, Figure 1 – figure
225 supplement 2G, Figure 2 – figure supplement 1A-B).
226
227 R7-8 synapses with distal medulla (Dm) cell types
228 The Dm neurons included the strongest targets of R7-8 (Table 1). Dm9 is glutaminergic
229 and provides excitatory feedback to R7 and R8, regulating their gain and augmenting their
230 color-opponency (Davis et al. 2020; Uhlhorn and Wernet 2020; Gao et al. 2008; Heath et al.
231 2020). It accounted for more than 90% all the synaptic inputs to R7-8 that were not from
232 photoreceptors (333/369 synapses, Table 2). Dm9 cells span multiple columns and tile the
233 medulla (Nern et al. 2015; Takemura et al. 2015; Figure 2B). We reconstructed six Dm9 cells
234 that were contacted by our seed column R7-8s, which received 16% of all R7-8 synapses,
235 and provided 57% of the total seed column photoreceptor synaptic input (Tables 1, 2). Of the
236 six Dm9 cells, one cell occupied our seed columns and formed the bulk of the synapses
237 between R7-8 and Dm9 in these columns. The other five cells received far fewer connections
238 and only in medulla layers M1 and M6. The well-connected Dm9 cell that we fully

239 reconstructed received 92 synapses per seed column (mean, range 78-102), and provided 70
240 synapses per seed column (mean, range 64-78) offering the most detailed picture of Dm9
241 connectivity yet (Supplementary File 1—Dm9 outgoing). While its R7-8 inputs were biased
242 towards R8 (31% R7 vs 69% R8), the output synapses were balanced (55% R7 vs 45% R8),
243 and pale and yellow columns were equally contacted (outputs from R7 and R8: 54% pale vs
244 46% yellow; inputs from R7 and R8: 53% pale vs 47% yellow). In total, 8% of the synapses
245 from R7-8 to Dm9 were outside the medulla (34/445 of all R7-8 synapses onto Dm9), on
246 processes following the photoreceptor axons (Figure 2Bii, arrow).

247 The most strongly connected R7 target cell type was Dm8, a central component of
248 *Drosophila*'s circuitry mediating color vision and wavelength-specific phototaxis (Gao et al.
249 2008; Melnattur et al. 2014; Pagni et al. 2021). Individual Dm8 cells cover multiple columns in
250 medulla layer M6 (Gao et al. 2008; Nern et al. 2015; Luo et al. 2020), and extend processes
251 vertically, with one characteristic process usually reaching higher than the others, up to layer
252 M3, defining a so-called 'home' column (Figure 2Ci, arrow). In our reconstructions, we
253 analyzed the connectivity of each Dm8 cell with the surrounding pale and yellow R7
254 photoreceptors in relation to its home column.

255 Dm8 cells were exclusively R7 targets, with no synapses from our seed column R8s.
256 Individual R7 cells synapsed onto 8 Dm8 cells (mean, range 6-10), contacting 15 Dm8s
257 altogether, and there were five Dm8 cells with processes spanning our seed column R7s and
258 receiving >40 synapses from them. Two of these cells had a pale home column and no input
259 from yellow seed column R7s, and two had a yellow home column and received 13% and 20%
260 of their seed column input from pale R7s (Supplementary File 1—Dm8 outgoing). The fifth cell
261 had a pale home column outside the seed column area, and its seed column inputs were
262 divided evenly, 55% from pale and 45% from yellow. Collectively, these data revealed that
263 Dm8 cells selectively innervated columns around the home column, but not simply the closest
264 columns.

265 In view of the importance of Dm8 cells for processing R7 output, we extended our
266 reconstructions to include all the photoreceptor inputs to three Dm8s, one with a pale home

267 seed column, one with a yellow home seed column, and one with a yellow home column
268 outside the seed columns (Figure 2Cii). All three cells were most densely innervated by R7 in
269 their home column: the yellow home column cells received 26% and 23% of their R7 input in
270 the home column, and the pale home column cell received 52% (Figure 2Ciii). The innervated
271 columns outside the home column were not the nearest neighbors of the home column, but
272 formed a more irregular, idiosyncratic spatial pattern. Together, our data are consistent with
273 Dm8 cells having a central, strong R7 input from either a pale or a yellow cell in its home
274 column and a surround that integrates spatially varied pale and yellow R7 inputs.

275 Two additional Dm cell types, Dm11 and Dm2, were prominent inner photoreceptor
276 targets. Dm11 cells tile the medulla in layer M6, with each cell covering ~9 columns (Nern et
277 al. 2015; Figure 2Di), and sending vertical processes that reach far up into the optic chiasm,
278 tracking the R7 and R8 photoreceptor axons (Courgeon and Desplan 2019; Figure 2Dii, Diii,
279 arrows). Dm11 was R7-selective, with 87% of its seed column photoreceptor inputs originating
280 from R7s (Figure 2Dii). Two-thirds of the Dm11 seed column R7-8 inputs were located outside
281 of the medulla (44/63 synapses), and this was another cell type innervated by photoreceptors
282 much more than previously reported (Figure 1 – figure supplement 2D; Clements et al. 2020;
283 Takemura et al. 2015). One Dm11 cell squarely occupied the four seed columns, receiving 52
284 synapses from the seed column photoreceptors, and this cell showed no clear bias for pale or
285 yellow inputs (40% pale, 60% yellow; Supplementary File 1—Dm11 outgoing).

286 Dm2 is a columnar cell type that spans 1-2 columns and has processes that reach
287 from layer M6 up to layer M3 to receive synaptic input from R8 cells (Figure 2Ei, Eii; Takemura
288 et al. 2013; Nern et al. 2015). We reconstructed four Dm2s that received 77% of their seed
289 column photoreceptor input from R8 (Figure 2Eii) and 81% from pale cells. Three of the Dm2
290 cells were centered on seed columns, with two in the pale seed columns receiving 36 and 35
291 synapses, and the cell in a yellow seed column receiving 18; the fourth cell was centered on
292 a neighboring yellow column and innervated one of the pale seed columns (Supplementary
293 File 2—Dm2). In the columns of the medulla FIB-SEM data set that have been identified as
294 pale and yellow (Menon et al. 2019; see Materials and Methods), Dm2 was also R8-selective

295 (70% of photoreceptor input from R8; Takemura et al. 2015; Clements et al. 2020). The cell
296 was missing from one of the pale columns in that data set (Takemura et al. 2015), but in the
297 columns where it was present, the cells received ~50% more synapses per column in the pale
298 columns (18 mean, range 16-20 in pale columns, versus 12, mean, range 10-15 in yellow
299 columns).
300
301 R7-8 synapses with medulla intrinsic (Mi) and medulla tangential intrinsic (Mti) cell types
302 The Mi cells connect the distal with the proximal medulla (Fischbach and Dittrich 1989).
303 These two medulla zones are separated by the serpentine layer M7, containing the processes
304 of large medulla tangential cells, including those intrinsic to the medulla which we refer to as
305 Mti cells. There were three Mti cells contacted by our seed column R7-8, and we matched
306 these cells to light microscopy images of two separate, previously undescribed cell types using
307 the locations of cell bodies, sizes of arbors and layer expression (Figure 3A,B). Both cell types
308 received a modest number of synapses from our seed-column R7-8 (Mti1: 7 synapses; Mti2:
309 10 and 2 synapses, respectively; Supplementary File 1—Mti outgoing), yet were likely to be
310 substantial targets overall since their processes covered large sections of the medulla (Figure
311 3A, B). The first cell type, which we refer to as Mti1, had a cell body located in the cell body
312 layer distally to the medulla, similar to most medulla neurons. Its processes were
313 asymmetrically oriented mainly along the dorsoventral axis, with dendrites that occupied
314 layers M3-M6, and axonal processes oriented dorsoventrally that spread laterally in layers
315 M7-M8 (Figure 3A). The second cell type, here named Mti2 (Figure 3B), had cell bodies
316 located at the anterior ventral edge of the medulla, adjacent to where its processes entered
317 and coursed through layer M7 going on to make elaborations in layer 6 and small, further
318 vertical processes that reach vertically up to layers M3 and M4 (Figure 3Biii and 3Bvi, arrows).
319 In our EM reconstructions, two cells shared these properties and overlapped around our seed
320 columns (Figure 3Bv).
321 Mi15 is the only local dopaminergic medulla cell type identified in *Drosophila* so far
322 (Meissner et al. 2019; Davis et al. 2020). Its morphology and connectivity in the medulla have

323 been described in previously (Takemura et al. 2013, 2015), and it has a long process that
324 extends into the optic chiasm and tracks photoreceptor axons. Our reconstructions revealed
325 that this process was a locus of photoreceptor input (Figure 3Cii, black arrow), and that Mi15
326 cells were R8-selective, with 91% of their seed column photoreceptor input drawn from R8.
327 The Mi15 cells received 47% of their seed column photoreceptor input outside the medulla
328 (mean of 15/32 synapses per column; Figure 1 – figure supplement 2G), and R8s
329 characteristically formed synapses with Mi15 cells at locations where they also made
330 synapses with R7 (Figure 3 – figure supplement 1A).

331 The columnar cell types Mi1, Mi4 and Mi9 are integral components of the ON-motion
332 pathway (Strother et al. 2017); prior EM reconstructions have found they receive significant
333 input from R7-8, a result confirmed by our data (Takemura et al. 2013, 2015; Figure 3 – figure
334 supplement 1B-D). In the identified pale and yellow columns of the medulla FIB-SEM data set,
335 Mi9 was selective for R8 (65% R8 vs 35% R7 input), and 53% of its photoreceptor input
336 originated from pale R8 (Takemura et al. 2015). Our data reinforced the observation that Mi9
337 show a bias for R8 input: 68% of our reconstructed Mi9 input originated from pale seed column
338 R8; the cells in pale columns received 15 and 14 R7-8 synapses, while those in yellow
339 columns received 6 and 4 (Figure 3 – figure supplement 1D).

340

341 <u>R7-8 synapses with cell types projecting to the lobula</u>

342 The lobula receives diverse inputs from the medulla, including from cell types required
343 for wavelength-specific phototaxis and learned color discrimination (Gao et al. 2008;
344 Karuppudurai et al. 2014; Melnattur et al. 2014; Otsuna et al. 2014). Many of these cell types
345 express the histamine receptor *ort*, notably the transmedulla (Tm) cell types Tm5a, Tm5b,
346 Tm5c and Tm20 (Gao et al. 2008), indicating they receive direct input from the histaminergic
347 R7 or R8 (Pantazis et al. 2008). We found all of these Tm cell types and they were highly
348 connected with the seed column R7-8, with a mean of 35 seed column photoreceptor inputs
349 per cell for Tm20, 27 for Tm5a, 23 for Tm5c, and 24 for Tm5b (Figure 4, Figure 4 – figure
350 supplement 1).

351 The cholinergic Tm5a cell type was the first cell type described to show pale versus
352 yellow selectivity, being preferentially innervated by yellow R7, as revealed by genetic
353 methods and light microscopy (Karuppudurai et al. 2014). It was identified in the medulla FIB-
354 SEM data set (Menon et al. 2019) and used for identifying putative yellow columns therein
355 (see Materials and Methods). Its medulla processes are centered on one yellow column, with
356 a single main dendrite from which branches spread laterally reaching some of the neighboring
357 columns in M3, M6 and M8, and an axon terminating in lobula layer 5B manifesting a
358 characteristically hooked final reversal of direction (Gao et al. 2008; Figure 4A). In both our
359 yellow seed columns there was a Tm5a cell, whose seed column photoreceptor input was
360 exclusively from the R7 in the home column (Figure 4Aiv). Reassuringly, there were also no
361 Tm5a cells centered on pale columns or innervated by pale photoreceptors. Thus, the Tm5a
362 cells supported the designation of our seed columns as pale or yellow, that was based on the
363 presence or absence of aMe12 vertical processes. One more cell that we refer to as a Tm5a-
364 like had the morphological features of a Tm5a cell, and was selective for yellow seed column
365 input, but from R8 (Figure 4 – figure supplement 1A). There was no cell with a similar
366 morphology or connectivity in the medulla FIB-SEM data set, as explored using NeuPrint
367 (Clements et al. 2020). The cell received its R8 input on three different dendritic branches,
368 indicating that they were unlikely to have resulted from a reconstruction error (Figure 4 – figure
369 supplement 1Aiv). Overall, our results confirmed the selectivity of Tm5a cells for yellow
370 columns and the reliability of finding R7-selective Tm5a cells in yellow columns.
371 The cholinergic Tm5b cell type is similar to Tm5a, but with ~2-3 vertical main dendrites
372 spanning ~5 columns, from which branches spread laterally in M3, M6 and M8 (Gao et al.
373 2008; Karuppudurai et al. 2014; Meinertzhagen et al. 2009; Figure 4B). A recent analysis of
374 the medulla FIB-SEM data set has proposed that Tm5b cells are pale-specific (Menon et al.
375 2019). Our reconstructions revealed two Tm5b cells that were innervated by pale R7, and not
376 yellow R7 (Figure 4B), with only a minor input from seed column R8 (19 and 20 R7 inputs, vs
377 7 and 2 R8 inputs, respectively). We also identified 3 more cells with a morphology matching
378 the Tm5b cell type, but innervated by predominantly yellow inputs, which we refer to as Tm5b-

379 like (Figure 4 – figure supplement 1B). In these yellow-specific cells, R8 input dominated, with
380 9.0 R8 synapses (mean, range 4-16), versus 4.7 R7 synapses (mean, range 3-7; Figure 4 –
381 figure supplement 1Biv). In particular, one Tm5b-like cell had >20 synapses, and innervated
382 all four seed columns, and so was well covered in our reconstructions (Figure 4 – figure
383 supplement 1B).

384 The Tm5c cells are glutaminergic neurons, spanning ~8 columns with single vertical
385 dendrite in the medulla, from which lateral branches spread out in M1, as well as M3 and M6,
386 while the axons terminate near the boundary between lobula layers 5 and 6, often with a
387 branch in layer 4 (Gao et al. 2008; Karuppudurai et al. 2014; Meinertzhagen et al. 2009; Figure
388 4C); one cell axon terminated deep in layer 6 (Supplementary File 2—Tm5c). Our
389 reconstructions confirmed they were selective for R8, as indicated previously (Takemura et al.
390 2013, 2015; Karuppudurai et al. 2014; Figure 1 – figure supplement 2D). Six Tm5c cells were
391 innervated by seed column photoreceptors, and they all received many synapses from
392 multiple columns, ranging from 11 to 44, consistent with R7-8 input over a large spatial
393 receptive field. One Tm5c was centered on our seed columns, with processes in all of them
394 (Figure 4Cii), and only targeted by yellow seed column photoreceptors, predominantly R8.
395 This bias towards yellow R8 inputs was maintained over the population (Figure 4Civ), yet there
396 were two Tm5c cells with pale selectivity, and it remains possible that different Tm5c subtypes
397 exist (Supplementary File 1–outgoing Tm5c). In the identified pale and yellow columns of the
398 FIB-SEM data set, there were two Tm5c cells reliably contacted by R7-8, with > 10 synapses
399 (Takemura et al. 2015; Clements et al. 2020). These two cells also showed a bias for yellow
400 R8 input, with respectively 18 and 11 synapses from yellow R8 cells, versus 5 and 0 synapses
401 from pale R8 and R7 combined.

402 The Tm20 cell type is a known columnar target of R8 (Takemura et al. 2013, 2015;
403 Gao et al. 2008), and the four Tm20 cells located in our seed columns were indeed selectively
404 connected to R8 (Figure 4 – figure supplement 1C, Figure 1 – figure supplement 2D). The
405 Tm20 and Tm5c cell types together received 140 synapses from seed column photoreceptors,
406 making them two of the most targeted cell types (Table 1). We also found one TmY10 cell that

407 received 7 synapses from our seed column photoreceptors (Supplementary File 1 - TmY10).
408 In addition, we partially reconstructed 10 other Tm cells with a mean of 4.4 photoreceptor
409 synapses per cell. We did not fully reconstruct these lightly innervated Tm cells; Tm subtypes
410 may manifest subtle differences in morphology and connectivity that require multiple examples
411 to distinguish (Jagadish et al. 2014; Gao et al. 2008; Fischbach and Dittrich 1989), which was
412 beyond the scope of our targeted reconstruction.

413 We found one more prominent cell type projecting to the lobula, which we refer to as
414 the medulla-to-lobula cell type ML1 (Figure 4D). We completely reconstructed one cell and
415 used light microscopy data to explore the anatomy of the population (Figure 4Dv-vi). These
416 cells projected to the deepest layer of the lobula and also to the adjacent central brain, with
417 cell bodies in the anterior medulla cell body rind (Figure 4Dv). They were morphologically
418 similar to a putative *ort*-expressing cell identified by Gao et al. (2008; see their Figure S6).
419 ML1 dendrites covered ~20 medulla columns with overlap, and the population covered the
420 medulla (Figure 4Dii,vi), ramifying from vertical processes in layers M1-4, and also in M8
421 (Figure 4Diii,v). Unlike the Tm cells, the ML1 axons exited the distal surface of the medulla
422 and traveled anteriorly to enter and terminate in or near lobula layer 6 (Figure 4Diii, v, vi),
423 providing an alternate pathway connecting the medulla to the lobula. Light microscopy
424 suggests that a fraction of the cells also formed synapses in the central brain, in the posterior
425 lateral protocerebrum (Figure 4Dvi, arrow). The input to the lobula was non-columnar, and
426 although it was not strictly retinotopically organized, it was spatially organized, with two axon
427 bundles originating in the dorsal and ventral medulla terminated in two general locations,
428 incompletely covering the lobula (Figure 4 – figure supplement 2). Our seed columns
429 contacted four ML1 cells, making an average of 25 synapses per ML1 cell. The cell was
430 exclusively targeted by R8s from both pale and yellow columns (Figure 4Div).

431

432 <u>Visual projection neurons connecting R7-8 with the central brain</u>

433 Nearly 10% of the synapses made by the central seed column R7-8 were with cells
434 projecting directly to the central brain (Table 1). Of these, the strongest targets were the MeTu

435 cells, which resemble Tm cells, but instead of sending axons to the lobula, projected to the
436 AOTU via the anterior optic tract (Fischbach and Lyly-Hunerberg 1983; Otsuna et al. 2014;
437 Otsuna and Ito 2006; Omoto et al. 2017; Timaeus et al. 2020; Tai et al. 2021; Figure 5A). Our
438 reconstructions confirmed that MeTu cells were targets of R7 (Timaeus et al. 2020), and that
439 their photoreceptor input was exclusively from R7 (Figure 5Aiv). In total MeTu cells received
440 15% of all the seed column R7 synapses (Table 1). We found 7 such neurons and
441 reconstructed the complete morphology of one. Their dendrites overlapped and covered ~20-
442 30 columns (Figure 5Aii), while the axons all targeted the lateral tip of the AOTU (Timaeus et
443 al. 2020; Omoto et al. 2017; Tai et al. 2021; Figure 5Ai).

444 The presence of MeTu cells was the largest discrepancy by synapse count between
445 our list of R7 targets and those of the medulla FIB-SEM data set (Clements et al. 2020;
446 Takemura et al. 2015; Figure 1 – figure supplement 2E), which was focused on columnar cell
447 types and did not identify MeTu cells. In the FIB-SEM data set, we identified a partially
448 reconstructed Tm cell (Figure 1 – figure supplement 2F) and several cells annotated as Dm7
449 as potential matches to MeTu cells. We did not identify any Dm7 cells postsynaptic to R7 in
450 our data. We confirmed details of the connectivity of our MeTu neurons that were found for
451 the FIB-SEM putative Dm7 neurons (including strong inputs from Dm2 and Mi15 neurons),
452 and we propose that the partially reconstructed Tm cells and also Dm7 cells in the 7-column
453 data set were most likely MeTu cells, resolving the largest (numerical) discrepancy between
454 the data sets, and underscoring the benefit of reconstructing small circuits in whole-brain EM
455 volumes.

456 Amongst the photoreceptor target cells projecting to the central brain, we identified a
457 second cell type whose axonal projections follow the anterior axonal tracts of the ML1 neuron,
458 that we refer to here as ML-VPN1 (Figure 5B). The cell bodies were located near the anterior
459 proximal medulla, and, based on our match using light-microscopic data, their dendrites
460 overlapped, with each cell spanning tens of columns, collectively covering the medulla (Figure
461 5Ci-vi). The dendrites ramified along the border of M7 and M8, with vertical processes
462 reaching up and spreading laterally in M3 and again vertically up to M1 (Figure 5Bii-iii, Ciii).

463 Although the ML-VPN1 axons followed the ML1 axonal tract, they innervated the posterior
464 lateral protocerebrum (PLP) of the ipsilateral hemisphere, in a region just posterior to the optic
465 glomeruli (Figure 5Bi, Ci). The ML-VPN1 cells were almost exclusively targeted by the pale
466 R8, with 8.7 seed pale R8 inputs per cell (mean, range 5-14), and just one yellow R8 input
467 across the three cells connected to our seed column photoreceptors (Figure 5Biv). Light
468 microscopy of co-labelled ML-VPN1 neurons and either yellow R8 axons (labelled for Rh6 in
469 Figure 5Cvi) or pale R8 axons (labelled for Rh5 in Figure 5 – figure supplement 1) supported
470 the pale preference seen in the EM data: ~90% of columns in which ML1 arbors and
471 photoreceptors appeared to overlap were pale. Together, our data indicate that ML-VPN1
472 neurons have a strong bias for pale R8 input.

473 The aMe12 cells were also R8 targets, and the two contacted cells received 15 and 11
474 R8 synapses, and 2 and 2 R7 synapses, respectively in the seed columns (Figure 1D, Eiii,
475 Supplementary File 1—aMe12 outgoing). Their axons also targeted the PLP, although in
476 different locations to ML-VPN1, but they did so in both hemispheres (Figure 5D). In addition,
477 aMe12 cells also projected to the mushroom body calyces of both hemispheres, as well as to
478 the contralateral and ipsilateral accessory medulla and superior clamp (Figure 5Di, Dii). All
479 three aMe12 cells shared a characteristic branching pattern, but only one of them additionally
480 innervated the contralateral accessory medulla (Figure 5Dii). The aMe12 cell type is present
481 in the hemibrain connectome, where it is also a strong input to γd Kenyon cells (Li et al. 2020;
482 Scheffer et al. 2020).

483 There were 5 additional tangential cells projecting to the central brain (Mt-VPNs)
484 targeted by seed column R7-8, collectively receiving 25 synapses (1 neuron in Figure 5E,
485 others in Figure 5 – figure supplement 2). The most targeted cell, which we refer to as Mt-
486 VPN1, had processes in layer M7, with branches reaching up into layers M5-M6, where it
487 received inputs from both seed column yellow R7s, and projected an axon to the posterior
488 lateral protocerebrum (Figure 5E). Despite the exclusive seed connections with yellow R7, Mt-
489 VPN1 was not specific for yellow R7: we traced Mt-VPN1 in 20 columns, in which it received
490 input from 13 yellow R7, and 7 pale R7 cells. The remaining tangential cells included a match

491 to an octopaminergic neuron (OA-AL2i3; Busch et al. 2009; Figure 5 – figure supplement 2A).
492 This cell had processes in the distal medulla in layers M1-M2 as well as processes reaching
493 out into the chiasm which received photoreceptor input (Figure 5 – figure supplement 2Aii-iii),
494 and an axon that ipsilaterally innervated the inferior and superior posterior slope, and the
495 flange (Figure 5 – figure supplement 2Ai). This cell was one of the rare cell types that formed
496 synapses onto photoreceptors, making 5 synapses onto the R7-R8, but only in one yellow
497 column (Supplementary File 1—Mt-VPN). The remaining Mt-VPN cells were very lightly
498 innervated by the seed column photoreceptors in multiple (Figure 5 – figure supplement 2Cii)
499 and single columns (Figure 5 – figure supplement 2 Bii, Dii), but may integrate large numbers
500 of photoreceptor inputs as they covered many columns. Collectively they innervated the
501 ipsilateral superior posterior slope, accessory medulla, and lobula, and in both hemispheres
502 the inferior posterior slope and lobula plate (Figure 5 – figure supplement 2B-D), revealing
503 multiple pathways for transmitting direct photoreceptor signals into the central brain.
504
505 Synapses between R7-DRA and R8-DRA, and with medulla cell types
506 The following four sections present the first EM connectomic data for targets of the
507 polarization-sensitive photoreceptors in the DRA of *Drosophila*. We first describe the cell types
508 targeted by photoreceptors in the DRA region that were also found in the central columns
509 (Figure 6), followed by modality-specific Dm cell types connected exclusively to DRA inner
510 photoreceptors (Figure 7), visual projection neurons connecting the DRA region and central
511 brain (Figure 8), and finally cell types only found in the DRA region (Figure 9).
512 The anatomical arrangement of synapses between R7-DRA and R8-DRA strikingly
513 resembled that of central R7 and R8. The number of R7-DRA synapses onto R8-DRA was
514 similar (13.7 mean, range 10 – 16), accounting for 4.9% (41/837) of the total R7-DRA output
515 (Figure 6 – Figure supplement 1A, Table 3), and the number of R8-DRA synapses onto R7-
516 DRA was also similar (36.0 mean, range 33-38; Figure 6 – Figure supplement 1B, Table 3).
517 Many of the synapses between the inner photoreceptors were also located outside the
518 medulla (15% of R8-DRA synapses to R7-DRA, 16/108, mean 5.3 synapses per cell, range

519 3-8; and 48% of R7-DRA synapses to R8-DRA, 19/41, mean 6.3 synapses per cell, range 4-
520 8; Figure 6Ai, arrow, Supplementary File 3).

521 The Dm9 cells in the DRA region were prominent synaptic targets of both inner
522 photoreceptors, and provided strong synaptic feedback onto them (Figure 6B, Table 3, 4).
523 They received 31.7 R7-DRA synapses per column (mean, range 26 – 38), corresponding to
524 11.3% (95/837) of the total R7-DRA output (Table 3), and R8-DRA was more strongly
525 connected with 38.3 synapses (mean, range 36 – 43), corresponding to 23% (115/499) of the
526 total R8-DRA output. Although the total number of inner photoreceptor inputs to Dm9 per seed
527 column were fewer in the DRA region compared to central seed columns (70 mean, range 62
528 – 81), their relative strength was similar to central columns (Supplementary File 1). The
529 distribution of R8 and R8-DRA synapses onto Dm9 was also different, with the greatest density
530 of R8-DRA synapses in layer M6, reflecting the characteristic morphology of R8-DRA (Figure
531 6Bi). Our prior light microscopic study suggested that marginal Dm9 cells might receive both
532 DRA and non-DRA inputs (Sancer et al. 2020). We therefore reconstructed R7 and R8 in three
533 non-DRA columns innervating the same DRA Dm9, and found that cell indeed received input
534 from both color and polarized light-sensitive photoreceptors (Figure 6Biv).

535 Dm2 was an R8 target in the central columns, but in the DRA region there were
536 drastically fewer R8-DRA inputs, with equal contacts from R7-DRA and R8-DRA (7.0 mean,
537 range 5 – 10 for R7-DRA, 9.0 mean, range 5 -15 for R8-DRA synapses per column; Figure
538 6Ci-ii, Table 3; (Sancer et al. 2020). The Dm11 cell type was an R7 target in central columns,
539 but in the DRA region it received minor, balanced input from both R7-DRA and R8-DRA and
540 was only found in one of the three DRA seed columns (4 from R7-DRA and 8 from R8-DRA;
541 Figure 6 – figure supplement 2D, Table 3). Thus, while a reduction in R8-DRA input to cells
542 targeted by R8 in the central columns was a repeated feature of the DRA region, as
543 exemplified by Dm2, it was also seen in cells targeted by R7, such as Dm11.

544 The connectivity of inner photoreceptors with lamina cells was maintained in the DRA
545 region, including with a substantial fraction of synapses outside the medulla (Figure 6 – figure
546 supplement 2A,B; Figure 1 – figure supplement 2G; Supplementary File 3), but there were

547 markedly fewer synapses to Mi cells from R8-DRA than from R8, including to Mi1 and Mi9,
548 while Mi4 was not contacted in the seed DRA columns at all (Mi1: 3 mean, range 2 – 5; Mi9:
549 4 mean, range 0 – 9; Figure 6 – figure supplement 2C,E). Of all the Mi cell types, Mi15 alone
550 was a significant photoreceptor target in the DRA region, receiving synapses from both R7-
551 DRA and R8-DRA (respectively, 7 mean, range 4 – 9, and 6 mean, range 3 – 10; Figure 6Di-
552 ii, Table 3). Compared to the central column R7-8 input, Mi15 cells gained R7-DRA synapses
553 in the DRA region, and they maintained their high fraction of inputs outside the medulla (Figure
554 6D; Figure 1 – figure supplement 2G; Supplementary File 3).
555 Only one Tm cell type, Tm20, was connected to inner photoreceptors with more than
556 2 synapses throughout all three DRA seed columns. This cell type was selective for R8-DRA,
557 but was much more weakly connected (5.3 mean, range 4 – 8 for R8-DRA; Table 3,
558 Supplementary File 1) than it was to R8 in the central columns. There was only one other
559 strongly connected Tm cell, which we refer to as Tm5-like, that had 12 synaptic inputs from
560 both R7-DRA and R8-DRA inputs in one of the three DRA columns (Figure 6 – figure
561 supplement 2F). Together, these four cells highlight the absence of projections to the lobula,
562 as compared to the central columns with 27 identified Tm cells (Table 1).
563
564 <u>Dm8-like photoreceptor targets in the DRA region</u>
565 The strongest target of R7-DRA cells was Dm-DRA1 (Sancer et al. 2019). Together,
566 20 Dm-DRA1 cells received 70.1 (mean, range 66 – 77) synapses per DRA seed column,
567 corresponding to 25.3% (212/837) of total R7-DRA output (Table 3, Supplementary File 1).
568 There were no synaptic inputs from R8-DRA, and synapses from R7-DRA to Dm-DRA1 were
569 consistently restricted to the proximal edge of layer M6 where R8-DRA are not present (Figure
570 7Ai, Aii). There were few synapses in neighboring non-DRA columns (Figure 7 – figure
571 supplement 1A), and only one of the contacting R7 cells made a substantial number (11) of
572 synapses. The inner photoreceptors choose their DRA fates independently, and therefore this
573 photoreceptor could be an R7-DRA, even though the R8 in the same column terminated in
574 M3; low numbers of such mixed ommatidia consistently occur at the DRA boundary (Wernet

575 et al. 2003; Wada 1974b). Dm-DRA1 cells have deep projections that leave the DRA region
576 and stratify below layer M6, and these did not receive strong photoreceptor input (Figure 7Aii,
577 compare light microscopy of clone in 7Aiii), nor did they preferentially occupy either pale or
578 yellow columns (Figure 7 – figure supplement 2).

579 To gain a better understanding of the synaptic connectivity between R7-DRA and Dm-
580 DRA1, we identified all the DRA photoreceptor inputs to three fully reconstructed Dm-DRA1
581 cells (Figure 7B). Each cell was connected to 9 (mean, range 8 – 10) neighboring R7-DRA,
582 receiving a total of 94 synapses (mean, range 66 – 112) from R7-DRA, but almost no
583 connections from R8-DRA (2 R8-DRA form 3 and 2 synapses with the posterior Dm-DRA1;
584 Figure 7Bi). Dm-DRA1 cells have been proposed to be DRA-specific equivalents of Dm8
585 (Courgeon and Desplan 2019; Sancer and Wernet 2021), but we never detected vertical
586 protrusions resembling Dm8 'home columns'. The smoothed distribution of synapses along a
587 linear projection of the DRA covered ~50 μm with the strongest input in the center, but without
588 a single, dominant home column (Figure 7Biv, Figure 7 – figure supplement 3).

589 The Dm-DRA2 cell type was the strongest R8-DRA target after Dm9 and R7-DRA
590 (Table 3), with 34.3 (mean, range 19 – 44) seed columns synapses to nine cells (Figure 7C,
591 Supplementary File 1; Sancer et al. 2019). Each Dm-DRA2 cell had multiple characteristic
592 vertical projections, whose lengths were variable but markedly longer than the single vertical
593 processes of Dm8 home columns, often reaching layer M1 (Figure 7Ci, Ciii; Sancer et al.
594 2019), and these vertical projections received R8-DRA synapses (Figure 7Cii, Ciii, Eiii). To
595 quantify the pattern of their photoreceptor inputs, we fully reconstructed three Dm-DRA2 cells.
596 These cells were innervated by 9.3 (mean, range 8 – 11) R8-DRA and received minor inputs
597 from R7-DRA (3.7 mean, range 3 – 4 cells per Dm-DRA2 with an average of 5.3, range 3 – 7
598 synapses; Figure 7D, Supplementary File 1). The distribution of R8-DRA synapses to each
599 Dm-DRA2 cell covered ~50 μm with a peak in its center and without a single, obvious home
600 column (Figure 7Di, Dii). Thus, Dm-DRA2 directly integrate photoreceptor inputs over multiple

601 columns, with stronger input at the center of their receptive field, much like we found for Dm-
602 DRA1.

603 The reconstructed Dm-DRA1 cells highly overlapped along the DRA region, as did the
604 Dm-DRA2 cells (Figure 7Ei, Eii; Sancer et al. 2019). The population of all Dm-DRA1 cells
605 connected to the same R7-DRA seed photoreceptor (8.3 mean, range 6 - 11) spanned 17
606 DRA columns (mean, range 13 - 19), corresponding to just under half the length of the DRA
607 region. In comparison, the number of Dm-DRA2 targets of one R8-DRA was fewer (3.3 mean,
608 range 2 – 5 Dm-DRA2 cells per column), and the length of the DRA region covered was also
609 shorter at 10.7 columns (mean, range 10 -12). These differences in connectivity may have
610 implications for how the two Dm-DRA cell types differently compute skylight polarization
611 information originating from the same visual field. Finally, comparison of inputs to Dm-DRA1
612 and Dm-DRA2 from the same location along the DRA revealed a separation of R7-DRA and
613 R8-DRA synapses into different sublayers of M6 (Figure 7Eiii), confirming prior observations
614 from light microscopy (Sancer et al. 2019).

615

616 Visual projection neurons connecting R7-DRA with the central brain

617 The second most prominent R7-DRA target was a cell type that we refer to as MeTu-
618 DRA (Figure 8A). These cells exclusively received R7-DRA synapses, with no input from R8-
619 DRA, and are modality-specific. Both the reconstructed cells and the matching light
620 microscopy MeTu-DRA clones projected long axons to the small unit of the AOTU (Figure
621 8Aii), identifying them as specialized MeTu cells (Omoto et al. 2017; Panser et al. 2016;
622 Otsuna et al. 2014; Tai et al. 2021). They closely resemble cells described in the DRA region
623 of optic lobes from larger insects (Pfeiffer and Kinoshita 2012; el Jundi et al. 2011). All 30
624 reconstructed MeTu-DRA cells received 61.3 (mean, range 49 – 85) R7-DRA synapses per
625 seed column, corresponding to 22.0% (184/837) of the total R7-DRA output (Figure 8Aiii,
626 Table 3, Supplementary File 1). Synapses from R7-DRA to MeTu-DRA were restricted to the
627 photoreceptor tips at the proximal edge of layer M6, as we found for Dm-DRA1 (Figure 8Aiv).
628 MeTu-DRA cells also innervated the dorsal medulla outside the DRA region (Figure 8Av), but

629 avoided non-DRA photoreceptors by stratifying below M6, and showed no obvious pale or
630 yellow preference (Figure 8 – figure supplement 1A). We visualized single MeTu-DRA cell
631 clones in the DRA and found their photoreceptor contacts were always restricted to the DRA
632 region (Figure 8Av, arrow). The medulla branches of all MeTu-DRA skeletons connected to
633 R7-DRA from the same DRA seed column (11.3 mean, range 8 – 16) widely overlapped,
634 covering 15 DRA columns (mean, range 12 – 17; Figure 8Avi). Thus, the MeTu-DRA cells
635 receive skylight polarization information from R7-DRA over similar portions of the sky as Dm-
636 DRA1 cells.

637 Since the axons of the central region MeTu cells projected to a discrete subdomain of
638 the small unit of the AOTU (Figure 5Ai), we assessed whether they intermixed with MeTu-
639 DRA terminals, and found they do not. The MeTu-DRA and the MeTu cells we reconstructed
640 from central columns terminate in separate, adjacent AOTU compartments (Figure 8vii, inset).

641 We identified one additional, previously uncharacterized visual projection neuron type
642 connecting the DRA region with the central brain, which we refer to as VPN-DRA. These cells
643 send axonal projections to the PLP (Figure 8Bi, Bii). There were 6 VPN-DRA cells with >2
644 synapses contacted by the DRA seed columns, and they received 10 (mean, range 6 – 13)
645 R7-DRA synapses per seed column (corresponding to 3.6%, 30/837, of total R7-DRA output),
646 with no R8-DRA synapses (Figure 8Biii, Table 3, Supplementary File 1). The main branches
647 in the medulla of VPN-DRA cells followed the DRA region, with smaller branches innervating
648 non-DRA columns (Figure 8Biv). Double labeling of photoreceptors and a driver line with
649 apparent VPN-DRA expression indicated that photoreceptor input to VPN-DRA cells might be
650 dominated by DRA inner photoreceptors, with only fine processes contacting non-DRA
651 photoreceptors (Figure 8Bv).

652 VPN-DRA cells form an overlapping group of neurons covering the entire DRA region
653 of a given hemisphere (Figure 8Bvi). There was morphological heterogeneity within the
654 population, with some cells having additional processes, both in the medulla, as well as in the
655 central brain and a different cell body position (Figure 8 – figure supplement 1B). Therefore,
656 there exist different subtypes of VPN-DRA.

657

658 Other newly identified photoreceptor targets in the DRA region

659 Two more previously uncharacterized cell types received photoreceptor input in the
660 DRA seed columns. The first, which we refer to as MeMe-DRA, were large heterolateral
661 medulla cells that connected the DRA regions of both hemispheres, crossing the central brain
662 without forming synapses there (Figure 9A). We reconstructed two MeMe-DRA cells, and
663 could not find additional ones, and we matched the morphology of the cell type using light
664 microscopy (Figure 9Aiv). Morphologically, these cells resemble the polarization-sensitive
665 MeMe1 cells characterized in locusts (el Jundi et al. 2011; el Jundi and Homberg 2010). They
666 were exclusively innervated by R7-DRA, receiving 12.0 (mean, range 0 – 21) synapses per
667 seed column, corresponding to 4.9% of total R7-DRA output (Figure 9Aii, Aiii, Table 3,
668 Supplementary File 1). The MeMe-DRA processes in the ipsilateral hemisphere appear to be
669 primarily dendritic, whereas the contralateral processes appear to be axonic (Figure 9Aiii, Aiv).
670 The putative dendritic processes appeared to contact DRA photoreceptors, based on light
671 microscopy labeling, with processes reaching layer M6 exclusively in the DRA region (Figure
672 9Aiv). Intriguingly, the area of medulla columns innervated by a given cell is flipped along the
673 anterior-posterior axis between the two hemispheres, so that the anterior half of the ipsilateral
674 medulla is connected, via the MeMe-DRA cell, with the posterior half of the contralateral
675 medulla and vice versa (Figure 9Av).

676 Another newly identified set of DRA photoreceptor targets were morphologically
677 diverse Mti cells that covered the dorsal medulla (Figure 9B, C, Figure 9 – figure supplement
678 1), for which we also found putative light microscopy matches. All 10 of these Mti-DRA cells
679 were innervated exclusively by R7-DRA, but there were two distinct morphological
680 populations, which we refer to as Mti-DRA1 (Figure 9Bi-Biv) and Mti-DRA2 (Figure 9Ci-Civ).
681 There were six Mti-DRA1 cells with ventral cell bodies (Figure 9Bi) that received together 12.3
682 (mean, range 10 – 14) synapses per seed column, corresponding to 4.4% of total R7-DRA
683 output (Figure 9Bii, Supplementary File 1). Individual reconstructed Mti-DRA1 cells had main
684 processes along the DRA region with short processes innervating non-DRA columns (Figure

685 9Biii, Biv). Mti-DRA2 cells had dorsally located cell bodies (Figure 9Ci) and were more weakly
686 connected to R7-DRA, with four Mti-DRA2 neurons making 5 (mean, range 3 – 8) synapses
687 per seed column, corresponding to 1.8% of R7-DRA total output, (Figure 9Cii– figure
688 supplement 1, Table 3, Supplementary File 1). The main processes of Mti-DRA2 skeletons
689 also innervated the DRA region but these cells formed longer processes extending further
690 ventrally into non-DRA columns (Figure 9Ciii, Civ).
691
692 Comparison of inner photoreceptor connectivity of central and the DRA columns
693 Taken together, our reconstructions of the synapses of the inner photoreceptors
694 specialized for color and polarization vision revealed specific stereotypical similarities, as well
695 as striking differences. The pattern of connectivity between photoreceptor terminals from the
696 same ommatidium, and with Dm9, was highly consistent in columns processing color and
697 polarization, indicating that the mechanisms of lateral inhibition between photoreceptors and
698 gain modulation by Dm9 can serve both modalities (Schnaitmann et al. 2018; Weir et al. 2016;
699 Figure 10A).
700 A second striking similarity was the location of synapses located outside the medulla
701 (Figure 1 – figure supplement 2G). In both the central and DRA columns, more than half of
702 the synapses between the photoreceptors and the inputs to the lamina cells L1 and L3 were
703 outside the medulla (Figure 1 – figure supplement 2G, Figure 2 – figure supplement 1, Figure
704 6 – figure supplement 1A, B, Supplementary File 3). In both cases, the strongest lamina
705 monopolar target was L3, receiving 80% of its inner photoreceptor inputs outside the medulla
706 (Figure 2 – figure supplement 1C, Figure 6 – figure supplement 1B). L3 could contribute to
707 color processing through innervation of Dm9, Tm20, and Tm5c (Takemura et al. 2015), in
708 addition to the ON and OFF pathways computing motion (Silies et al. 2013). Our
709 reconstructions therefore provide further support for the early convergence of motion and color
710 channels, which have until recently been believed to operate separately (Heisenberg and
711 Buchner 1977; Yamaguchi et al. 2008; Wardill et al. 2012; Pagni et al. 2021; Li et al. 2021).

712 Amongst Dm cell types, both R7-DRA and R8-DRA connect to their own modality-
713 specific amacrine-like cell type, Dm-DRA1 and Dm-DRA2, respectively (Sancer et al. 2019).
714 Such connections never occur in the central seed columns, where only R7 connects to Dm8
715 (Figure 10B). Recent studies point towards Dm-DRA1 (and possibly Dm-DRA2) as
716 developmentally similar duplicates of Dm8 cells (Courgeon and Desplan 2019; Sancer and
717 Wernet 2021). Many of the connections to Mi cells are weaker or missing in the DRA region
718 (Figure 10C). Given the role of Mi1, Mi4 and Mi9 in computing motion (Strother et al. 2017),
719 this could indicate a stricter separation between computations of motion and polarization, as
720 compared to motion and color. In contrast, Mi15 cells are targeted by both central and DRA
721 inner photoreceptors. Its role is not known, but its partly dopaminergic neurotransmitter
722 phenotype suggests a modulatory role (Davis et al. 2020). We reconstructed morphologically
723 different Mti cells both from central and DRA columns, and while the Mti cells are R8 targets
724 in the central columns (Figure 3A, B), they are targets of R7 in the DRA region with Mti-DRA1
725 cells having a greater input per seed column than the Mti cells (Figure 9B, C).
726 A striking difference between the central and DRA columns is the absence of most
727 lobula-projecting cells targeted by photoreceptors (Figure 10D). We confirm Tm5a, Tm5b,
728 Tm5c, and Tm20 as targets of central R7 or R8 (Meinertzhagen et al. 2009; Gao et al. 2008;
729 Melnattur et al. 2014), and we also confirm the lack of synaptic connections with these cell
730 types in the DRA region (Sancer et al. 2020). In addition to Tm cells, we identify the new cell
731 type ML1, also connecting the medulla to the lobula but without the precise retinopy of the Tm
732 cell arrays, and with additional branches in the central brain (Figure 10Dii). The lack of Tm
733 and ML1 connectivity in the DRA region is reflected in the overall lower number of R8-DRA
734 synapses (Table 3).
735 R7 and R7-DRA cells are strongly connected to respectively different classes of MeTu
736 cells, whose axon terminals are spatially segregated in the small unit of the AOTU (Figure
737 10E; Timaeus et al. 2020). These data support previous proposals of parallel pathways to the
738 central brain via the AOTU (Otsuna et al. 2014; Omoto et al. 2017; Timaeus et al. 2020; Tai
739 et al. 2021). Besides the AOTU, photoreceptor targets in the central and DRA columns both

740 project to the PLP, but otherwise they show little overlap in the central brain areas they project
741 to (Figure 10F). The additional contacts of DRA region projection neurons are focused in the
742 lateral horn and the contralateral medulla, while the central column projection neurons
743 innervate widely across the central brain, including the mushroom bodies, and the
744 contralateral lobula plate. A key modality-specific feature of the visual projection neurons is
745 the dominance of R8 input in the central columns, and R7 in the DRA region (Figure 11A).
746
747 Cell types distinguishing between pale and yellow inputs
748 The fly's retinal mosaic can support circuits with different chromatic sensitivities by
749 selective sampling of pale and yellow photoreceptors. For example, cells contrasting pale and
750 yellow R7 input would be expected to have high chromatic sensitivity around ~350 nm, where
751 the spectral sensitivity of Rh3 and Rh4 overlap (Salcedo et al. 1999). Our reconstructions
752 revealed several cases of connectivity patterns that could support such selective sampling.
753 For R7, these included two cell types previously reported to be pale- or yellow-selective: Tm5a
754 for yellow R7 (Karuppudurai et al. 2014), and Tm5b for pale R7 (Menon et al. 2019; Figure
755 11Bi). By completely reconstructing several Dm8 cells for the first time (Figure 2C), we found
756 that Dm8 neurons were most highly innervated by R7 in their home columns, with
757 approximately equal sampling of pale and yellow R7 input in the surrounding columns. Unlike
758 in the DRA region, there were no cells projecting to the central brain that were substantial
759 targets of R7. Examining the encoding of chromatic signals in Tm5a/b and Dm8 cells, and
760 their other synaptic partners, is therefore a promising avenue for addressing the open question
761 of how, or if, UV information from yellow ommatidia is processed differently from UV signals
762 downstream of pale R7 cells.
763 We found more pale-yellow selective cells among the R8 targets. Two visual projection
764 neurons were newly identified as selective for pale R8 input, the aMe12 and ML-VPN1 cells.
765 ML-VPN1 provides input to the PLP, while aMe12 has presynaptic sites in the accessory
766 medulla, the PLP, and the mushroom body, where it provides input to γd Kenyon cells (Li et
767 al. 2020; Scheffer et al. 2020). These connectivity patterns suggest roles in circadian

768 entrainment and learning and memory, respectively (Figure 11Bii). *Drosophila* pale R8 cells
769 are most sensitive to blue wavelengths (Sharkey et al. 2020; Salcedo et al. 1999; Schnaitmann
770 et al. 2018; Heath et al. 2020), and the projections of aMe12 and ML-VPN1 demonstrate that
771 blue light is processed and used by the central brain within one synapse. Little is known about
772 the central processing of color in *Drosophila* (Longden 2016), but the detection of blue light
773 plays an important role in the circadian avoidance of bright light (Lazopulo et al. 2019). Flies
774 can also learn to discriminate between large areas of blue and green light and a group of
775 visual projection neurons have been reported to provide input to γd Kenyon cells and be
776 required for this ability (Vogt et al. 2014).

777 While near perfect specificity for pale versus yellow inputs appears to be limited to a
778 few cell types, several strongly connected cell types show strongly biased inputs: For example,
779 Dm2 favors pale over yellow R8 (60:15), and Tm5c favors yellow over pale R8 (103:20) a
780 result that corroborates and extends the findings of the 7-column medulla connectome.
781 Individual cells, in particular Tm20 neurons, that span just one column, are also constrained
782 to be selective for pale and yellow photoreceptor input. Such selectivity could in principle be
783 exploited at the level of the synaptic targets of these neurons. Surprisingly, Mi9 cells, another
784 cell type present in every column of the eye, also revealed strong pale/yellow biases in our
785 reconstructions, both with R7 inputs (3:9), as well as R8 inputs (26:1). Given the known role
786 of Mi9 in shaping direction-selective responses on T4 dendrites (Strother et al. 2017;
787 Takemura et al. 2017), these data identify yet another level of crosstalk between chromatic
788 and motion-sensitive channels. Overall, it is an unexpected finding that most projections from
789 the medulla to the lobula from photoreceptor target neurons convey biased pale/yellow inputs.
790 These differences could mediate much broader effects of pale/yellow differences in medulla
791 and lobula circuits than currently appreciated, or these specializations could be blunted by
792 combinations at the next synaptic layer.

793

794 **Discussion**

795 Our systematic reconstruction of all synaptic inputs and outputs of identified,
796 functionally specialized *Drosophila* photoreceptors (pale and yellow R7-8, R7-DRA and R8-
797 DRA) provides a comprehensive inventory of the first steps of the color and polarization
798 pathways, from which all the computations of the dependent behaviors stem. These data
799 revealed core connectomic motifs shared across column types (Figure 10A-C), multiple new
800 photoreceptor targets, and uncovered additional cell types as being connected to specific
801 photoreceptor subtypes conveying specific color and polarization information to the central
802 brain (Figure 10E, F).
803
804 Inner photoreceptor connections outside the medulla neuropil
805 We confirmed previously reported synaptic partners of the inner photoreceptors in the
806 central medulla (Figure 1-supplement 2) and identified new photoreceptor targets. As prior
807 reconstructions were incomplete (Takemura et al. 2015), it was unclear whether the
808 unidentified connections were mainly onto new target neurons or represented more
809 connections onto known cell types; our reconstructions revealed both types of omissions. One
810 functionally important set of missed connections are the synapses between inner
811 photoreceptors from the same central and DRA ommatidia, which we found to be stronger
812 than previously reported (Takemura et al. 2008, 2015), due to significant numbers of synapses
813 outside the medulla. These synapses likely contribute to color-opponent responses seen in
814 central R7 and R8 terminals (Schnaitmann et al. 2018) and the polarization-opponent signals
815 measured from DRA photoreceptors (Weir et al. 2016). Our reconstructions also support a
816 larger scale opponent process mediated by multi-columnar Dm9 cells (Heath et al. 2020),
817 which also formed some synapses outside the medulla neuropil.
818 Other cell types also received inner photoreceptor input outside the medulla, notably
819 the lamina monopolar cells L1 and L3. These lamina connections indicate that chromatic
820 comparisons arising from R7 and R8 may feed into the motion vision pathway, and identifies
821 a new site for interplay between the ‘color’ and ‘motion’ pathways (Wardill et al. 2012;
822 Schnaitmann et al. 2013; Pagni et al. 2021; Li et al. 2021). Together, these observations

823 suggest that synapses in an unexpected location, outside the main synaptic layer of the
824 medulla, could play a significant role in early visual processing.
825
826 Newly identified targets of central versus DRA inner photoreceptors
827 In the central medulla, we found, for the first time in an EM study, strong synaptic
828 connections between R7s and MeTu cells that project to the AOTU (Figure 11Ai), confirming
829 previous claims based on light microscopy (Timaeus et al. 2020). This finding may reconcile
830 disparate observations, such as a role in wavelength-specific phototaxis for cells matching
831 MeTu morphology (Otsuna et al. 2014), as well as measurements of color-sensitive signals in
832 the AOTU of bees (Mota et al. 2013). Previous anatomical studies partitioned MeTu cells into
833 distinct subclasses that terminate in discrete subdomains of the AOTU (Omoto et al. 2017;
834 Timaeus et al. 2020; Tai et al. 2021). Here, we identified modality-specific MeTu-DRA cells
835 that only integrate from the polarization-sensitive R7-DRA photoreceptors, while avoiding
836 synaptic contacts with color-sensitive pale or yellow R7s. Our MeTu and MeTu-DRA cells
837 target adjacent subdomains within the small unit of the AOTU (Figure 10E), in agreement with
838 proposals that parallel channels convey different forms of visual information from the eye to
839 the central complex via the AOTU (Hardcastle et al. 2021; Hulse et al. 2020; Timaeus et al.
840 2020; Omoto et al. 2017).
841 We also identified connections from inner photoreceptors to several cell types either
842 not previously described, or not known to be photoreceptor targets, thus setting up a clear
843 expectation that these cells should contribute to color or polarization vision. ML1 is a new,
844 major target of R8, a cell type that connects the medulla to the lobula via a previously
845 unknown, non-columnar pathway, and the central brain (Figure 4D, Figure 11Aii). Previous
846 studies have identified an important role for Tm5a/b/c and Tm20 cell types for chromatic
847 processing in the lobula (Lin et al. 2016; Gao et al. 2008), and we have confirmed that these
848 cell types are targets of R7-8. Whether these Tm neurons and ML1 cells have common targets
849 in the lobula, feed into shared central pathways or contribute to separate channels remain

open questions; the lobula arbors of the Tm and ML1 cells are mostly in different layers arguing against direct synaptic interactions between the cells.

The reconstruction of DRA photoreceptor targets confirmed the modality-specific connectivity of Dm-DRA cell types within layer M6: Dm-DRA1 to R7-DRA, and Dm-DRA2 to R8-DRA (Figure 11A). The R7-DRA and R8-DRA cells respond to orthogonal orientations of polarized light at each location of the DRA, so Dm-DRA1 and Dm-DRA2 likely process orthogonal e-vector orientations spatially averaged by pooling over ~10 ommatidia (Weir et al. 2016). Our data also revealed additional DRA pathways into the PLP in the central brain via VPN-DRA cells, as well as to the contralateral DRA, via MeMe-DRA cells (Figure 10F). Such interhemispheric connections have been demonstrated in larger insects (el Jundi et al. 2011; Labhart 1988), but not in *Drosophila,* and their synaptic input was not known. Interocular transfer contributes to navigation by desert ants that can see the celestial polarization but not visual landmarks (Wehner and Muller 1985), but the interactions between the DRA regions remain poorly understood. The identification of MeMe-DRA neurons may enable the mechanisms of such phenomena to be explored.

For color vision, we have confirmed the pale-yellow specificity of Tm5a and Tm5b cells (Figure 11Bi). We have additionally identified as pale-specific the aMe12 and ML-VPN1 cell types, and the yellow bias of Tm5c and the pale bias of Mi9 (Figure 11Bii). Our detailed analysis of Dm8 inputs confirmed that these neurons receive most of their photoreceptor input in a central home column, consistent with pale and yellow subtypes of Dm8 cells having distinct chromatic properties (Courgeon and Desplan 2019, Menon et al. 2019, Li et al. 2021, Pagni et al. 2021). The selective photoreceptor input to these cell types, combined with input to columnar cells from a single photoreceptor subtype, indicate that wavelength-specific information is maintained in the medulla and lobula (Figure 11Bi). The projections of aMe12 and ML-VPN1 to the central brain indicate the possibility that wavelength-specific photoreceptor responses are directly conveyed into the central brain by these cells, although they likely integrate input from other chromatically sensitive cell types (Figure 11Bii).

878

879 Limitations of our approach

880 By focusing on a small number of columns, we have delivered a near complete picture
881 of local connectivity, but we cannot rule out the possibility that certain cell types may have
882 been overlooked. For instance, we chose an arbitrary threshold of 2-3 synapses below which
883 we did not endeavor to reconstruct synaptic targets to the extent required to uniquely identify
884 them. As a result we may, in principle, have missed large cells that receive small, but
885 significant inputs across many columns. Furthermore, we cannot rule out regional
886 specializations in the optic lobes, such that specific cell types might be found outside of our
887 seed columns. For example, some MeTu cells are only found in the dorsal third of the medulla
888 (Omoto et al. 2017; Otsuna et al. 2014), where incoming R7 cells are known to co-express
889 Rh3 and Rh4 Rhodopsins (Mazzoni et al. 2008).

890

891 Complementary usage of multiple connectomic data sets and outlook

892 Taken together, the data presented here provides access to the full complement of R7
893 and R8 photoreceptor targets from functionally specialized optical units. By reconstructing
894 these local circuits within a full-brain EM volume, we were able to establish the complete
895 morphology of large, multi-columnar cell types, that are strongly connected to photoreceptors,
896 but had eluded previous connectomic reconstruction efforts (Takemura et al. 2013, 2015). The
897 sparse tracing approach we have implemented and described here enabled efficient
898 identification of the complete set of upstream and downstream partners of the inner
899 photoreceptors, in a manner that is complementary to the dense connectomes generated from
900 smaller-scale medulla volumes. As an example of this synergistic usage of complementary
901 data sets, we have returned to the 7-column data (Takemura et al. 2015; Clements et al. 2020)
902 and used our whole-cell morphologies to match the bodies of previously unidentified
903 photoreceptor targets. In that process we have established strong candidates for MeTu, ML1,
904 and perhaps for aMe12 (see Materials and Methods) and confirmed several aspects of their
905 connectivity in FAFB. In so doing, we now have access to the additional connectivity data

provided by the 7-column dense reconstruction. While full exploration and follow-up analyses of these combined data is beyond the scope of this work, the FIB-SEM/FAFB combination revealed several intriguing connectivity patterns, including new candidate paths for the integration of output from different photoreceptor types. For example, the MeTu cells that are postsynaptic to R7 also receive indirect R8 input via the R8 target Mi15, and ML1 combines direct R8 input with indirect input from outer photoreceptors via lamina neurons. As further connectome data sets are completed, this comparative interplay between data sets with unique advantages and limitations, will be an important step in both cross-validating and extending the applicability of all related data sets.

Our reconstruction of the DRA photoreceptor targets provides the first EM-based connectomic data set for modality-specific cell types likely to process skylight information in any insect and will be important for developing refined models of skylight navigation (Gkanias et al. 2019). Core motifs shared between DRA and central columns such as opponency are prime candidates for circuit elements that perform computations, such as establishing opponency, that are key for both polarization and color processing, whereas cell types with preferential connections to either pale of yellow columns are promising candidates for the study of specific aspects of color processing in the insect brain. This comprehensive catalog of the neurons carrying signals from R7 and R8 photoreceptors deeper into the brain establishes a broad foundation for further studies into the mechanistic basis of color vision and its contributions to perception and behavior.

926 **Materials & Methods**

Key Resources Table				
Reagent type (species) or resource	**Designation**	**Source or reference**	**Identifiers**	**Additional information**
genetic reagent (*Drosophila melanogaster*))	MCFO-1; ”pBPhsFlp2::PEST in attP3; ;pJFRC201-10XUAS-FRT>STOP>FRT-myr::smGFP-HA in VK0005, pJFRC240-10X-UAS-FRT>STOP>FRT-myr::smGFP-V5-THS-10XUAS-FRT>STOP>FRT-myr::smGFP-FLAG in su(Hw)attP1”	https://doi.org/10.1073/pnas.1506763112	RRID:BDSC_64085	
genetic reagent (*Drosophila melanogaster*))	pJFRC51-3XUAS-IVS-Syt::smHA in su(Hw)attP1, pJFRC225-5XUAS-IVS-myr::smFLAG in VK00005	https://doi.org/10.1073/pnas.1506763112		
genetic reagent (*Drosophila melanogaster*)	SS02978	This study	SS02978	For further details on driver lines see Table S1. Driver lines will be available via https://www.janelia.org/split-GAL4.
genetic reagent (*Drosophila melanogaster*)	SS01015	This study	SS01015	For further details on driver lines see Table S1. Driver lines will be available via https://www.janelia.org/split-GAL4.
genetic reagent (*Drosophila melanogaster*)	SS28175	This study	SS28175	For further details on driver lines see Table S1. Driver lines will be available via https://www.janelia.org/split-GAL4.
genetic reagent (*Drosophila melanogaster*)	R56F07	Bloomington Drosophila Stock Center	RRID:BDSC_39160	
genetic reagent (*Drosophila melanogaster*)	ortc2b-Gal4	https://doi.org/10.1016/j.neuron.2013.12.010		

genetic reagent (*Drosophila melanogaster*)	20XUAS-CsChrimson-mVenus in attP18	https://doi.org/10.1038/nmeth.2836	RRID:BDSC_55134	
antibody	anti-chaoptin mouse monoclonal 24B10	DSHB	RRID:AB_528161	
antibody	anti-Brp mouse monoclonal nc82	DSHB	RRID:AB_2314866	
antibody	anti-dsRed rabbit polyclonal	Clontech Laboratories, Inc.: 632496	RRID:AB_10013483	
antibody	Rat cadherin, DN-Ex #8(extracellular domain)	Developmental Studies Hybridoma Bank	RRID: AB_528121	(1:100)
antibody	anti-HA rabbit monoclonal C29F4	Cell Signaling Technologies: 3724S	RRID:AB_1549585	
antibody	anti-FLAG rat monoclonal DYKDDDDK Epitope Tag Antibody [L5],	Novus Biologicals: NBP1-06712	RRID:AB_1625981	
antibody	DyLight 550 conjugated anti-V5 mouse monoclonal	AbD Serotec: MCA1360D550GA	RRID:AB_2687576	
antibody	DyLight 549 conjugated anti-V5 mouse monoclonal	AbD Serotec: MCA1360D549GA	RRID:AB_10850329	
antibody	anti-GFP rabbit polyclonal	ThermoFisher: A-11122	RRID:AB_221569	
antibody	anti-GFP mouse monoclonal 3E6	ThermoFisher: A-11120	RRID:AB_221568	
Software, algorithms	FluoRender	http://www.sci.utah.edu/software/fluorender.html		

Software, algorithms	VVDviewer	https://github.com/takashi310/VVD_Viewer		
Software, algorithm	Python 3	http://www.python.org	RRID:SCR_008394	
Software, algorithm	pymaid	https://github.com/schlegelp/PyMaid		python library
Software, algorithm	FAFBseg	https://github.com/flyconnectome/fafbseg-py		python library
Software, algorithm	R	https://www.r-project.org/		
Software, algorithm	R Studio	https://www.rstudio.com/		
Software, algorithm	Natverse	https://natverse.org	DOI: 10.7554/eLife.53350	collection of R packages for neuroanatomical analysis
Software, algorithm	Tidyverse	https://www.tidyverse.org/		R package
Software, algorithm	knitr	https://cran.r-project.org/package=knitr		R package
Software, algorithm	kableExtra	https://cran.r-project.org/package=kableExtra		R package

Software, algorithm	gridExtra	https://cran.r-project.org/package=gridExtra		R package
Software, algorithm	png	https://cran.r-project.org/package=png		R package
Software, algorithm	RColorBrewer	https://cran.r-project.org/package=RColorBrewer		R package
Software, algorithm	alphashape3d	https://CRAN.R-project.org/package=alphashape3d		R package
Software, algorithm	Fiji	http://fiji.sc	RRID:SCR_002285	
Software, algorithm	MATLAB			
Software, algorithm	CATMAID	www.catmaid.org		neuron reconstruction
other	FAFB	Zheng et al. 2018; https://v2.virtualflybrain.org/		EM data set
other	FAFB-FFN1	Li et al. 2020; http://fafb-ffn1.storage.googleapis.com/data.html		EM auto-segmentation
other	FlyWire	Dorkenwald et al. 2020; https://flywire.ai/		EM auto-segmentation

Sequence-based reagent	Rh3 F	This paper	PCR primer	CACC GGT ACG CTT ATG ATA ACC TTC G
Sequence-based reagent	Rh3 R	This paper	PCR primer	GCT CCG GTC TGC GGG CCA AGA
Sequence-based reagent	Rh5 F	This paper	PCR primer	CACC GGT GAT TAA TGC GAA TGT AGC TGC
Sequence-based reagent	Rh5 R	This paper	PCR primer	ACT GCT TGA TCC GCT CCA AAA TC
Sequence-based reagent	Rh6 F	This paper	PCR primer	CA CCA ACA TGA TGG CGG ACA TCA C
Sequence-based reagent	Rh6 R	This paper	PCR primer	TTC GAA TGG CTG GTA CTG GTG

927

928 EM reconstruction

929 The FAFB data set is a serial section transmission EM volume of a female *Drosophila*
930 *melanogaster* brain (Zheng et al. 2018). We manually reconstructed neurons in this volume in
931 the CATMAID environment, which includes a browser-based annotation interface and a server
932 hosting a copy of the data (Saalfeld et al. 2009). We also searched for neurons using two
933 recent auto-segmentations FAFB-FFN1 (Li et al. 2020) and FlyWire (Dorkenwald et al. 2020),
934 importing some of the FAFB-FFN1 auto-segmentation fragments afterwards into the
935 CATMAID environment, a process that facilitated the identification of a small number of
936 neurons. We followed established guidelines for manually tracing neuron skeletons,
937 annotating synaptic connections, and reviewing reconstructed cells (Schneider-Mizell et al.
938 2016). We completely reconstructed the morphology of pairs of R7 and R8 cells in 7 “seed”
939 columns, 4 adjacent columns chosen to be near the center of the retinal mosaic, and 3

940 columns in the dorsal rim area (Figure 1C). On the R7 and R8 cells, we annotated as a "pre-
941 synapse" all the locations where there was a T-bar (Figure 1 – figure supplement 1A).
942 Associated with each pre-synapse we annotated a "post-synapse" connection with every
943 synaptic partner. These seed neurons and their pre-synapses were completely proofread by
944 independent team members, a process that amounted in small (<10%) amendments to the
945 connectivity data presented here.

946 In total, we identified 4043 connections from the seed column R7 and R8 cells to 422
947 postsynaptic skeletons (the vast majority of which correspond to individual neurons), including
948 the 14 R7-8 cells. We reconstructed their morphology to be able to identify the cell type (e.g.
949 Dm8, Mi1, Tm5a) or cell class (e.g. Dm, Mi, Tm) of 299 cells, whose synapses accounted for
950 96.2% (3888/4043) of the total synaptic output. For all but one cell, we applied a threshold of
951 >2 synapses to focus our reconstructions on reliable connections – the exception was the Mt-
952 VPN2 cell, which had a large dendritic field and so may integrate many sparse R7 and R8
953 inputs (Figure 5 – figure supplement 1). There were 244 cells with >2 synapses, of which 224
954 were identified to cell type, 16 were identified to cell class, giving a total of 240 identified cells
955 (224 + 16 cells), and the remaining 4 were unidentified (Tables 1 and 3). The 240 identified
956 cells with >2 synapses accounted for 94% (3803/4043) of the total synapses. The 16 cells
957 reconstructed to cell class were sparsely connected, with 4.9 synapses per cell (mean, 79
958 synapses total). The R7 and R8 cells make infrequent synaptic contacts with glia as well as
959 neurons (Figure 1 – figure supplement 1C), but we did not systematically trace the glia
960 connections.

961 The 244 cells with >2 synapses were the focus of our analysis, and their connections
962 are summarized in Tables 1 and 3; the connections of individual cells are also organized by
963 cell type for incoming and outgoing synapses in Supplementary File 1. In addition, the
964 morphologies and connections of individual cells with >1 synapses are shown in the gallery
965 figures (Supplementary File 2). Most neurons could be uniquely identified with incomplete
966 reconstructions. Nevertheless, it is useful to establish a reference morphology data and so we
967 completely reconstructed individual examples of specific cell types, in addition to the seed R7

968 and R8 cells, and in some cases multiple examples. In the central columns, there were 14
969 completely reconstructed neurons: Dm2, Dm8 (3 cells), Dm9, Dm11, MeTu, Mi15, ML1, ML-
970 VPN1, Tm5a, Tm5b, Tm5c (2 cells). In the DRA, there were 10 completely reconstructed
971 neurons: Dm-DRA1 (4 cells), Dm-DRA2 (3 cells), and MeTuDRA (3 cells). We believe that a
972 number of these cell types we reconstructed have not been previously described: aMe12,
973 ML1, ML-VPN1, and ML-VPN2 in the central columns; MeMe-DRA, MeTu-DRA, DRA-VPN
974 and Mti-DRA in the DRA region. For one cell whose morphology was similar to the described
975 Tm5a cell type, but whose connectivity was markedly different from the others, we annotated
976 this cell as Tm5a-like. Likewise, for three cells whose morphology was similar to the described
977 Tm5b cell type, but whose connectivity was markedly different from that reported by (Menon
978 et al. 2019), we annotated these cells as Tm5b-like. There were numerous tangential cells
979 contacted in the central and DRA columns that do not match those characterized in previous
980 anatomical studies (Fischbach and Dittrich 1989). We have annotated these as medulla
981 tangential intrinsic (Mti) cells when the cells have processes intrinsic to the medulla, and as
982 medulla tangential visual projection neurons (Mt-VPNs) when they project to neuropils outside
983 the medulla.

984 We additionally identified 970 incoming synapses to the seed column R7-8 cells from
985 56 cells, including the 14 R7-8 cells. All the 30 cells providing >2 synapses were reconstructed
986 so that we could ascribe a cell type, and these cells provided 96% (936/970) of the total
987 incoming synapses (Tables 2,4). In total, we identified the presynaptic cell type of 99%
988 (963/970) of the synapses onto the R7-8 cells (including the 1-synapse contributing cells). All
989 but 1 of the cells providing >2 synapses were themselves contacted by the seed column R7-
990 8 cells, the exception being a DRA C2 cell that provided 5 synapses (Supplementary File 1).
991 Including this C2 cell, there were 245 cells with >2 input or output synapses with the seed
992 column photoreceptors (244 + 1 cells).

993 This report was focused on identifying the synaptic inputs and outputs of the R7 and
994 R8 cells of the central and DRA columns, and it was not feasible to also detail the circuit
995 connectivity for the cells targeted by these photoreceptors. For exceptional cell types,

996 however, we traced more than the cells' connections to the seed column R7 and R8 cells. 1)
997 We traced three aMe12 cells to near completion, to determine the columns that contained the
998 cell type's characteristic vertical processes that we used to determine whether a column was
999 pale or not (see below). 2) We traced all the photoreceptor inputs to three Dm8 cells in the
1000 central columns (Figure 2Cii-iii). 3) For the Mt-VPN1 cell, we reconstructed the photoreceptor
1001 inputs in 20 medulla columns to discount the possibility that this was a pale-specific neuronal
1002 target in the central columns. 4) For three fully reconstructed Dm-DRA1 cells and three fully
1003 reconstructed Dm-DRA2 cells we traced all their R7-DRA and R8-DRA inputs (Figure 6E,F).
1004 5) For one Dm9 cell innervated by R7-DRA and R8-DRA, we traced in non-DRA columns to
1005 confirm that Dm9 cells in the DRA also receive non-DRA photoreceptor input (Figure 6Cvi).
1006
1007 Defining pale, yellow and DRA medulla columns
1008 To identify medulla columns, we used a map of Mi1 neurons. This Mi1 map, which we
1009 have generated for a separate, ongoing study, includes nearly all Mi1 neurons in the medulla
1010 of the right hemisphere of the FAFB volume. The Mi1 cell type is columnar, with one cell per
1011 column and unambiguous arborizations in medulla layer 1, 5, 9 and 10 (Fischbach and Dittrich
1012 1989). We defined the location of a column in the medulla as the center-of-mass of the Mi1
1013 dendrite in layer 5 (Figure 1C, 2A).
1014 We traced the vertical dendritic branches of all three aMe12 cells in the data set. Their
1015 vertical branches innervate pale columns (Figure 1D), and so we labelled the columns they
1016 occupied (by proximity to the nearest Mi1-defined column) as pale columns (Figure 1C). The
1017 aMe12 cells have short vertical branches reaching from M6 to M3 and longer vertical branches
1018 reaching up to M1 (Figure 1Dii, Eiii). Both the long and short vertical processes were used to
1019 assign pale medulla columns. Nearly all the assigned pale columns were innervated by one
1020 aMe12 cell, but three columns were innervated by two cells. Using this system, the columns
1021 not innervated by aMe12 were yellow candidates (Figure 1C). Despite extreme care and
1022 multiple reviews of the aMe12 neurons, errors of omission are always possible in the manual
1023 reconstruction procedure, and so we are confident that the 'pale' identified columns are

1024 innervated by aMe12, however, it is possible that a small number of the 'yellow' columns are
1025 mis-classified. The aMe12 cells innervated just 1 of the 42 identified DRA columns (Figure
1026 1C). While most medulla columns innervated by R7-8 are pale or yellow, there are a small
1027 number of ommatidial cartridges with other identities, for example rare (~1-2 per fly)
1028 ommatidial pairs of R7 and R8 cells expressing Rh3 and Rh6, respectively (Chou et al. 1996).
1029 The congruence of the pale- and yellow-specificity we observed for Tm5a, aMe12 and ML-
1030 VPN1 cell types indicated that our allocation of pale columns in the central columns was
1031 robust, and consistent with the previous report of the yellow-specificity of Tm5a cells
1032 (Karuppudurai et al. 2014).

1033 To identify the DRA columns, we reconstructed the R7 and R8 cells in 27 columns
1034 along the dorsal-rim-corresponding margin of the medulla and ascertained whether the R8
1035 cell terminated in the same layer as the R7 cell (Figure 1E, arrow; Figure 1 – figure supplement
1036 1A). The R8-DRA cells terminate before the R7-DRA cells in this layer, allowing the two cell
1037 types to be distinguished. By careful visual inspection of the M6 layer of all medulla columns
1038 located close to the dorsal edge of the medulla we identified 15 additional DRA columns
1039 resulting in a total of 42 DRA columns which is in good agreement with the previously reported
1040 average number of 39 DRA columns (Weir et al. 2016; Figure 1C).

1041

1042 Analysis of synapse locations

1043 To define the medulla and lobula layers, we first used the R package collection
1044 "natverse" (Bates et al. 2020) to transform pre-defined neuropil meshes (Jenett et al. 2012;
1045 Bogovic et al. 2019) into the FAFB space. Our meshes for the medulla and lobula computed
1046 in this way defined the top and bottom layers of these neuropils. We then interpolated the
1047 initial internal layer boundaries using demarcations established in prior studies (Takemura et
1048 al. 2015; Wu et al. 2016). Finally, we refined the layer boundaries using the characteristic
1049 arborizations patterns of the Mi1, C2, Tm5 and Tm20 cell types (Gao et al. 2008; Fischbach
1050 and Dittrich 1989). For the medulla, the demarcations were: 0%, 8.2%, 26.2%, 36.1%, 45.9%,
1051 54.1%, 62.3%, 67.2%, 76.2%, 91.0%, 100%. For the lobula the layer demarcations were: 0%,

1052 4.2%, 11.3%, 22.4%, 37.4%, 49.4%, 64.7%, 100%. The layer designations are therefore
1053 guides to aid interpretations and comparisons, and not measurements of the neuropils
1054 themselves.

1055 To plot the histograms of the synaptic depths in the medulla (e.g. Figure 1Eiii, we took
1056 the projection of the synapse locations along the columnar axis, and smoothed this distribution
1057 of synaptic depths with a zero-phase Gaussian filter with a standard deviation of 0.4 μm. For
1058 the histograms of distances of R7 synapses to each Dm8 cell's home column (Figure 2Ciii),
1059 we took the projection of the synapse locations onto the plane perpendicular to the columnar
1060 axis and calculated the distance in that plane to the column center. The resulting distribution
1061 of distances was then smoothed with a zero-phase Gaussian filter with a standard deviation
1062 of 0.6 μm.

1063 For the histograms of the distances along the DRA of photoreceptor synapses to Dm-
1064 DRA1 and Dm-DRA2 cells (Figure 7B, D), we first fitted an ellipse to the centers of DRA
1065 columns, using least squares regression (Figure 7 – figure supplement 3Ai). We then
1066 calculated the location of the perpendicular projection of every synapse along the fitted ellipse
1067 (Figure 7 – figure supplement 3Aii-iv). Finally, these distances were filtered with a zero-phase
1068 Gaussian filter with a standard deviation of 0.6 μm.

1069

1070 <u>Comparison with 7-column medulla FIB-SEM data set</u>

1071 To compare the connectivity of R7 and R8 of our central column reconstructions with
1072 the connectivity identified in the medulla FIB-SEM data set (Takemura et al. 2013, 2015), we
1073 took advantage of the identification of pale and yellow columns in that data set used by (Menon
1074 et al. 2019). That study used the presence or absence of Tm5a to indicate yellow and pale
1075 columns, respectively, and excluded columns that contained Tm5 neurons that were
1076 ambiguous for being Tm5a or Tm5b neurons. Using this scheme, columns B, D and H are
1077 pale, and columns A, E and F are yellow (here using the column references used for the 7-
1078 column data set). The 7-column medulla data set is now publicly available and accessible with

1079 the release of NeuPrint (Clements et al. 2020), and we used NeuPrint to compile the
1080 connectivity of cells with pale and yellow R7 and R8 cells from the data set (Figure 1 – figure
1081 supplement 2). The unidentified cells, including cells annotated as output ('out') and fragments
1082 of putative tangential cells ('tan') in the six pale and yellow columns are 38.1% for R7
1083 (518/1342 synapses over 6 columns) and 38.9% for R8 (726/1854 synapses over 6 columns).
1084 We also searched the FIB-SEM data set for neurons with shapes and patterns of
1085 connectivity similar to aMe12, ML1, and MeTu neurons and identified the following putative
1086 matches (NeuPrint medulla7column identifiers in parenthesis): aMe12 (54028), ML1(16666),
1087 MeTu (11770; annotated as an unknown Tm; 35751 and other reconstructions annotated as
1088 'Dm7'). The ML1 and MeTu matches are further supported by multiple inputs other than R-
1089 cells (e.g. L3, L4 and Dm9 to ML1 and Mi15 to MeTu) that are present in both data sets. These
1090 matches provide examples of how the combination of our complete but focused
1091 reconstructions and the dense but strongly volume-limited FIB-SEM data can together enable
1092 insights that go beyond each individual data set.
1093
1094 Genetics and molecular biology
1095 Fly genotypes
1096 Fly genotypes used throughout the manuscript are listed organized by Figure Panel
1097 in Supplementary File 4.
1098
1099 Driver lines
1100 Split-GAL4 lines were constructed and characterized as in previous work (Wu et al.
1101 2016). Briefly, we tested candidate AD and DBD hemidriver pairs (Tirian and Dickson 2017;
1102 Dionne et al. 2018). for expression in cell types of interest and assembled successful
1103 combinations into stable fly strains that were then used for subsequent experiments. Split-
1104 GAL4 lines generated in this study and images of their expression patterns will be made
1105 available online (https://www.janelia.org/split-GAL4). aMe12, ML1 and ML-VPN1 were initially
1106 identified by light microscopy, allowing us to generate split-GAL4 driver lines targeting these

1107 previously undescribed cell types. Images of cells labeled by these driver lines were
1108 subsequently matched to the EM reconstructions. Split-GAL4 lines labeling Dm11, Mi15, L2
1109 and VPN-DRA were from prior work (Davis et al. 2020; Tuthill et al. 2013; Wu et al. 2016). The
1110 candidate VPN-DRA driver (OL0007B) was originally described as a split-GAL4 driver for a
1111 different cell type (LC12; Wu et al. 2016) but also labels neurons highly similar or identical to
1112 VPN-DRA. We also used GAL4 driver lines from the Janelia and Vienna Tiles collections
1113 (Jenett et al. 2012; Tirian and Dickson 2017).
1114
1115 Rhodopsin-LexA reporter constructs
1116 To construct Rh3-, Rh5- and Rh6-LexA driver lines, we amplified previously
1117 characterized promoter regions (Mollereau et al. 2000; Pichaud and Desplan 2001; Tahayato
1118 et al. 2003; Chou et al. 1996; Papatsenko et al. 1997; Huber et al. 1997) by PCR from genomic
1119 DNA. Primer sequences are listed in the Key Resources Table. The PCR products were
1120 TOPO-cloned into pENTR-D-TOPO (Invitrogen) and transferred to pBPnlsLexA::GADflUw
1121 (addgene #26232) using standard Gateway cloning. Transgenic flies were generated by
1122 phiC31-mediated integration into the attP40 landing site (injections were done by Genetic
1123 Services, Inc).
1124
1125 Histology
1126 To characterize the neurons labeled by split-GAL4 lines, we visualized both overall
1127 expression patterns and individual cells. For the former, we used we pJFRC51-3XUAS-IVS-
1128 Syt::smHA in su(Hw)attP1 and pJFRC225-5XUAS-IVS-myr::smFLAG in VK00005 (Nern et al.,
1129 2015) or 20XUAS-CsChrimson-mVenus in attP18 (Klapoetke et al. 2014) as reporters; the
1130 latter was achieved by stochastic labeling of individual cells with MCFO (Nern et al. 2015).
1131 Specimens were processed and imaged by the Janelia FlyLight Project team following
1132 protocols that are available online (https://www.janelia.org/project-team/flylight/protocols
1133 under “IHC - Anti-GFP”, “IHC - Polarity Sequential”, “IHC – MCFO and “DPX mounting”).
1134 Additional MCFO images of cells labeled by GAL4 (instead of split-GAL4) driver lines were

1135 generated in the same way. Images were acquired on Zeiss LSM 710 or 780 confocal
1136 microscope using 20x 0.8 NA or 63x 1.4 NA objectives.
1137 The specimens shown in Figures 7Aiii, 7Ciii, 8Aii and 8v were prepared and imaged
1138 as previously described (Sancer et al 2019).
1139 For the combined labeling of aMe12, ML-VPN1 and VPN-DRA with photoreceptor
1140 markers, fly brains were processed using standard immunolabeling protocols as previously
1141 described in (Davis et al. 2020). Briefly, flies were dissected in insect cell culture medium
1142 (Schneider's Insect Medium, Sigma Aldrich, #S0146) followed by fixation with 2% PFA (w/v;
1143 prepared from a 20% stock solution, Electron Microscopy Sciences: 15713) in cell culture
1144 medium for 1 h at room temperature. This fixation step and the subsequent primary and
1145 secondary antibody incubations were each followed by several washes with PBT (0.5 % v/v
1146 TX-100, Sigma Aldrich: X100, in PBS). To block nonspecific antibody binding, brains were
1147 incubated in PBT-NGS (5% Goat Serum ThermoFisher: 16210-064 in PBT) for at least 30 min
1148 prior to addition of primary antibodies in PBT-NGS. Primary and secondary antibody
1149 incubations were at 4°C overnight, all other steps were at room temperature. Brains were
1150 mounted in SlowFadeGold (ThermoFisher: S36937).
1151 Primary antibodies were anti-GFP rabbit polyclonal (ThermoFisher: A-11122,
1152 RRID:AB_221569; used at 1:1000 dilution), anti-GFP mouse monoclonal 3E6 (ThermoFisher:
1153 A-11120, RRID:AB_221568; dilution 1:100), anti-dsRed rabbit polyclonal (Clontech
1154 Laboratories, Inc.: 632496, RRID:AB_10013483; dilution 1:1000), anti-chaoptin mouse
1155 monoclonal 24B10 (Fujita et al., 1982; DSHB: RRID:AB_528161, dilution 1:20) and anti-Brp
1156 mouse monoclonal nc82 (Wagh et al., 2006; DSHB:RRID:AB_2314866; dilution 1:30).
1157 Secondary antibodies were from Jackson ImmunoResearch Laboratories, Inc. Images were
1158 acquired on a Zeiss LSM 880 or confocal microscope using a 40x 1.3 NA objective.
1159
1160 Image processing
1161 Most anatomy figures show reconstructed views of cells of interest generated from
1162 confocal stack using FluoRender (http://www.sci.utah.edu/software/fluorender.html). Some

1163 images were manually edited to only show the cell relevant for the comparison to the EM
1164 reconstructions. Some panels in Figure 5 are overlays of registered images with either the
1165 template brain used for registration (Bogovic et al. 2019) or the pattern of a second registered
1166 expression pattern (L2 lamina neurons terminal in Figure 5Cv). Images with rhodopsin reporter
1167 (Rh3-, Rh5 or Rh6-LexA) labeling show single sections or maximum intensity projections
1168 through a small number of adjacent slices. For these images, other processing was limited to
1169 adjustments of brightness and contrast across the entire field of view for each channel.

Acknowledgements

The authors thank: Lou Scheffer, Shinya Takemura, and Kazunori Shinomiya for access to data, advice and discussions; Ruchi Parekh for managing the CAT team and coordinating the tracing effort; the FAFB tracing community for supportive and open sharing of methods and data; Janelia Fly Core for fly care and Janelia FlyLight Project Team for help with preparation and imaging of light microscopy samples; and the Janelia Visitor program for facilitating early stages of this collaboration. This work was supported by the Deutsche Forschungsgemeinschaft (DFG) through grants WE 5761/2-1 (M.F.W.) and SPP2205 (M.F.W.), AFOSR grant FA9550-19-1-7005 (M.F.W), with support from the Fachbereich Biologie, Chemie & Pharmazie of the Freie Universität Berlin (M.F.W.) and by the Howard Hughes Medical Institute through its support of the Janelia Research Campus (D.D.B, M.B.R. and G.M.R.).

Author Contributions

Emil Kind: Conceptualization, Methodology - neuronal reconstructions, Methodology – analysis, Software, Validation, Formal Analysis, Investigation – light microscopy, Investigation – neuronal reconstructions, Data Curation, Writing – original draft preparation, Writing – review and editing, Visualization.

Kit D. Longden: Methodology – analysis, Validation, Formal Analysis, Writing – original draft preparation, Writing – review and editing, Visualization.

Aljoscha Nern: Conceptualization, Methodology - neuronal reconstructions, Methodology – analysis, Validation, Formal Analysis, Investigation – light microscopy, Resources, Writing – original draft preparation, Writing – review and editing, Visualization.

Arthur Zhao: Methodology - neuronal reconstructions, Methodology – analysis, Software, Validation, Formal Analysis, Data Curation, Writing – original draft preparation, Writing – review and editing, Visualization.

Gizem Sancer: Methodology - neuronal reconstructions, Investigation – light microscopy, Investigation – neuronal reconstructions.

Miriam Flynn: Methodology - neuronal reconstructions, Investigation – neuronal reconstructions.

Connor Laughland: Methodology - neuronal reconstructions, Investigation – neuronal reconstructions.

Bruck Gezahegn: Methodology - neuronal reconstructions, Investigation – neuronal reconstructions.

Henrique Ludwig: Methodology - neuronal reconstructions, Investigation – neuronal reconstructions.

Alex Thomson: Methodology - neuronal reconstructions, Investigation – neuronal reconstructions.

Tessa Obrusnik: Methodology - neuronal reconstructions, Investigation – neuronal reconstructions.

Paula G. Alarcón: Methodology - neuronal reconstructions, Investigation – light microscopy, Investigation – neuronal reconstructions.

Heather Dionne: Investigation – molecular constructs, Resources.

Davi D. Bock: Methodology - neuronal reconstructions, Resources, Data Curation, Funding Acquisition.

Gerald M. Rubin: Resources, Writing – review and editing, Supervision, Funding Acquisition.

Michael B. Reiser: Conceptualization, Methodology - neuronal reconstructions, Methodology – analysis, Resources, Data Curation, Writing – original draft preparation, Writing – review and editing, Visualization, Supervision, Project Administration, Funding Acquisition.

Mathias F. Wernet: Conceptualization, Methodology - neuronal reconstructions, Methodology – analysis, Resources, Writing – original draft preparation, Writing – review and editing, Visualization, Supervision, Project Administration, Funding Acquisition.

1238 **Tables**

1239 Table 1: Synaptic targets of seed column R7 and R8

1240 Table 2: Cells that synapse onto seed column R7 and R8

1241 Table 3: Synaptic targets of seed column R7-DRA and R8-DRA

1242 Table 4: Cells that synapse onto seed column R7-DRA and R8-DRA

1243

1244 **Supplementary Files**

1245 Supplementary File 1:

1246 Tables of all seed column R7, R8, R7-DRA and R8-DRA target cells by type

1247 Supplementary File 2:

1248 Gallery plots of all seed column R7, R8, R7-DRA and R8-DRA target cells by type

1249 Supplementary File 3

1250 Tables of seed column synapses outside the medulla

1251 Supplementary File 4

1252 Fly genotypes organized by Figure panel

Figure 1

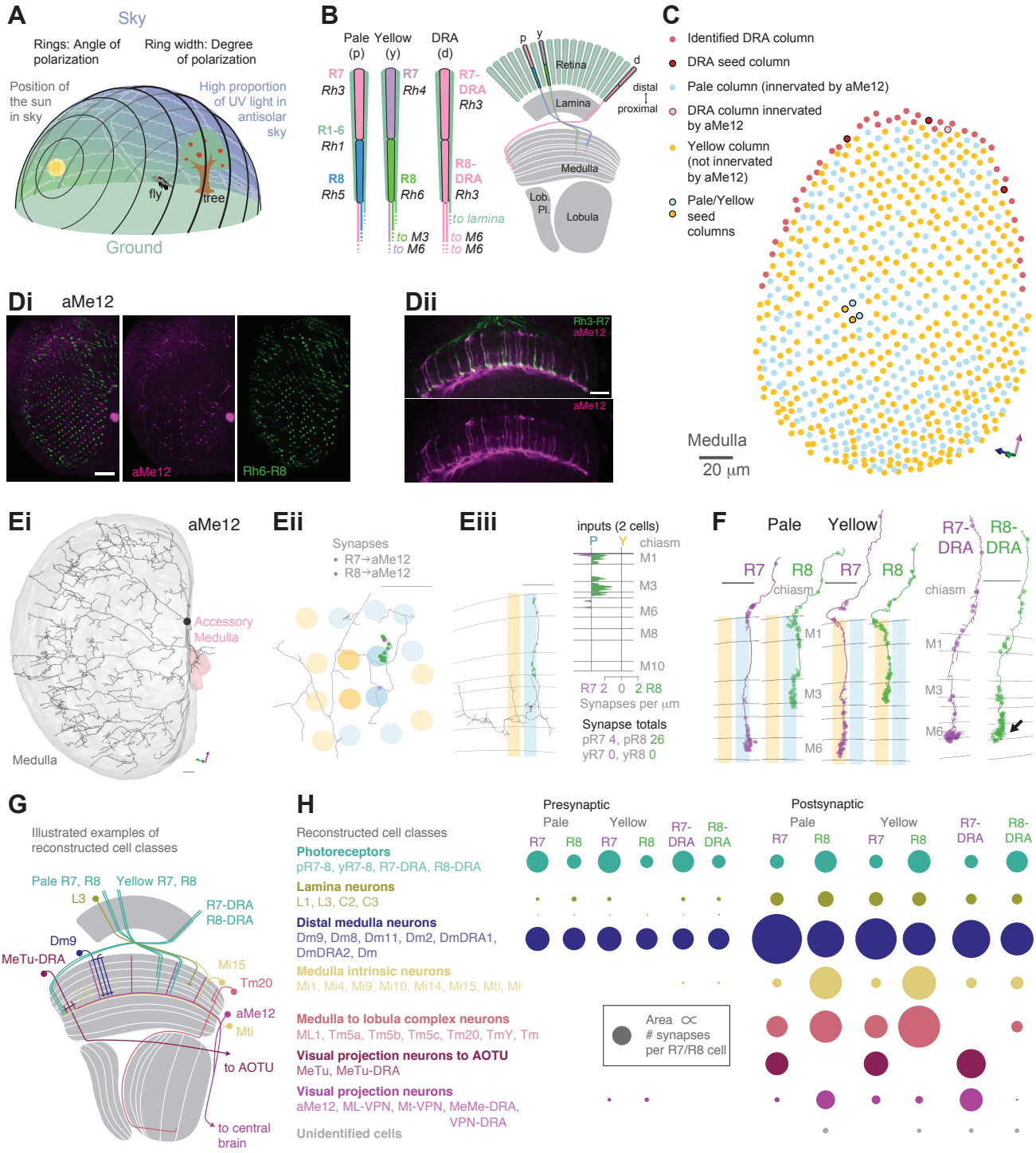
A
Sky
Rings: Angle of polarization
Ring width: Degree of polarization
Position of the sun in sky
High proportion of UV light in antisolar sky
fly
tree
Ground
B
Pale (p)
Yellow (y)
DRA (d)
R7 Rh3
R1-6 Rh1
R8 Rh5
R7 Rh4
R8 Rh6
R7-DRA Rh3
R8-DRA Rh3
to lamina
to M3
to M6
to M6
to M6
Retina
Lamina
Medulla
Lob. Pl.
Lobula
distal
proximal
C
Identified DRA column
DRA seed column
Pale column (innervated by aMe12)
DRA column innervated by aMe12
Yellow column (not innervated by aMe12)
Pale/Yellow seed columns
Medulla
20 μm
Di
aMe12
aMe12
Rh6-R8
Dii
Rh3-R7
aMe12
aMe12
Ei
aMe12
Accessory Medulla
Medulla
Eii
Synapses
R7→aMe12
R8→aMe12
Eiii
inputs (2 cells)
P
Y
chiasm
M1
M3
M6
M8
M10
R7 2 0 2 R8
Synapses per μm
Synapse totals
pR7 4, pR8 26
yR7 0, yR8 0
F
Pale
Yellow
R7
R8
R7
R8
R7-DRA
R8-DRA
chiasm
M1
M3
M6
G
Illustrated examples of reconstructed cell classes
Pale R7, R8
Yellow R7, R8
L3
R7-DRA
R8-DRA
Dm9
MeTu-DRA
Mi15
Tm20
aMe12
Mti
to AOTU
to central brain
H
Reconstructed cell classes
Photoreceptors
pR7-8, yR7-8, R7-DRA, R8-DRA
Lamina neurons
L1, L3, C2, C3
Distal medulla neurons
Dm9, Dm8, Dm11, Dm2, DmDRA1, DmDRA2, Dm
Medulla intrinsic neurons
Mi1, Mi4, Mi9, Mi10, Mi14, Mi15, Mti, Mi
Medulla to lobula complex neurons
ML1, Tm5a, Tm5b, Tm5c, Tm20, TmY, Tm
Visual projection neurons to AOTU
MeTu, MeTu-DRA
Visual projection neurons
aMe12, ML-VPN, Mt-VPN, MeMe-DRA, VPN-DRA
Unidentified cells
Presynaptic
Pale
Yellow
R7
R8
R7
R8
R7-DRA
R8-DRA
Postsynaptic
Pale
Yellow
R7
R8
R7
R8
R7-DRA
R8-DRA
Area ∝ # synapses per R7/R8 cell

1253 Figure 1: Systematic reconstruction of all synaptic targets of inner photoreceptor subtypes

1254 **A.** Simplified schematic summarizing some of the most salient visual stimuli of a fly (center):
1255 celestial cues (sun), color gradients (distribution of green versus UV wavelengths) and skylight
1256 polarization (as defined by degree of polarization and angle of polarization) can be used for
1257 navigation, as well as more or less colorful landmarks (tree). **B.** Schematic representation of
1258 the fly visual system. Left: In the retina, inner photoreceptor R7 (distal) and R8 (proximal)
1259 rhodopsin expression differs across three functionally specialized subtypes pale (p), yellow
1260 (y), and DRA (d). Rh3 and Rh4 opsins are both UV-sensitive, whereas Rh5 and Rh6 are more
1261 sensitive to blue and green wavelengths, respectively. R1-6 express Rh1 and are broadly
1262 sensitive to green and UV wavelengths. Only in the DRA, both R7 and R8 axons terminate in
1263 the same layer of the medulla neuropil (M6), which is the target layer of R7 cells outside the
1264 DRA, and non-DRA R8 cells terminate in layer M3. Right: Overview of the main four optic lobe
1265 neuropils. Only the lamina and medulla receive direct photoreceptor input. **C.** Distribution of
1266 medulla columns downstream of either p (light blue), y (yellow), and DRA (red) photoreceptors
1267 reconstructed from the FAFB data set. Pale columns were assigned via presence of aMe12
1268 long vertical projections (see below). Seven seed columns used for systematic reconstruction
1269 are highlighted with black circles. The colored axes indicate the orientation of the displayed
1270 view: green for lateral, magenta for dorsal, and blue for posterior axes. Scale bar: 20 μm. **D.**
1271 Double labeling of aMe12 vertical processes and yellow R8 cells. See Materials and Methods
1272 and Supplementary File 4 for fly genotypes and other details of this and other light microscopy
1273 panels. Left (Di): Confocal image showing the array of medulla columns with labeling of aMe12
1274 neurons (purple) and yellow R8 axons (green). Note that the two patterns appear near-
1275 mutually exclusive. Right (Dii): Side view of aMe12 vertical projections and pale R7 axons
1276 (green). Di-ii Scale bars: 20 μm. **E.** Left (Ei): Skeleton of the optic lobe part of a fully
1277 reconstructed aMe12 neuron (gray), with processes leaving the medulla through the
1278 accessory medulla (pink). Eii: Across the four central seed columns (darker shading), synaptic
1279 input from R7 (purple dots) and R8 photoreceptors (green dots) to aMe12 is specific to the

1280 designated pale columns. Eiii, Left: Sideview depicting the distribution of R7 and R8 inputs
1281 into aMe12 across medulla layers (color code of pale and yellow columns as before). Right:
1282 Same distribution plotted as synapses/µm, for both pale and yellow columns (color code as
1283 before). Ei-iii: Scale bars: 10 μm. **F.** Reconstructed pale R7 and R8, yellow R7 and R8, and
1284 R7-DRA and R8-DRA terminals with R7 presynapses in purple and R8 presynapses in green.
1285 Note the termination of R8-DRA in the R7 target layer M6 (arrow). Scale bars: 10 μm. **G.**
1286 Illustrations of reconstructed neuron classes, including lamina monopolar (L), distal medulla
1287 (Dm), medulla intrinsic (Mi), transmedulla (Tm), medulla tangential intrinsic (Mti), visual
1288 projection neurons targeting the central brain (example: aMe12), and medulla-to-tubercle
1289 (MeTu) cells projecting to the anterior optic tubercle (AOTU). **H.** For the synapses from seed
1290 column inner photoreceptors to cells with ≥ 3 synapses, we identified the cell type or cell class
1291 of 99.5% (3803/3821 synapses). Overview of the relative strength of these connections with
1292 different neuron classes (color code as before), including with the unidentified cells (Tables 1-
1293 4), across pale, yellow, and DRA columns (pre- and postsynaptic). Area of circles corresponds
1294 to the number of synapses per R7 and R8 cell.
1295

Figure 1 – figure supplement 1

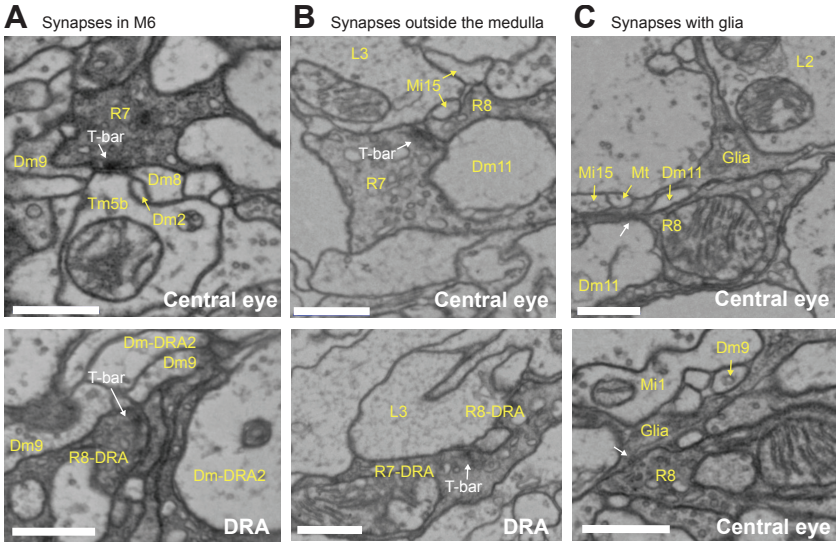

1296 Figure 1 - figure supplement 1: Example EM-images

1297 **A**. Example EM-images of photoreceptor synapses in medulla layer 6. Top: R7 synapse (T-
1298 bar labelled) with postsynaptic Dm2, Dm8, Dm9 and Tm5b cells. Bottom: R8-DRA synapse,
1299 with postsynaptic Dm9 and Dm-DRA2 cells. R8 synapses in layer 6 were diagnostic of DRA
1300 columns (see Materials and Methods). **B**. Images of synapses outside the medulla in the
1301 central (top) and DRA (bottom) seed columns. **C**. Two examples of photoreceptor synapses
1302 with glia, with the arrows indicating the postsynaptic density in the glial cell. Scale bars: 500
1303 μm.

1304

Figure 1 – figure supplement 2

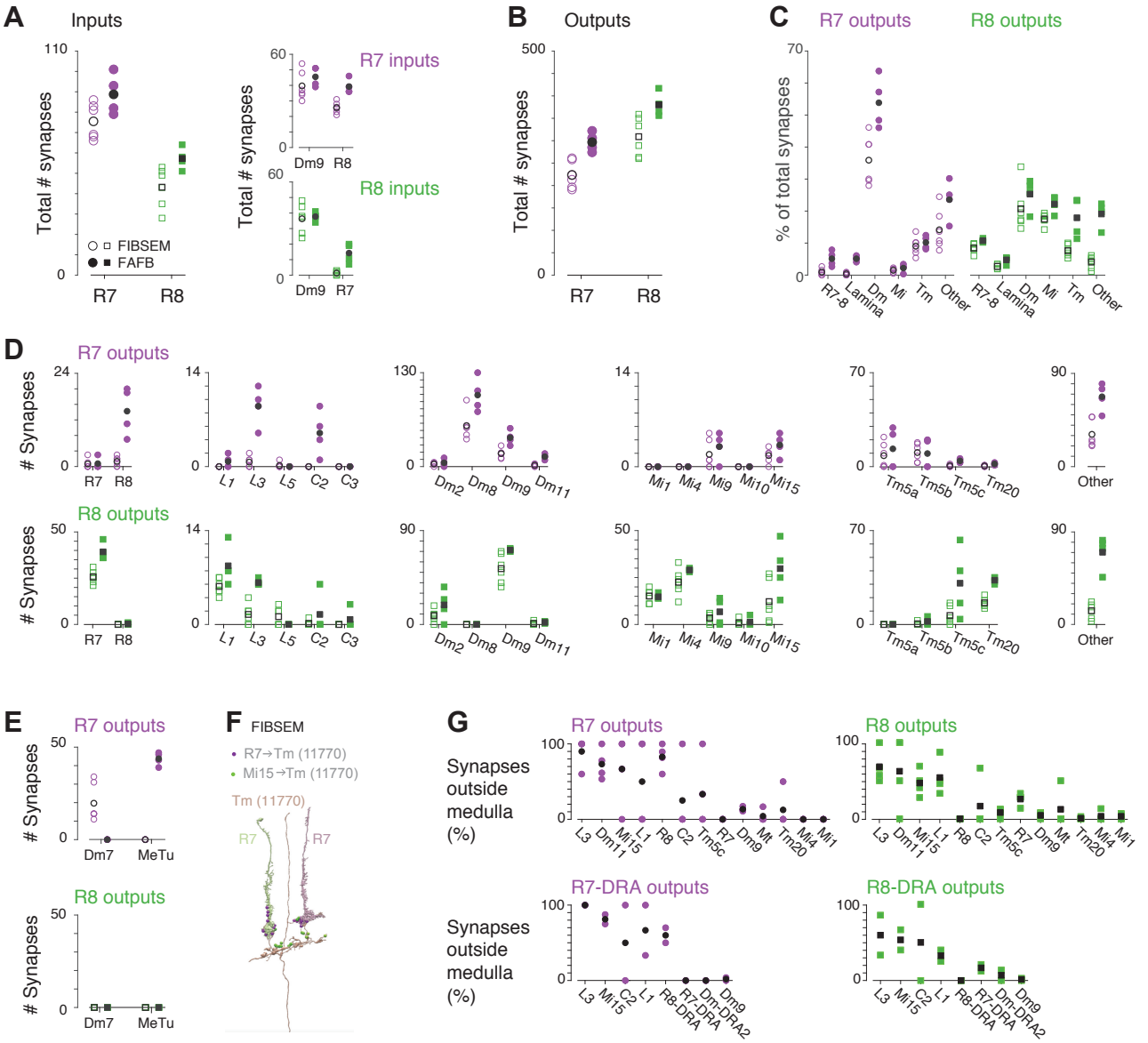

1305 Figure 1 – figure supplement 2: Comparison with medulla FIB-SEM data

1306 **A**. Left: Comparison of total numbers of synaptic inputs to R7 (purple, circles) and R8 (green,
1307 squares) in our data set (filled symbols) and a medulla FIB-SEM data set (open symbols), with
1308 mean values are indicated by black symbols. These plotting conventions are used throughout
1309 the figure. We used the six columns identified as pale and yellow in the FIB-SEM data set
1310 (Takemura et al. 2015) by Menon et al. (2019), made available in Clements et al. (2020), see
1311 Materials and Methods. Right: The R7-8 photoreceptors and Dm9 inputs dominate the
1312 synaptic input to R7 (purple, circles) and to R8 (green, squares); the increased number of
1313 synapses outside medulla (see panel G) likely accounts for the higher number of inputs to our
1314 R7-8 cells. **B**. Comparison of the total number of output synapses from R7 and R8. We
1315 reconstructed more output synapses, per cell, than in the FIB-SEM data set. **C**. Comparison
1316 of total numbers of R7-8 output synapses disaggregated by cell classes. To enable like-for-
1317 like comparisons, we used only cell classes and cell types annotated in both data sets, with
1318 the cell types shown in D. To quantify the completeness of cell type identification, we counted
1319 all other identified cell types found each data set in the 'Other' category. Our reconstruction
1320 found a large increase in R7 synapses to multicolumnar Dm cells, and increases in R8
1321 synapses to multicolumnar cell classes, such as Tm cells and cells like aMe12 in the 'Other'
1322 class. **D**. Comparison of total numbers of R7 (top) and R8 (bottom) output synapses
1323 disaggregated by cell type, with cell types grouped from left to right by their cell class
1324 categories in C. For R7, there were increases in synapses to R8 and L3, which receive
1325 synapses outside the medulla, and Dm8 cells, which are multicolumnar. For R8, there were
1326 increases in synapses to R7 and Mi15, which receive synapses outside the medulla, and
1327 multicolumnar Tm5c and 'Other' cell types, and also Tm20 cells, which may be surprising
1328 because this cell type is columnar. **E**. Comparison of R7-8 synapses to (FIB-SEM) Dm7 and
1329 (current study) MeTu cells. These two cell types were the only cell type discrepancies between
1330 the data sets: Dm7 cells were major targets of R7 in the FIB-SEM data, but not in ours, while
1331 MeTu cells were major targets in our data but not in the FIB-SEM data. **F**. Example Tm cell
1332 (brown, Tm #11770) in the FIB-SEM data whose dendritic morphology matched MeTu cell.

1333 Two R7 cells (green, left, and purple, right), are also shown, along with R7 synapses (green
1334 circles) and Mi15 synapses (purple). We propose that some MeTu cells are included in the
1335 FIB-SEM data but are currently annotated as unidentified Tm or Dm7 cells. **G**. Percentages
1336 of synapses outside the medulla for R7 (left) and R8 (right) with cell types in the central (top)
1337 and DRA (bottom) seed columns. L3 in particular is almost exclusively innervated outside the
1338 medulla. Tables of synapses outside the medulla are listed for each cell type in Supplementary
1339 File 3.

Figure 2

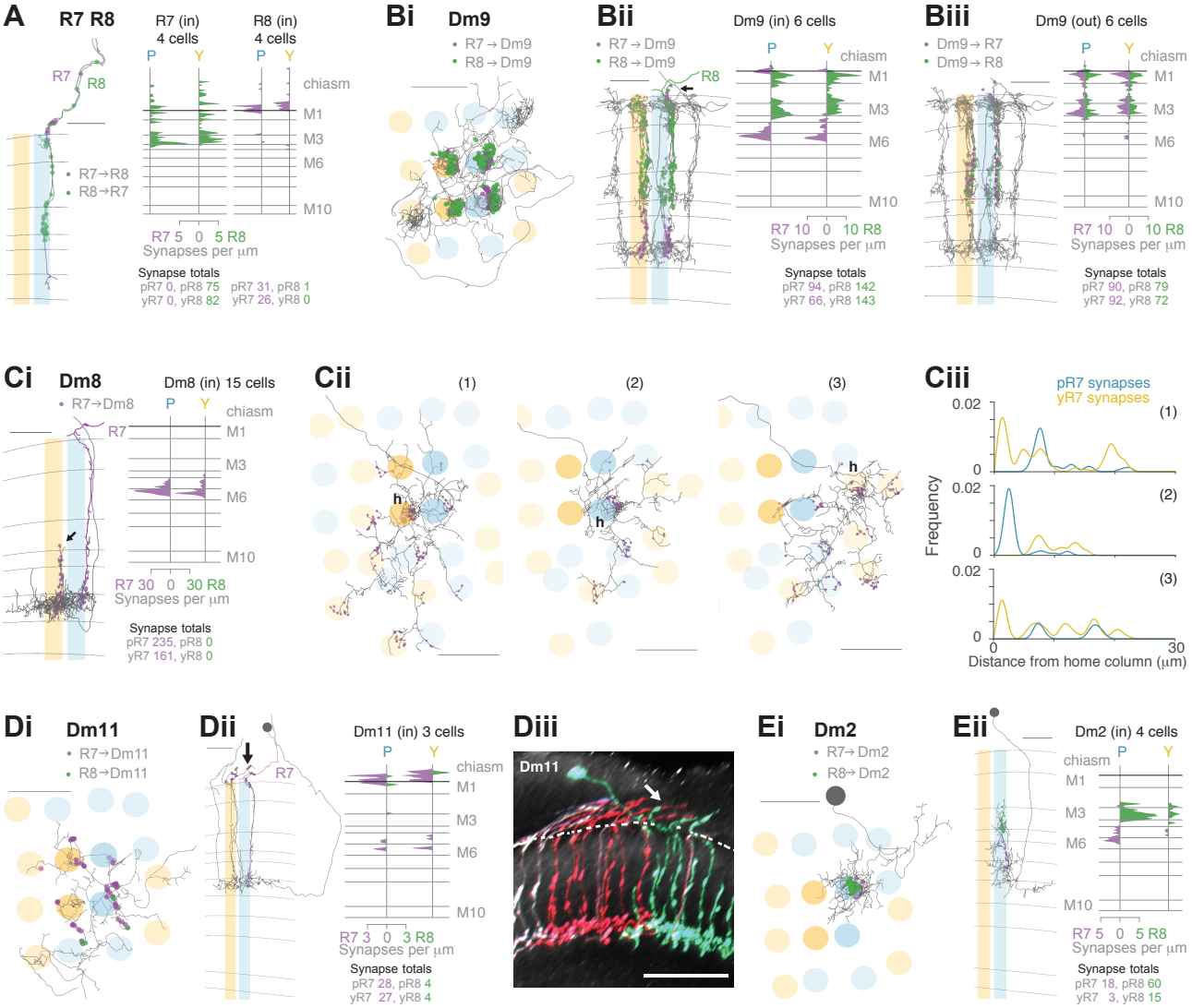
A
R7 R8
R7 (in) 4 cells
R8 (in) 4 cells
P Y
chiasm
M1
M3
M6
M10
R7→R8
R8→R7
R7 5 0 5 R8
Synapses per µm
Synapse totals
pR7 0, pR8 75
yR7 0, yR8 82
pR7 31, pR8 1
yR7 26, yR8 0
Bi
Dm9
R7→Dm9
R8→Dm9
Bii
Dm9 (in) 6 cells
R7 10 0 10 R8
Synapses per µm
Synapse totals
pR7 94, pR8 142
yR7 66, yR8 143
Biii
Dm9 (out) 6 cells
Dm9→R7
Dm9→R8
R7 10 0 10 R8
Synapses per µm
Synapse totals
pR7 90, pR8 79
yR7 92, yR8 72
Ci
Dm8
R7→Dm8
Dm8 (in) 15 cells
R7 30 0 30 R8
Synapses per µm
Synapse totals
pR7 235, pR8 0
yR7 161, yR8 0
Cii
(1)
(2)
(3)
h
Ciii
pR7 synapses
yR7 synapses
Frequency
0.02
0
30
Distance from home column (µm)
Di
Dm11
R7→Dm11
R8→Dm11
Dii
Dm11 (in) 3 cells
R7 3 0 3 R8
Synapses per µm
Synapse totals
pR7 28, pR8 4
yR7 27, yR8 4
Diii
Dm11
Ei
Dm2
R7→Dm2
R8→Dm2
Eii
Dm2 (in) 4 cells
R7 5 0 5 R8
Synapses per µm
Synapse totals
pR7 18, pR8 60
yR7 3, yR8 15

1340 Figure 2: Synapses between R7 and R8, and with Dm neurons in the central medulla

1341 **A.** Synapses between central R7 and R8 cells. Left: Side view of R7 (purple) and R8 (green),
1342 with R7→R8 synapses (purple points) and R8→R7 synapses (green points). Note synapses
1343 outside the medulla neuropil (distal to layer M1). Scale bar: 10 μm. Right: Synapse distribution
1344 (in synapses/μm) in the yellow and pale seed columns. **B.** Synapses between R7 and R8 and
1345 Dm9 cells. Bi: Top view of a fully reconstructed Dm9 skeleton (grey) covering all four central
1346 seed columns (darker shading) with all R7 (purple) and R8 (green) inputs. Bii, Left: Side view
1347 of R7 (purple) and R8 synapses (green) to the same Dm9 cell across medulla layers. Right:
1348 Layer distribution of photoreceptor inputs to six Dm9 cells. Biii, Left: Side view of Dm9→ R7
1349 (purple) and Dm9→R8 (green) feedback synapses from the same Dm9 cell. Right: Layer
1350 distribution of feedback synapses from six Dm9 occupying the seed columns. Most of these
1351 synapses are from the illustrated Dm9 cell with other Dm9 cells contributing a small number
1352 of connections in M1 and M6. **C.** Synapses between R7 and Dm8 cells. Ci, Left: Side view of
1353 R7 synapses (purple) to a fully reconstructed Dm8 cell, with one pale R7 cell is shown in
1354 purple. Note the characteristic vertical projections of Dm8 in its 'home column' (arrow; yellow
1355 R7 cell not shown). Right: Layer distribution of R7 inputs from 14 Dm8 cells innervating the
1356 four seed columns. Cii: Full reconstructions of three Dm8 cells (labeled 1,2,3) innervating the
1357 four seed columns, with all R7 synapses (purple), including inputs beyond the seed columns.
1358 Individual Dm8 home columns (h) are marked. Ci-ii Scale bars: 10 μm. Ciii: R7→Dm8
1359 synapses/μm as a function of their distance from the home column, for the three Dm8 cells
1360 (1,2,3 above). The cells receive dense innervation in their home column and weaker inputs
1361 from both pale and yellow R7 cells in their periphery. **D.** Synapses between R7 and Dm11
1362 cells with R7 (purple) and R8 (green) synapses from seed columns. Di: Top view of a
1363 reconstructed Dm11 skeleton. Dii, Left: Side view of the layer distribution of photoreceptor
1364 synapses, including synapses outside the medulla (arrow). Di-ii Scale bars: 10 μm. Right:
1365 Layer distribution of R7 and R8 inputs to three Dm11 cells. Diii: Rendering of a confocal image
1366 of MultiColor FlpOut (MCFO) labelled Dm11 cells. Note the characteristic vertical projections

1367 leaving the medulla neuropil (arrow). The dashed line marks the approximate boundary of the
1368 medulla neuropil. Scale bar: 20 μm. **E.** Synapses between R7 and R8 and Dm2 cells. Ei: Top
1369 view of a Dm2 skeleton, with R7 (purple) and R8 (green) synapses. Eii, Left: Side view of layer
1370 distribution of photoreceptor synapses onto the same Dm2 cell. Ei-ii Scale bars: 10 μm. Right:
1371 Layer distribution of R7 and R8 inputs to four Dm2 cells.
1372

Figure 2 – figure supplement 1

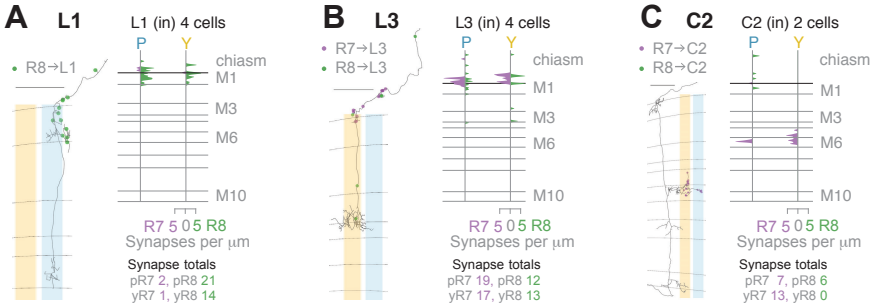

1373 Figure 2 – figure supplement 1: Lamina cell types targeted by central column R7-8

1374 **A**. Left: Side view of a reconstructed L1 cell (gray) with R8→L1 synapses (green). Right:
1375 Layer distribution (in synapses/μm) of all R7 and R8 inputs to 4 L1 cells. B**.** Left: Side view of
1376 a reconstructed L3 cell (gray), with R7→L3 (purple) and R8→L3 synapses (green). Right:
1377 Layer distribution (in synapses/μm) of all R7 and R8 inputs to 4 L3 cells. **C.** Left: Side view of
1378 a reconstructed C2 cell (gray), with R7→C2 (purple) and R8→C2 synapses (green). Right:
1379 Layer distribution (in synapses/μm) of all R7 and R8 inputs to 2 C2 cells. **A-C.** All scale bars:
1380 10 μm.

Figure 3

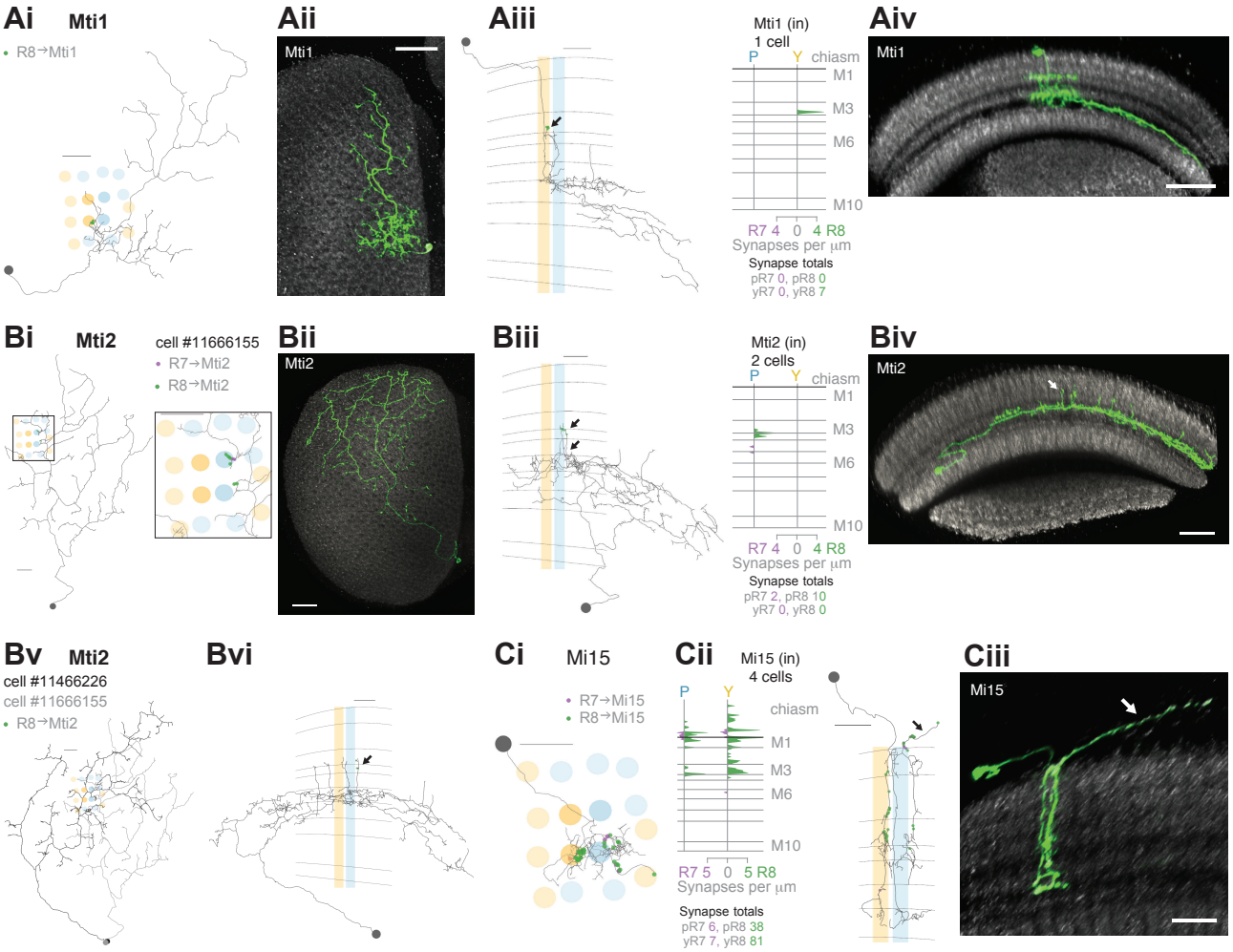
Ai
Mti1
R8→Mti1
Aii
Mti1
Aiii
Mti1 (in)
1 cell
P
Y
chiasm
M1
M3
M6
M10
R7 4 0 4 R8
Synapses per µm
Synapse totals
pR7 0, pR8 0
yR7 0, yR8 7
Aiv
Mti1
Bi
Mti2
cell #11666155
R7→Mti2
R8→Mti2
Bii
Mti2
Biii
Mti2 (in)
2 cells
P
Y
chiasm
M1
M3
M6
M10
R7 4 0 4 R8
Synapses per µm
Synapse totals
pR7 2, pR8 10
yR7 0, yR8 0
Biv
Mti2
Bv
Mti2
cell #11466226
cell #11666155
R8→Mti2
Bvi
Ci
Mi15
R7→Mi15
R8→Mi15
Cii
Mi15 (in)
4 cells
P
Y
chiasm
M1
M3
M6
M10
R7 5 0 5 R8
Synapses per µm
Synapse totals
pR7 6, pR8 38
yR7 7, yR8 81
Ciii
Mi15

1381 Figure 3: R7-8 synapses with medulla intrinsic (Mi) and medulla tangential intrinsic (Mti) cell
1382 types
1383 **A.** Synapses of central R7 and R8 with Mti1 cells. Ai: Top view of an Mti1 skeleton with
1384 synapses from seed column R8 cells (green). Scale bar: 10 μm. Aii: Top view of an MCFO-
1385 labeled cell matching overall Mti1 morphology. Light microscopy images (Aii,Aiv,Bii,Biv,Ciii)
1386 were manually segmented to focus on the cells of interest. Scale bar: 20 μm. Aiii: Side view
1387 of the same Mti1 cell as in Ai with R8 (green) synapses. Scale bar: 10 μm. Aiv: Side view
1388 rendering of the same light microscopy Mti1 image (green). Scale bar: 20 μm. **B.** Synapses
1389 from R7 and R8 to Mti2. Bi: Top view of a reconstructed Mti2 cell, with R7 (purple) and R8
1390 (green) synapses. Scale bar: 10 μm. Bii: Top view of an MCFO-labeled cell matching overall
1391 Mti2 morphology. Scale bar: 20 μm. Biii: Side view of the same Mti2 skeleton as in Bi with R7
1392 (purple) and R8 (green) synapses on characteristic vertical projections (arrow). Scale bar: 10
1393 μm. Biv: Side view of the cell shown in Bii. Arrow indicates vertical projections. Scale bar: 20
1394 μm. Bv: Top view of a second reconstructed Mti2 cell (dark gray) overlayed on the first (light
1395 gray), with R8 (green) synapses. Bvi: Side view of the second Mti2 skeleton, with R8 (green)
1396 synapses again located on vertical projections (arrow). Bv-vi Scale bars: 10 μm. **C.** Synapses
1397 of R7 and R8 with Mi15 cells. Ci: Top view of a fully reconstructed Mi15 skeleton, with R7
1398 (purple) and R8 (green) synapses. Cii, left: Side view depicting the layer distribution of
1399 photoreceptor synapses (same color code) onto the same Mi15 skeleton, with synapses
1400 outside the medulla (arrow). Ci-ii Scale bars: 10 μm. Right: Layer distribution of R7 and R8
1401 inputs to four Mi15 cells. Ciii: Side view rendering of a light microscopy image (MCFO) of an
1402 Mi15 cell. Note the long process leaving the medulla (arrow). Scale bar: 10 μm.
1403

Figure 3 – figure supplement 1

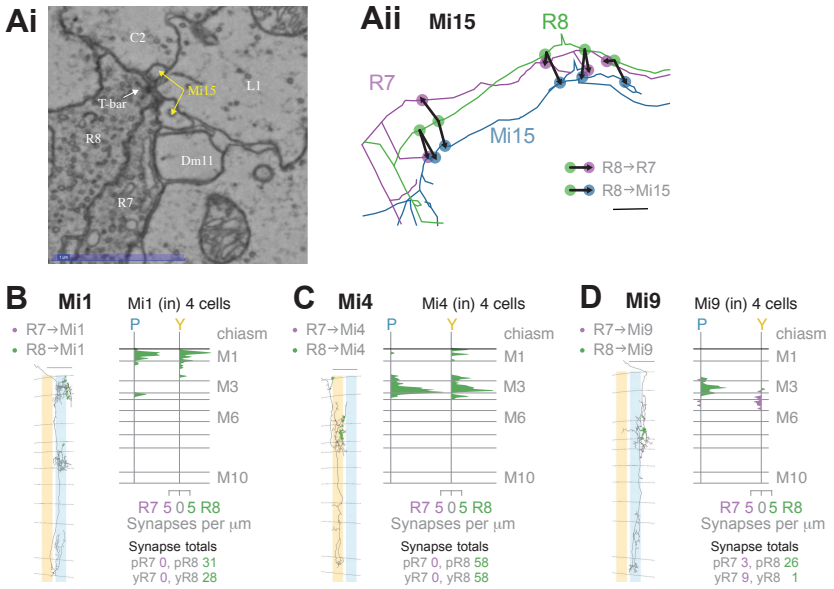

1404 Figure 3 – figure supplement 1: Mi cell types targeted by R7-8

1405 **A**. Colocalization of R8→Mi15 synapses with R8→R7 synapses. Ai. Example EM-image of
1406 Mi15 and R7 cells as postsynaptic partners of the same R8 presynapse. Scale bar: 1 μm. Aii.
1407 Magnified view of skeletons of R8, Mi15, and R7 cells in the optic chiasm, illustrating the
1408 colocalization of R8→Mi15 synapses with R8→R7 synapses at 5 successive locations. Scale
1409 bar: 1 μm. **B**. Left: Side view of a reconstructed Mi1 cell (gray) with R7→Mi1 (purple) and
1410 R8→Mi1 synapses (green). Right: Layer distribution (in synapses/μm) of all R7 and R8 inputs
1411 to 4 Mi1 cells. **C**. Left: Side view of a reconstructed Mi4 cell (gray) with R7→Mi4 (purple) and
1412 R8→Mi4 synapses (green). Right: Layer distribution (in synapses/μm) of all R7 and R8 inputs
1413 to 4 Mi4 cells. **D**. Left: Side view of a reconstructed Mi9 cell (gray) with R7→Mi9 (purple) and
1414 R8→Mi9 synapses (green). Right: Layer distribution (in synapses/μm) of all R7 and R8 inputs
1415 to 4 Mi9 cells. In the pale seed columns, Mi9 cells received many R8 synapses, but only
1416 received 1 R8 synapse in the yellow seed columns. **B-D.** Scale bars: 10 μm.

Figure 4

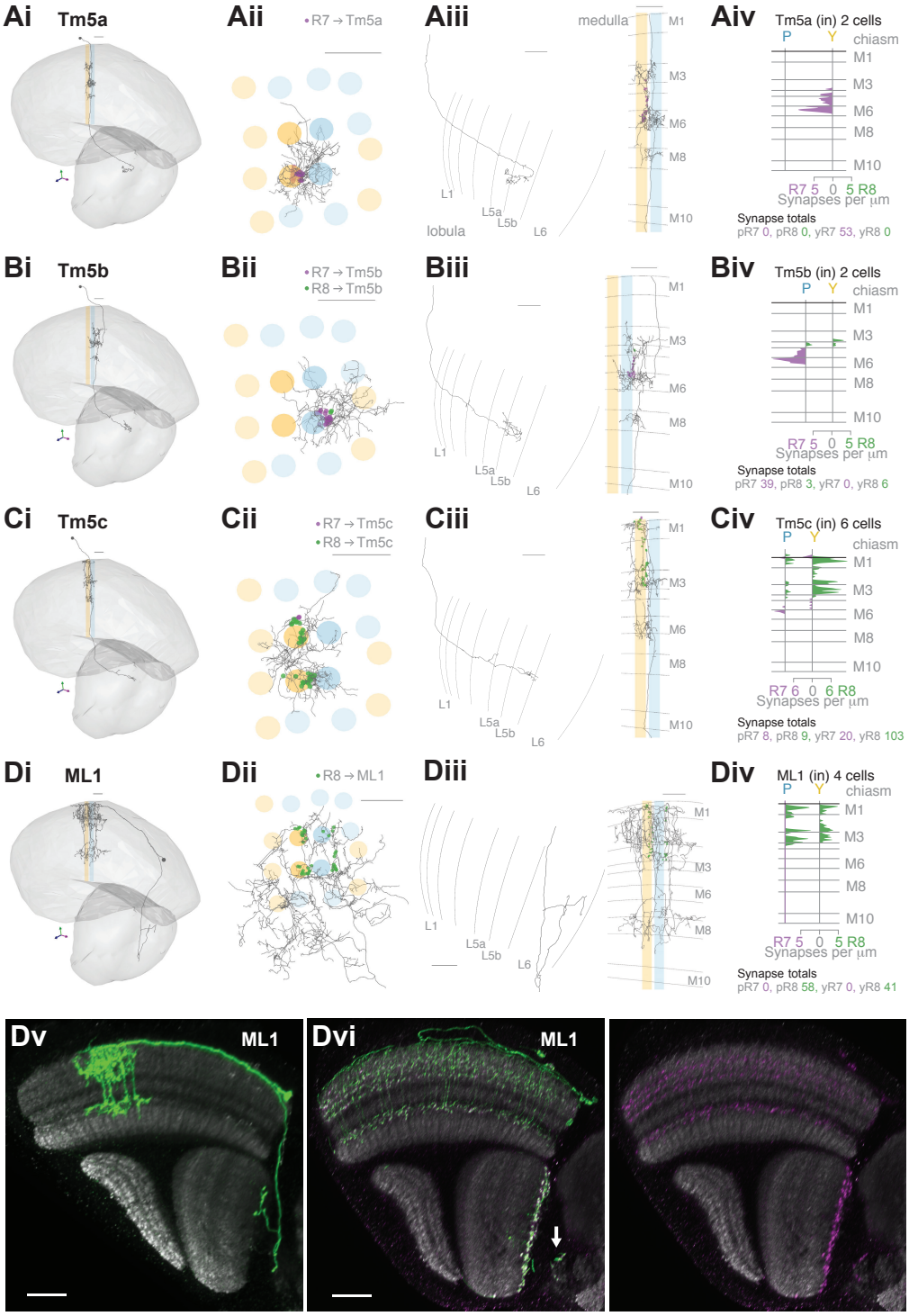
Ai
Tm5a
Aii
R7 → Tm5a
Aiii
medulla
M1
M3
M6
M8
M10
L1
L5a
L5b
L6
lobula
Aiv
Tm5a (in) 2 cells
P
Y
chiasm
R7 5 0 5 R8
Synapses per µm
Synapse totals
pR7 0, pR8 0, yR7 53, yR8 0
Bi
Tm5b
Bii
R7 → Tm5b
R8 → Tm5b
Biii
Biv
Tm5b (in) 2 cells
R7 5 0 5 R8
Synapses per µm
Synapse totals
pR7 39, pR8 3, yR7 0, yR8 6
Ci
Tm5c
Cii
R7 → Tm5c
R8 → Tm5c
Ciii
Civ
Tm5c (in) 6 cells
R7 6 0 6 R8
Synapses per µm
Synapse totals
pR7 8, pR8 9, yR7 20, yR8 103
Di
ML1
Dii
R8 → ML1
Diii
Div
ML1 (in) 4 cells
R7 5 0 5 R8
Synapses per µm
Synapse totals
pR7 0, pR8 58, yR7 0, yR8 41
Dv
ML1
Dvi
ML1

1417 Figure 4: R7-8 synapses with cell types projecting to the lobula

1418 **A-D**. Synapses between R7 and R8 and Tm5a (A), Tm5b (B), Tm5c (C) and ML1 (D) cell
1419 types. Panels **i-iii**: Anatomy of fully reconstructed cells. **i**: Side view. **ii**: Top view. **iii**, Left: Side
1420 view of axon terminals in the lobula. Right: Side view of medulla branches. R7 synapses are
1421 indicated in purple, R8 synapses in green in ii, iii (Right). **iv**: Layer distribution of R7 and R8
1422 inputs. Scale bars: 10 μm. **A.** Tm5a. The two Tm5a cells were exclusively targeted by yellow
1423 R7 cells. **B.** Tm5b. The two Tm5b cells were highly biased to pale R7 inputs. **C.** Tm5c. The
1424 five Tm5c cells were highly biased to yellow R8 inputs. **D.** ML1. Dv: Side view of a single
1425 MCFO-labeled ML1 cell (light microscopy). Note this cell has terminals both at the base of the
1426 deepest lobula layer and in the central brain; not all examined ML1 cells have terminals in the
1427 central brain. Scale bar: 20 μm. Dvi: Side view showing the distribution of a membrane marker
1428 (green) and presynaptic marker (synaptotagmin-HA, purple) in ML1 cells imaged as a
1429 population. The combined patterns (Left), and the presynaptic marker alone (Right) are
1430 shown. Arrow indicates central brain terminals. Scale bar: 20 μm.

1431

Figure 4 – figure supplement 1

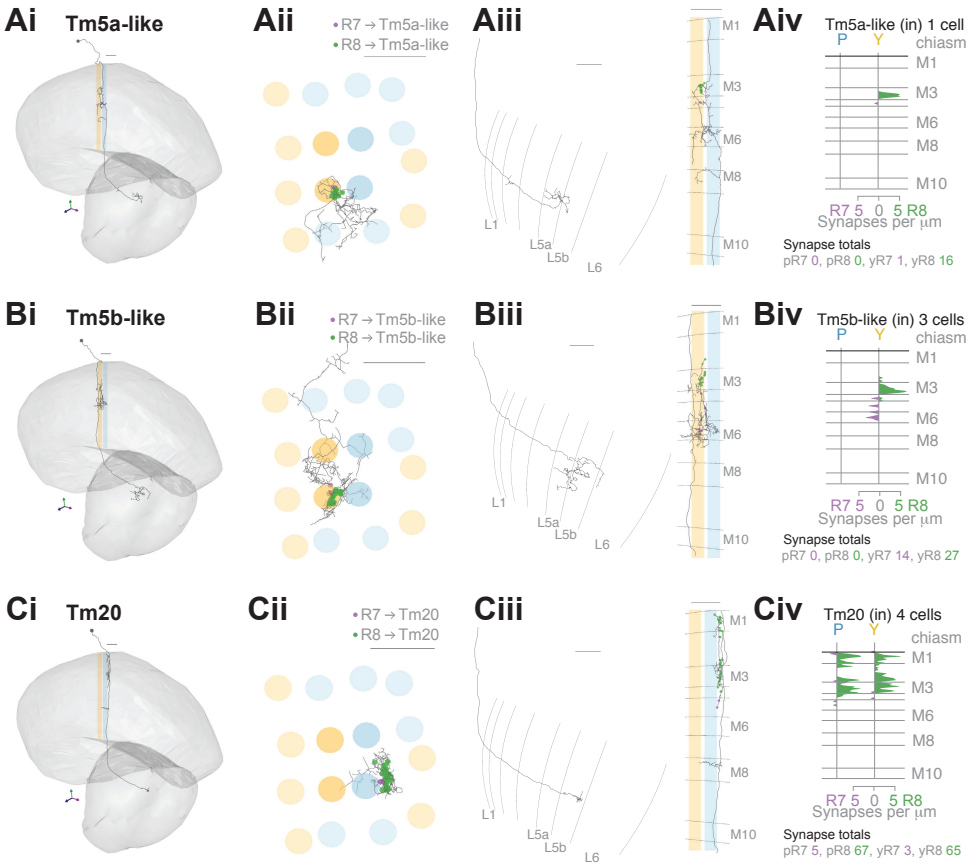

1432 Figure 4 – figure supplement 1: Additional connections of R7-8 to cell types projecting to the
1433 lobula

1434 **A.** R7 and R8 connections with the Tm5a-like cell, that has a morphology similar to a Tm5a
1435 cell, but a different pattern of connectivity. The same reconstructed cell is shown in Ai-iii. Ai:
1436 Side view. Aii: Top view with R7 (purple) and R8 (green) synapses. Aiii: Left: The axon
1437 terminals in the lobula. Right: Side view with R7 (purple) and R8 (green) synapses. Aiv: Layer
1438 distribution (in synapses/μm) of all R7 and R8 inputs from four seed columns to the Tm5a-like
1439 cell. **B.** R7 and R8 connections with three Tm5b-like cells, that each have a morphology similar
1440 to a Tm5b cell, but a different, shared pattern of connectivity. The same reconstructed Tm5b-
1441 like cell is shown in Bi-iii. Bi: Side view. Bii: Top view with R7 (purple) and R8 (green)
1442 synapses. Biii: Left: The axon terminals in the lobula. Right: Side view with R7 (purple) and
1443 R8 (green) synapses. Biv: Layer distribution (in synapses/μm) of all R7 and R8 inputs from
1444 four seed columns to the three Tm5b-like cells. Unlike the Tm5b cells, the Tm5b-like cells are
1445 predominantly targeted by yellow R8 photoreceptors. **C.** R7 and R8 connections with Tm20
1446 cells. The same reconstructed Tm20 cell is shown in Ci-iii. Ci: Side view. Cii: Top view with
1447 R7 (purple) and R8 (green) synapses. Ciii: Left: The axon terminals in the lobula. Right: Side
1448 view with R7 (purple) and R8 (green) synapses. Civ: Layer distribution (in synapses/μm) of all
1449 R7 and R8 inputs from four seed columns to the four Tm20 cells. **A-C.** Scale bars: 10 μm.

Figure 4 – figure supplement 2

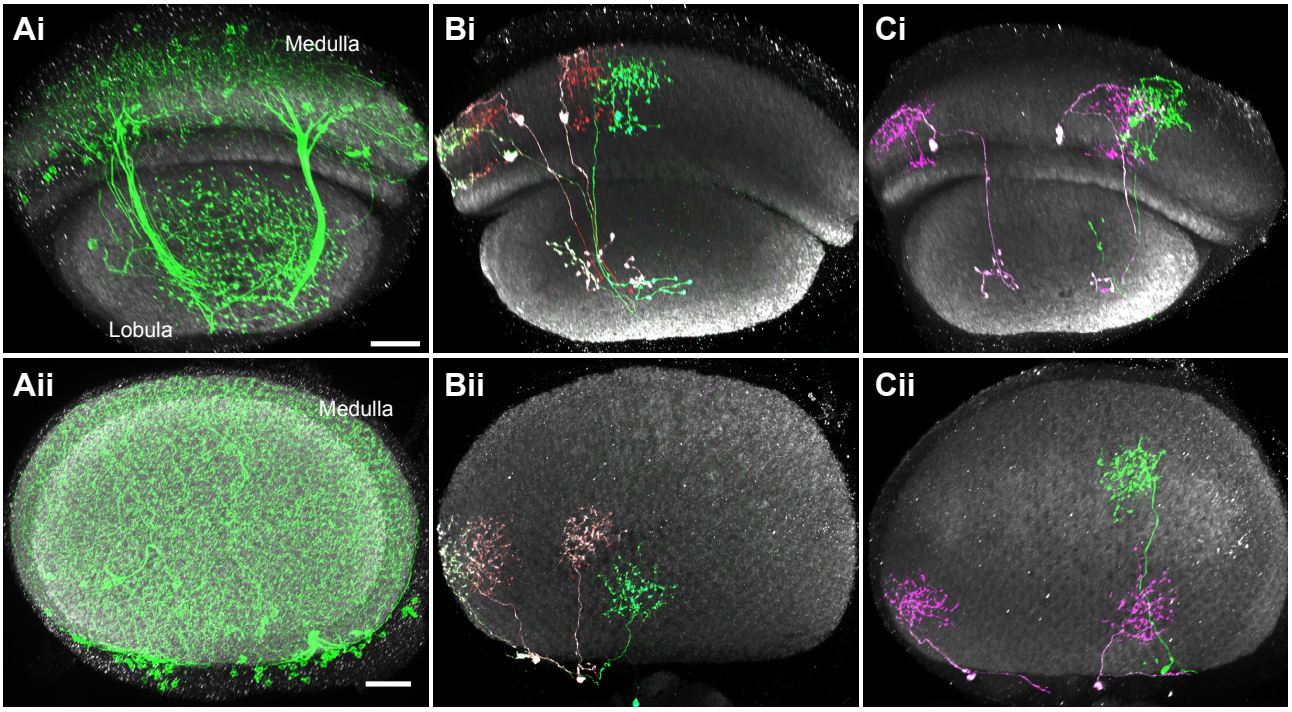

1450 Figure 4 – figure supplement 2: ML1 arbor distribution in the medulla and lobula

1451 Scale bars in (Ai,Aii) represent 20 μm. The other panels are shown at a similar scale. Images
1452 show views generated from image stacks (see Materials and Methods). Images show a top
1453 view of the array of column in the lobula (top panels, lower part of each image) or the medulla
1454 (lower panels), respectively. **A**. As a population, ML1 cells appear not to cover all visual
1455 columns in the lobula (Ai) but do cover the entire medulla (Aii). Note absence of the green
1456 ML1 membrane label near the dorsal and ventral margin of the lobula but not the medulla.
1457 **B,C**. Lobula (Bi,Ci) and medulla (Bii,Cii) arbors of two groups of MCFO-labeled ML1 cells. The
1458 retinotopic array of ML1 cells in the medulla (Bii,Cii) is only partly reflected in the positions of
1459 their axon terminals (Bi,Ci) in or near the lobula. For example, cells near the medulla edge
1460 have terminals away from the margin of the lobula.

Figure 5

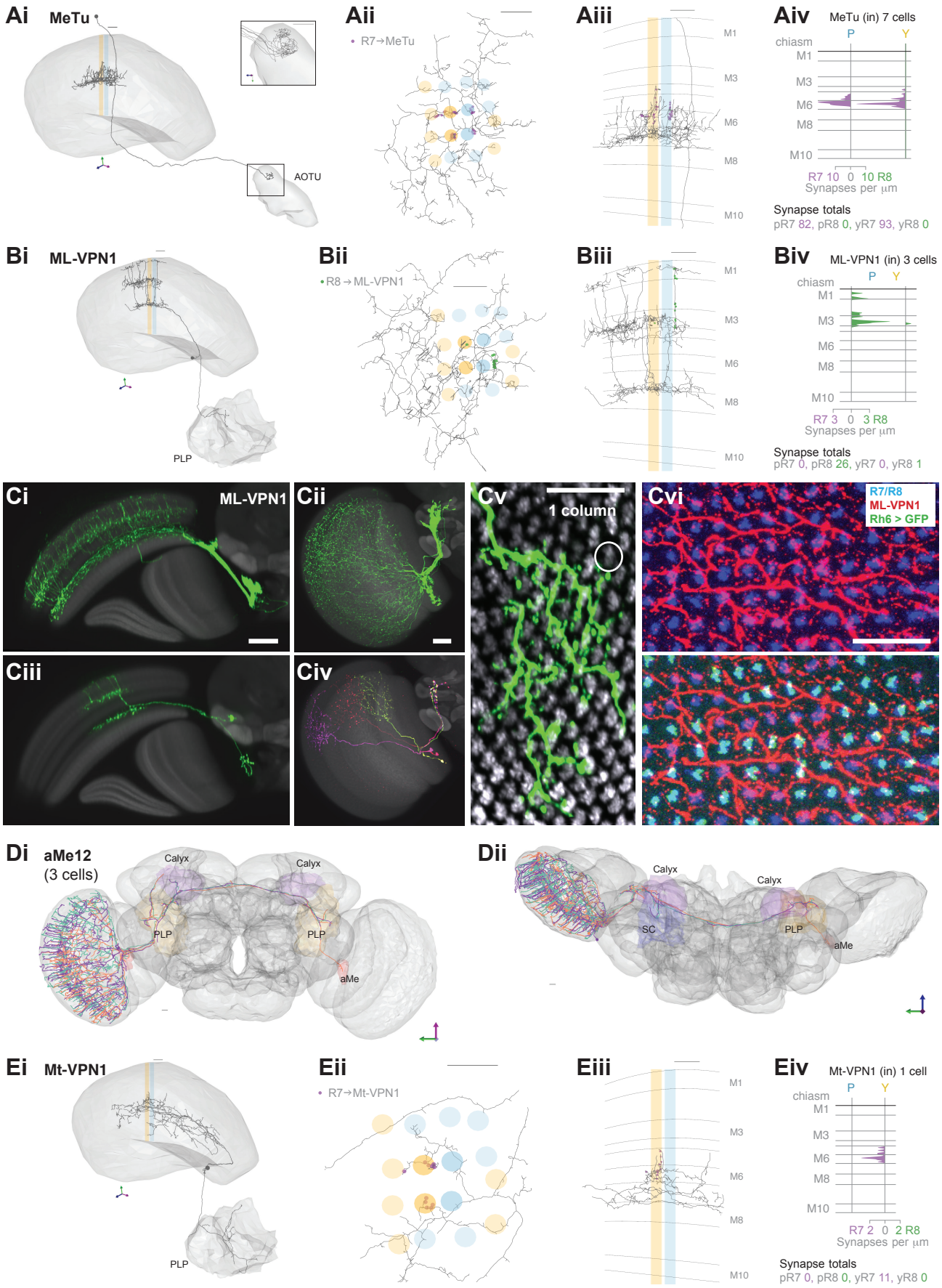
Ai
MeTu
AOTU
Aii
R7→MeTu
Aiii
M1
M3
M6
M8
M10
Aiv
MeTu (in) 7 cells
P
Y
chiasm
M1
M3
M6
M8
M10
R7 10 0 10 R8
Synapses per µm
Synapse totals
pR7 82, pR8 0, yR7 93, yR8 0
Bi
ML-VPN1
PLP
Bii
R8→ML-VPN1
Biii
M1
M3
M6
M8
M10
Biv
ML-VPN1 (in) 3 cells
P
Y
chiasm
M1
M3
M6
M8
M10
R7 3 0 3 R8
Synapses per µm
Synapse totals
pR7 0, pR8 26, yR7 0, yR8 1
Ci
ML-VPN1
Cii
Cv
1 column
Cvi
R7/R8
ML-VPN1
Rh6 > GFP
Ciii
Civ
Di
aMe12
(3 cells)
Calyx
Calyx
PLP
PLP
aMe
Dii
Calyx
Calyx
SC
PLP
aMe
Ei
Mt-VPN1
PLP
Eii
R7→Mt-VPN1
Eiii
M1
M3
M6
M8
M10
Eiv
Mt-VPN1 (in) 1 cell
P
Y
chiasm
M1
M3
M6
M8
M10
R7 2 0 2 R8
Synapses per µm
Synapse totals
pR7 0, pR8 0, yR7 11, yR8 0

1461 Figure 5: Visual projection neurons connecting R7-8 with the central brain

1462 **A,B,E.** Synapses between R7 and R8 and MeTu (A), ML-VPN1 (B) and Mt-VPN1 (E) cells.
1463 Panels **i-iii**: Anatomy of reconstructed cells. **i**: Side view. **ii**: Top view. **iii**: Side view of medulla
1464 branches. R7 synapses are indicated in purple, R8 synapses in green in ii, iii. **iv**: Layer
1465 distribution of R7 and R8 inputs. Scale bars: 10 μm. **A**. The MeTu cell shown was fully
1466 reconstructed. Ai. Inset shows a magnified view of axon projections to the AOTU. Aiv: All
1467 seven MeTu cells were exclusively R7 targets. **B.** The ML-VPN1 cell shown was fully
1468 reconstructed. Bi. ML-VPN1 cells project to the PLP. Biv. Both ML-VPN1 cells were pale R8
1469 targets. **Ci-vi**: Light microscopy of ML-VPN1 anatomy. Ci,Cii: Side view (Ci) and top view (Cii)
1470 of the population of ML-VPN1 cells. Ciii: Side view of a single MCFO-labeled ML-VPN1 cells.
1471 Civ: Top view of multiple MCFO-labeled ML-VPN1 cells. Cv: Overlay of arbors of a single cell
1472 ML-VPN1 cell with L2 terminals (gray) indicating medulla columns. Images in Ci-Cv show
1473 overlays of aligned confocal images with the standard brain used for registration (Ci-iv) or a
1474 second registered image showing L2 terminals (Cv). Cvi: Confocal substack projection
1475 showing medulla columns at approximately the level of R8 terminals. ML-VPN1 (red) and
1476 photoreceptor axons (blue) are shown without (top) and with (bottom) labelling of yellow R8
1477 axons (Rh6 > green). Overlap between ML1 and photoreceptors is largely limited to pale
1478 columns (i.e. columns without the Rh6 marker). **Ci-vi** Scale bars: 20 μm. **D.** Reconstructions
1479 of three aMe12 cells (orange, turquoise, purple) covering the entire medulla, with axons
1480 leaving via the accessory medulla and innervating the mushroom body calyces (Calyx) and
1481 the PLP and accessory medulla (aMe) of both hemispheres. Di: Frontal view. Dii: Dorsal view.
1482 **E.** Mt-VPN1 cells. Eiv: Tracing of Mt-VPN1 photoreceptor synapses in 16 additional columns
1483 did not confirm yellow specificity found in the seed columns.

1484

Figure 5 – figure supplement 1

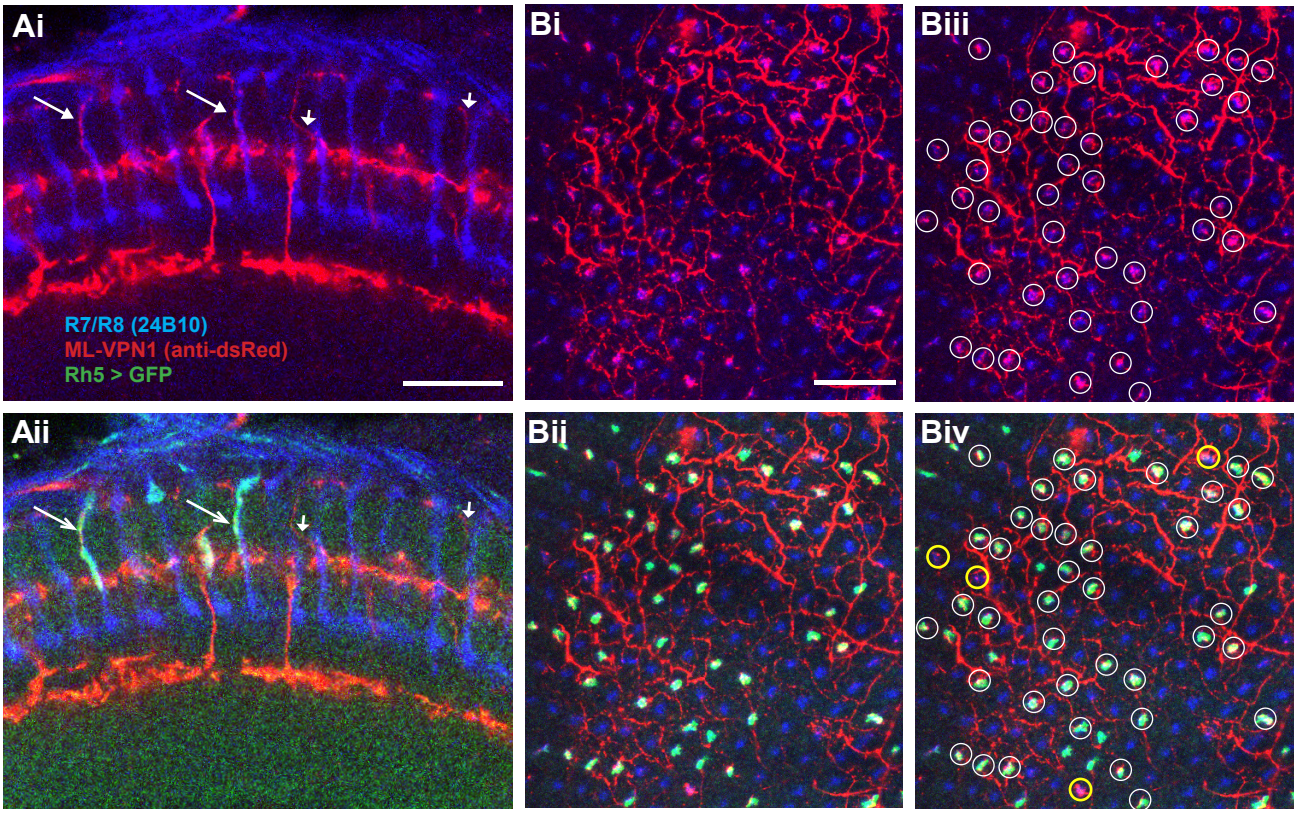

1485 Figure 5 – figure supplement 1: Pale-specificity of ML-VPN1

1486 **A**. Side view of R7 and R8 photoreceptors (blue) and ML-VPN1 cells (red), without (Ai) and
1487 with (Aii) Rh5 expression (green) , from confocal microscopy. Ai. Four vertical processes that
1488 traverse layers 1-3 are labelled by arrows; in our EM reconstructions the photoreceptor
1489 synapses were largely located on such characteristic processes (Figure 5Biii). Most vertical
1490 processes that followed photoreceptors (long arrows, left) were in pale (Rh5-positive)
1491 columns; vertical processes that did not follow photoreceptors (short arrows, right) were
1492 frequently found in yellow (Rh5-negative) columns or could not be readily assigned to a
1493 column. **B**. Projection through a few adjacent confocal slices showing ML-VPN1 and
1494 photoreceptor axons at approximately the level of R8 terminals, with color-coded image
1495 channels as in A, without (Bi) and with (Bii) pale R8 columns labelled by the Rh5 marker.
1496 Overlap between ML1 and R-cells is largely limited to pale columns. For example, out of 43
1497 putative overlaps circled (Biii), only four did not overlap with pale R8 expression (Biv, yellow
1498 thick circles), indicating that 93% of putative innervated columns were pale in this image. **A-B**
1499 Scale bars: 20 μm.

Figure 5 – figure supplement 2

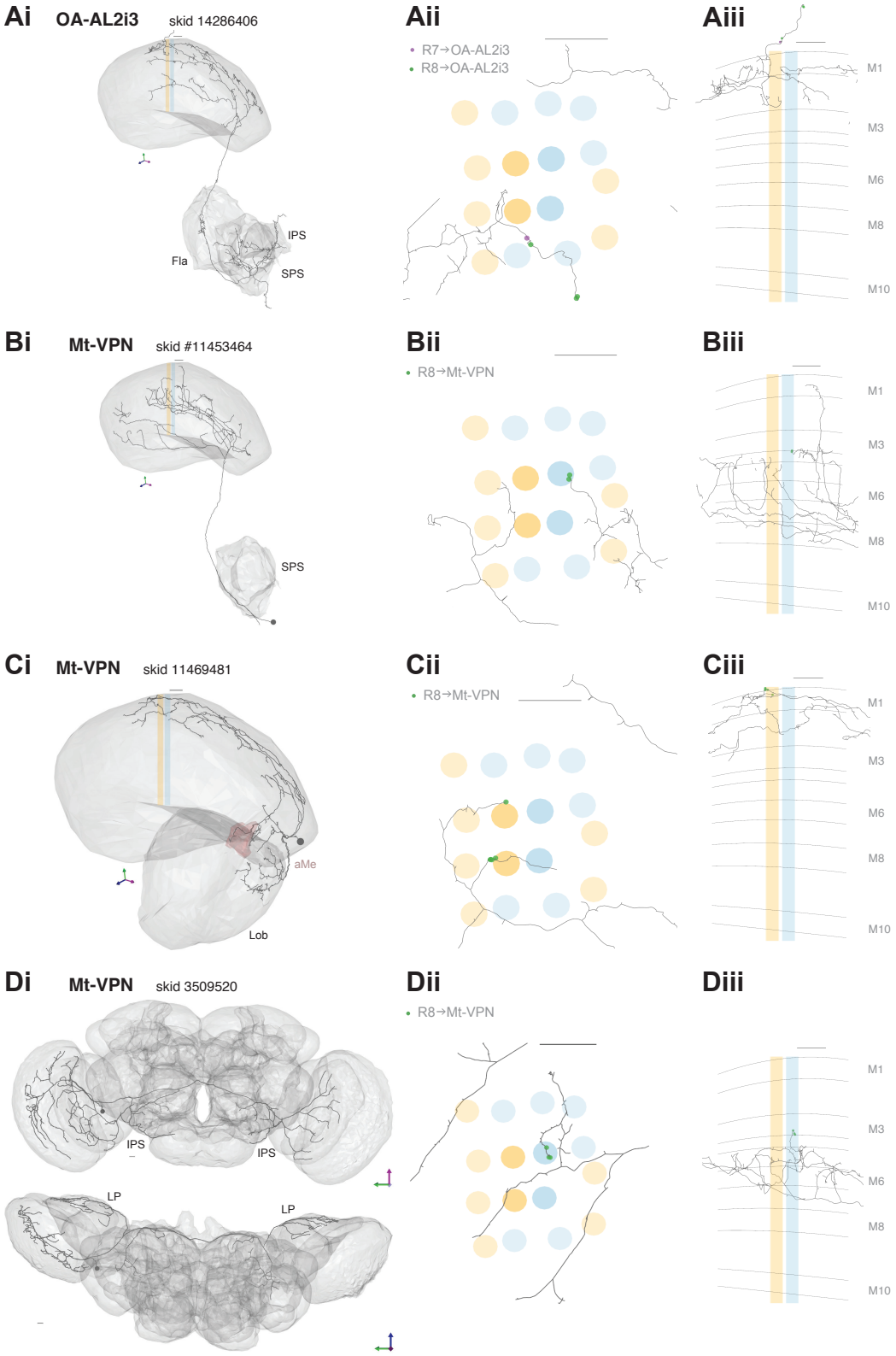

1500 Figure 5 – figure supplement 2: All additional neurons connecting R7-8 to the central brain
1501 with ≥3 synapses.
1502 **A**. R7 and R8 connections with a neuron matching the anatomy of a known octopaminergic
1503 cell type (OA-AL2i3, skid 14286406). The same reconstructed cell is shown in Ai-iii. Ai: Side
1504 view, showing the projections to the flange (Fla), inferior posterior slope (IPS), and superior
1505 posterior slope (SPS). Aii: Top view with R7 (purple) and R8 (green) synapses. Aiii: Side view
1506 with R7 (purple) and R8 (green) synapses. The cell has processes leaving the medulla that
1507 track the photoreceptors, where it received synaptic input in our seed columns. Synapse
1508 totals: 1 yellow R7, 3 yellow R8. **B.** R8 connections with the reconstructed Mt-VPN cell with
1509 skid 11453464. Bi: Side view, showing the projection to the SPS. Bii: Top view with R8 (green)
1510 synapses. Biii: Side view with R8 (green) synapses. Synapse totals: 11 yellow R7. **C.** R8
1511 connections with the reconstructed Mt-VPN cell with skid 11469481l. Ci: Side view, showing
1512 the projections to the lobula (Lob) and accessory medulla (aMe). Cii: Top view with R8 (green)
1513 synapses. Ciii: Side view with R8 (green) synapses. Synapse totals: 5 yellow R8. **D.** R8
1514 connections with the reconstructed Mt-VPN cell with skid 3509520, which is also a
1515 heterolateral lobula late tangential cell. Di: Side view, showing the projections to the lobula
1516 plate (LP) and IPS in both hemispheres. Dii: Top view with R8 (green) synapses. Diii: Side
1517 view with R8 (green) synapses. Synapse totals: 3 pale R8. **A-D.** Scale bars: 10 μm.

Figure 6

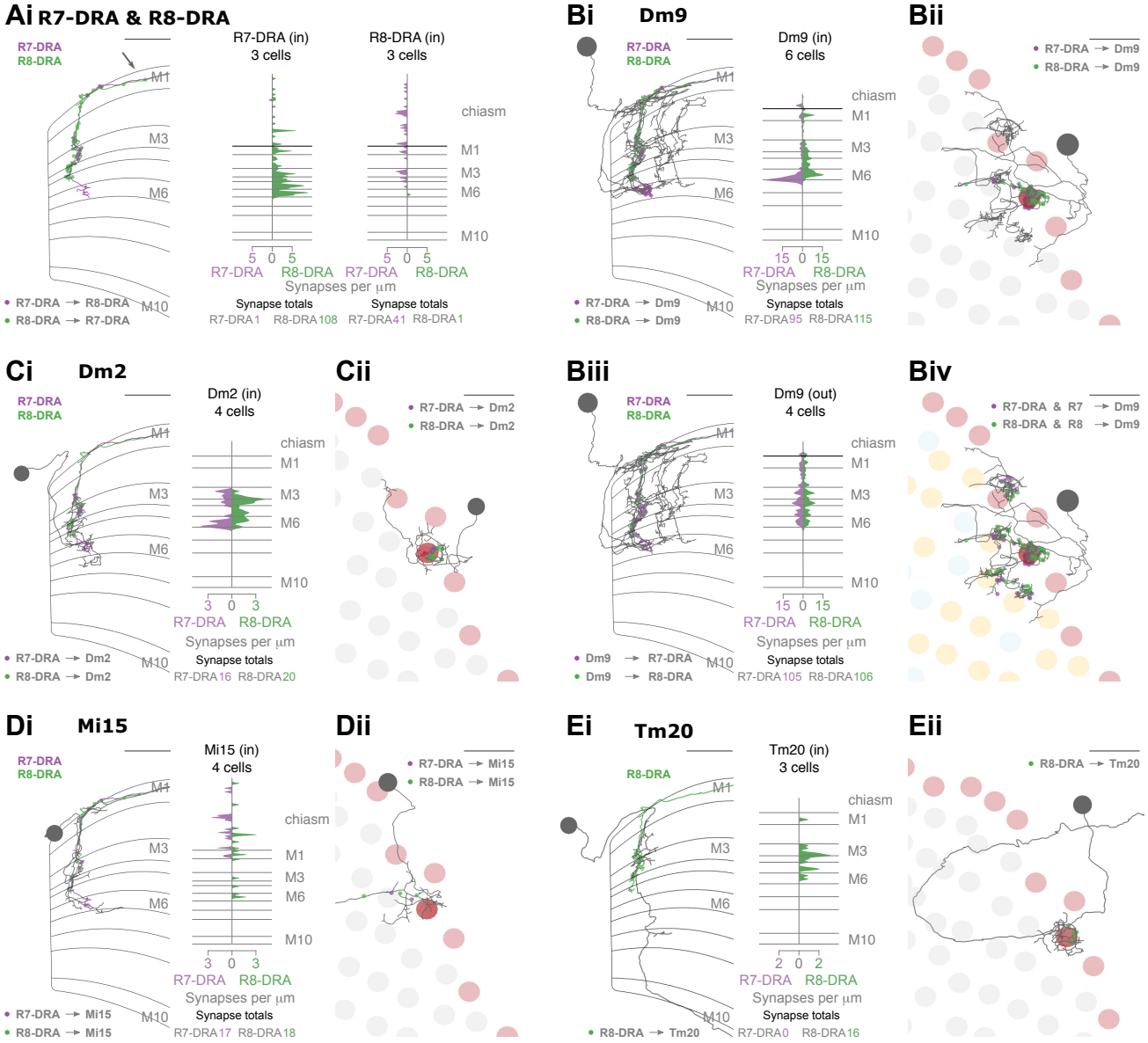
Ai R7-DRA & R8-DRA
R7-DRA
R8-DRA
R7-DRA (in)
3 cells
R8-DRA (in)
3 cells
chiasm
M1
M3
M6
M10
5 0 5
R7-DRA R8-DRA R7-DRA R8-DRA
Synapses per µm
Synapse totals
R7-DRA 1 R8-DRA 108 R7-DRA 41 R8-DRA 1
R7-DRA → R8-DRA
R8-DRA → R7-DRA
Bi Dm9
Dm9 (in)
6 cells
15 0 15
R7-DRA → Dm9
R8-DRA → Dm9
R7-DRA 95 R8-DRA 115
Bii
Ci Dm2
Dm2 (in)
4 cells
3 0 3
R7-DRA → Dm2
R8-DRA → Dm2
R7-DRA 16 R8-DRA 20
Cii
Biii
Dm9 (out)
4 cells
Dm9 → R7-DRA
Dm9 → R8-DRA
R7-DRA 105 R8-DRA 106
Biv
R7-DRA & R7 → Dm9
R8-DRA & R8 → Dm9
Di Mi15
Mi15 (in)
4 cells
R7-DRA → Mi15
R8-DRA → Mi15
R7-DRA 17 R8-DRA 18
Dii
Ei Tm20
Tm20 (in)
3 cells
2 0 2
R8-DRA → Tm20
R7-DRA 0 R8-DRA 16
Eii

1518 Figure 6: Synapses between R7-DRA and R8-DRA, and with medulla cell types

1519 **A.** Reciprocal synapses between R7-DRA and R8-DRA. Left: Side view of an R7- and R8-
1520 DRA cell with R7-DRA→R8-DRA (purple points) and R8-DRA→R7-DRA (green points Right:
1521 Layer distribution of R7-DRA and R8-DRA reciprocal synapses in three columns. **B.**
1522 Reciprocal synapses between Dm9 in the DRA region and R7-DRA and R8-DRA. Bi, Left:
1523 Side view of a reconstructed Dm9 skeleton (grey) in the DRA region, with R7-DRA→Dm9
1524 synapses (purple) and R8-DRA→Dm9 synapses (green). Right: Layer distribution of DRA
1525 photoreceptor inputs into Dm9. Bii: Top view of Dm9 cell that connects to photoreceptors in
1526 both DRA (light red) and non-DRA columns (grey). Biii, Left: Feedback synapses from Dm9
1527 to R7-DRA (purple) and R8-DRA (green). Right: Layer distribution of Dm9 inputs into R7-DRA
1528 and R8-DRA. Biv: DRA and non-DRA R7 (purple) and R8 (green) synapses to the same Dm9
1529 cell. **C.** Synapses between R7-DRA, R8-DRA and Dm2. Ci, Left: Side view of a Dm2 cell with
1530 synapses from R7-DRA (purple) and R8-DRA (green). Right: Layer distribution of R7-DRA
1531 and R8-DRA synapses onto 4 Dm2 cells. Cii: Top view of Dm2 skeleton in the DRA region. **D.**
1532 Synapses between R7-DRA, R8-DRA and Mi15. Di, Left: Side view of a reconstructed Mi15
1533 cell with R7-DRA→Mi15 synapses (purple) and R8-DRA→Mi15 synapses (green). Right:
1534 Layer distribution of R7-DRA and R8-DRA synapses to 4 Mi15 cells. Dii: Top view of Mi15
1535 skeleton in the DRA region. **E.** Synapses between R7-DRA, R8-DRA and Tm20. Ei, Left: Side
1536 view of a reconstructed Tm20 cell with R8-DRA→Tm20 synapses in green. Right: Layer
1537 distribution of R8-DRA input to 3 Tm20 cells. Eii: Top view of Tm20 skeleton in the DRA region.
1538 (All scale bars: 10 μm).

1539

Figure 6 – figure supplement 1

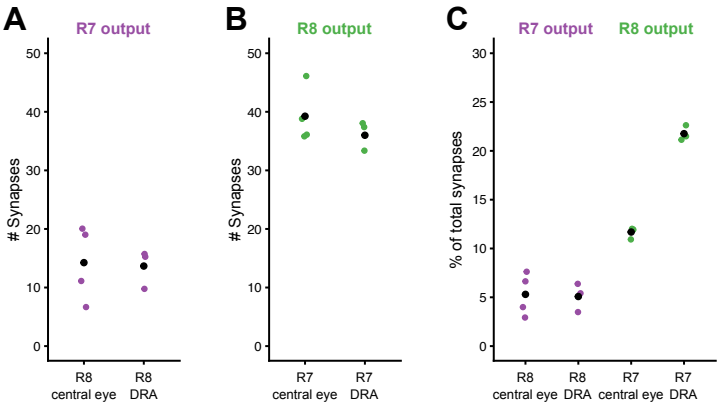

1540 Figure 6 - figure supplement 1: Synapses between inner photoreceptors in both the central
1541 and DRA columns
1542 **A**. Total number of R7 synapses onto R8 for all full reconstructed cells in the central columns
1543 (4) and R7-DRA onto R8-DRA in the DRA columns (3). **B**. Total number of R8 synapses onto
1544 R7 for all full reconstructed cells in the central columns (4) and R8-DRA onto R7-DRA in the
1545 DRA columns (3). **C**. Fraction of photoreceptor-to-photoreceptor synapses of the total output
1546 of R7 and R8 in the central columns, and of R7-DRA and R8-DRA in the DRA columns.
1547 Individual counts in colored circles mean for each group in black circle.

Figure 6 – figure supplement 2

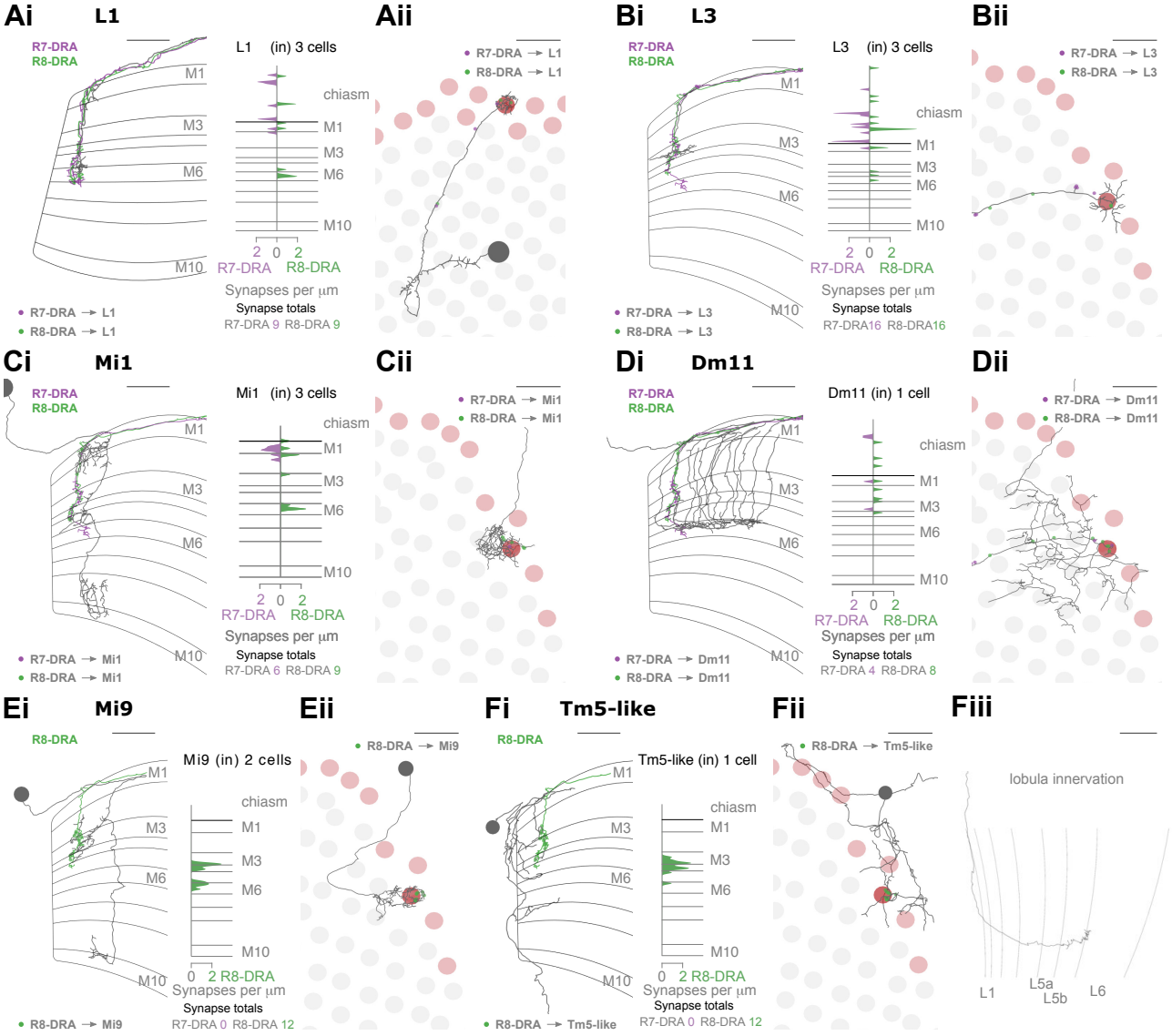

1548 Figure 6 – figure supplement 2: Additional cell types connected to R7-DRA and R8-DRA

1549 **A.** Synapses between R7-DRA, R8-DRA and L1. Ai, Left: Side view of a reconstructed L1
1550 skeleton (dark grey), together with R7-DRA (purple) and R8-DRA (green) from the same
1551 column plus R7-DRA→L1 synapses (purple) and R8-DRA→L1 synapses (green). Right:
1552 Synapse distribution (in synapses/µm) of all three reconstructed L1 cells from the three DRA
1553 seed columns across medulla layers. Aii Top view of the same L1 cell with R7-DRA→L1
1554 synapses (purple) and R8-DRA→L1 synapses (green). **B**. Synapses between R7-DRA, R8-
1555 DRA and L3. Bi, Left: Side view of a reconstructed L3 skeleton (dark grey), together with R7-
1556 DRA (purple) and R8-DRA (green) from the same column plus R7-DRA→L3 synapses
1557 (purple) and R8-DRA→L3 synapses (green). Right: Synapse distribution (in synapses/µm) of
1558 all three reconstructed L3 cells from the three DRA seed columns across medulla layers. Bii
1559 Top view of the same L3 cell with R7-DRA→L3 synapses (purple) and R8-DRA→L3 synapses
1560 (green). **C**. Synapses between R7-DRA, R8-DRA and Mi1. Ci, Left: Side view of a
1561 reconstructed Mi1 skeleton (dark grey), together with R7-DRA (purple) and R8-DRA (green)
1562 from the same column plus R7-DRA→Mi1 synapses (purple) and R8-DRA→Mi1 synapses
1563 (green). Right: Synapse distribution (in synapses/µm) of all three reconstructed Mi1 cells from
1564 the three DRA seed columns across medulla layers. Cii Top view of the same Mi1 cell with
1565 R7-DRA→Mi1 synapses (purple) and R8-DRA→Mi1 synapses (green). **D**. Synapses between
1566 R7-DRA, R8-DRA and Dm11. Di, Left: Side view of a reconstructed Dm11 skeleton (dark
1567 grey), together with R7-DRA (purple) and R8-DRA (green) plus R7-DRA→Dm11 synapses
1568 (purple) and R8-DRA→Dm11 synapses (green). Right: Synapse distribution (in synapses/µm)
1569 of one reconstructed Dm11 cell across medulla layers. Note that synapses between R7-DRA
1570 and R8-DRA→Dm11 were only found in one of the three DRA seed columns. Dii Top view of
1571 the same Dm11 cell with R7-DRA→Dm11 synapses (purple) and R8-DRA→Dm11 synapses
1572 (green). **E.** Synapses between R8-DRA and Mi9. Ei, Left: Side view of a reconstructed Mi9
1573 skeleton (dark grey), together with R8-DRA (green) from the same column plus R8-DRA→Mi9
1574 synapses (green). Right: Synapse distribution (in synapses/µm) of two reconstructed Mi9 cells

across medulla layers. Note that only in two of the three DRA seed columns R8-DRA→Mi9 synapses were found. Eii Top view of the same Mi9 cell with R8-DRA→Mi9 synapses (green). **F**. Synapses between R8-DRA and a Tm5-like cell. Fi, Left: Side view of a reconstructed Tm5-like skeleton (dark grey), together with R8-DRA (green) plus R8-DRA→ Tm5-like synapses (green). Right: Synapse distribution (in synapses/µm) of one Tm5-like cell across medulla layers. Note that in only one of the three DRA seed columns was such a cell found. Fii: Top view of the same Tm5-like cell with R8-DRA→Tm5-like synapses (green). Fiii: Lobula innervation of the Tm5-like cell.

Figure 7

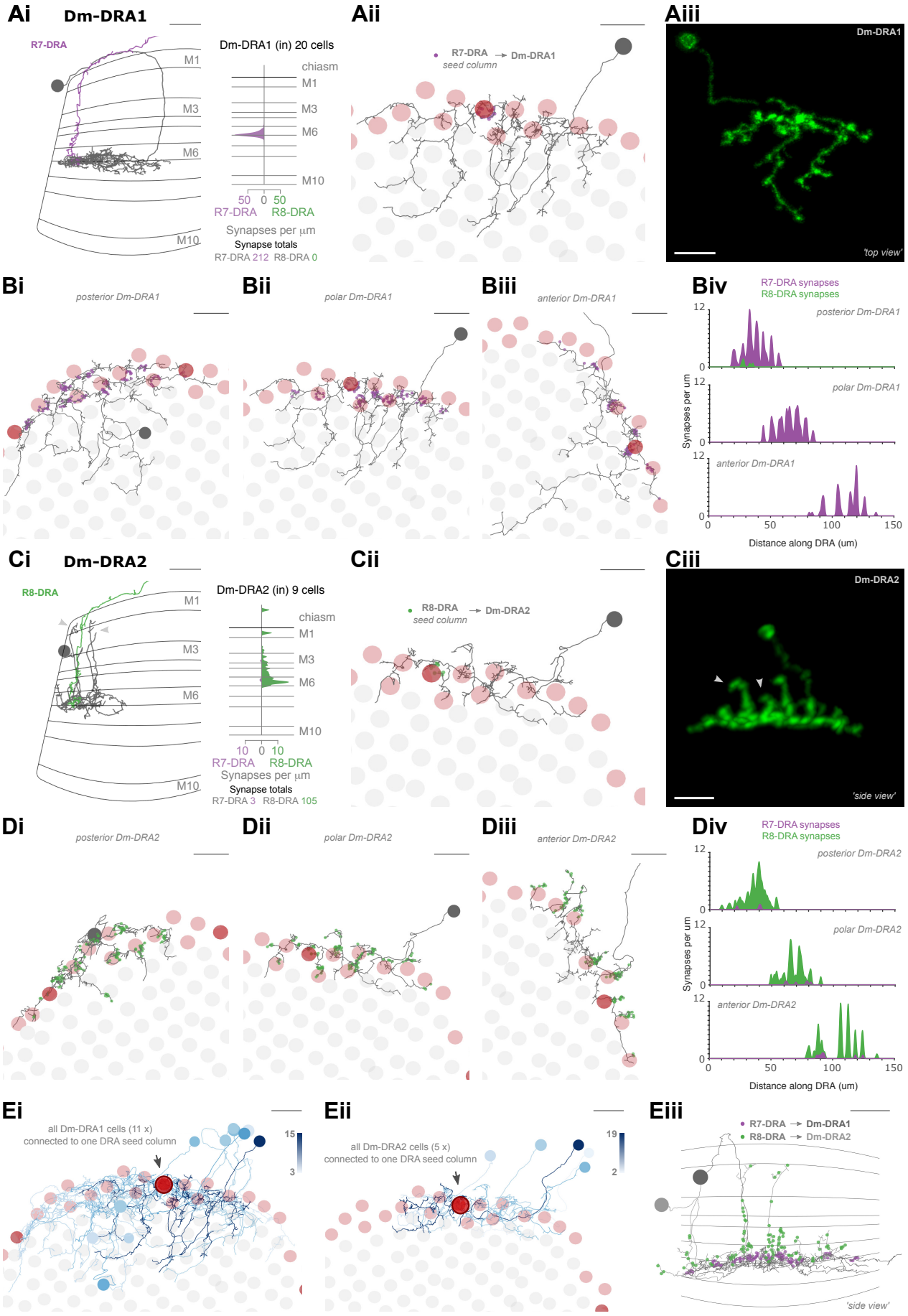
Ai
Dm-DRA1
R7-DRA
M1
M3
M6
M10
Dm-DRA1 (in) 20 cells
chiasm
50 0 50
R7-DRA R8-DRA
Synapses per µm
Synapse totals
R7-DRA 212 R8-DRA 0
Aii
R7-DRA seed column → Dm-DRA1
Aiii
Dm-DRA1
'top view'
Bi
posterior Dm-DRA1
Bii
polar Dm-DRA1
Biii
anterior Dm-DRA1
Biv
R7-DRA synapses
R8-DRA synapses
Synapses per um
Distance along DRA (um)
Ci
Dm-DRA2
R8-DRA
Dm-DRA2 (in) 9 cells
10 0 10
R7-DRA R8-DRA
Synapses per µm
Synapse totals
R7-DRA 3 R8-DRA 105
Cii
R8-DRA seed column → Dm-DRA2
Ciii
Dm-DRA2
'side view'
Di
posterior Dm-DRA2
Dii
polar Dm-DRA2
Diii
anterior Dm-DRA2
Div
Ei
all Dm-DRA1 cells (11 x) connected to one DRA seed column
Eii
all Dm-DRA2 cells (5 x) connected to one DRA seed column
Eiii
R7-DRA → Dm-DRA1
R8-DRA → Dm-DRA2
'side view'

1583 Figure 7: Dm8-like photoreceptor targets in the DRA region

1584 **A.** Synapses between photoreceptors and Dm-DRA1 cells. Ai, Left: Side view of a
1585 reconstructed Dm-DRA1 (grey) innervated by R7-DRA (purple). Right: Distribution of R7-DRA
1586 synapses (purple) onto 20 Dm-DRA1 cells, plotted across medulla layers. Aii: Top view of the
1587 same fully reconstructed Dm-DRA1 skeleton and R7-DRA inputs from the (polar) seed
1588 column. Aiii: Top view of a light microscopic Dm-DRA1 single cell clone with processes leaving
1589 the DRA region. **B.** R7-DRA inputs into Dm-DRA1 cells. Bi-iii: Three skeletons of fully
1590 reconstructed Dm-DRA1 cells (grey) at different positions along the DRA (posterior, polar and
1591 anterior) with all R7-DRA synapses (purple) originating from an average of 11 columns. Biv:
1592 Distribution of R7-DRA synapses onto the three Dm-DRA1 cells from Bi-iii along the DRA
1593 region. **C.** Synapses between photoreceptors and Dm-DRA2 cells. Ci, Left: Side view of one
1594 reconstructed Dm-DRA2 skeleton (grey) innervated by R8-DRA (green). Right: Layer
1595 distribution of DRA photoreceptor synapses onto 9 Dm-DRA2 cells. Cii: Top view of the same
1596 fully reconstructed Dm-DRA2 skeleton and photoreceptor inputs from the (polar) seed column.
1597 Ciii: Side view of a light microscopic Dm-DRA2 single cell clone with vertical processes (arrows
1598 in Ci and Ciii indicate vertical projections). **D.** Photoreceptor inputs to Dm-DRA2 cells. Di-iii:
1599 Three skeletons of fully reconstructed Dm-DRA2 cells (grey) at different positions along the
1600 DRA (posterior, polar and anterior) with all R8-DRA (green) synapses originating from an
1601 average of 11 columns. Div: Distribution of R8-DRA (and few R7-DRA) synapses onto the
1602 three Dm-DRA2 cells from Di-iii along the DRA region. **E.** Comparison of Dm-DRA1 and Dm-
1603 DRA2 connectivity. All reconstructed Dm-DRA1 skeletons connected to R7-DRA in the polar
1604 seed column (circled column, arrow). The saturation of blue color indicates strength of
1605 connectivity (from 3 to 15 synapses). Eii: All Dm-DRA2 skeletons connected to R8-DRA in the
1606 polar seed column (circled column, arrow), blue color indicates the strength of connectivity
1607 (from 2 to 19 synapses). Eiii: Side views of overlapping Dm-DRA1 and Dm-DRA2 cell
1608 skeletons with all R7-DRA and R8-DRA synapses (same cells as in Bii and Dii). (All scale
1609 bars: 10 μm).

1610

Figure 7 – figure supplement 1

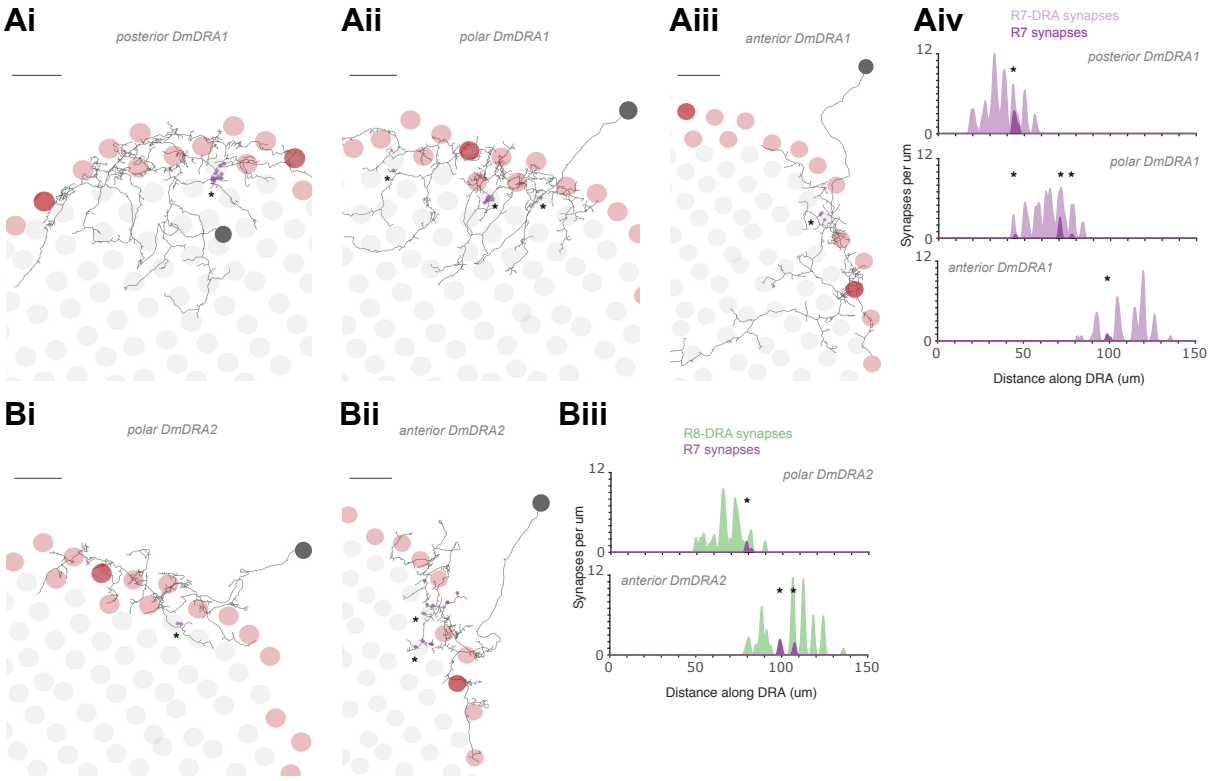

1611 Figure 7 – figure supplement 1: Non-DRA photoreceptor inputs to Dm-DRA cells

1612 **A.** Top view (Ai-Aiii) of three fully reconstructed Dm-DRA1 cells (same as in Figure 7B) with
1613 all non-DRA R7 inputs marked (purple dots), as well as distribution of synapses along the
1614 DRA region (Aiv). Note the strong inputs into the posterior Dm-DRA1 cell, originating from an
1615 R7 cell at the DRA/non-DRA boundary, with a putative 'mixed' fate (Ai). **B.** Top view (Bi-Bii)
1616 of two fully reconstructed Dm-DRA2 cells (same as in Figure 7D) with all non-DRA R7 inputs
1617 marked (purple dots), as well as distribution of synapses along the DRA region (Biii). Note that
1618 no non-DRA R7 synapses were found for the posterior Dm-DRA2.

Figure 7 – figure supplement 2

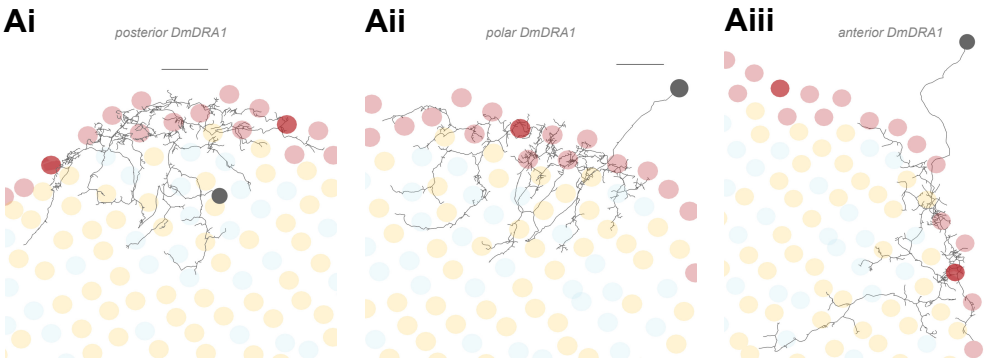

1619 Figure 7 – figure supplement 2: Deep projections of Dm-DRA1 cells

1620 **A.** Top view (Ai-Aiii) of three fully traced Dm-DRA1 cells (same as in Figure 7B) with pale and
1621 yellow fates of all non-DRA columns indicated. Deep projections of Dm-DRA1 cells do not
1622 seem to show any obvious preference for pale or yellow columns. (All scale bars: 10 μm).

Figure 7 – figure supplement 3

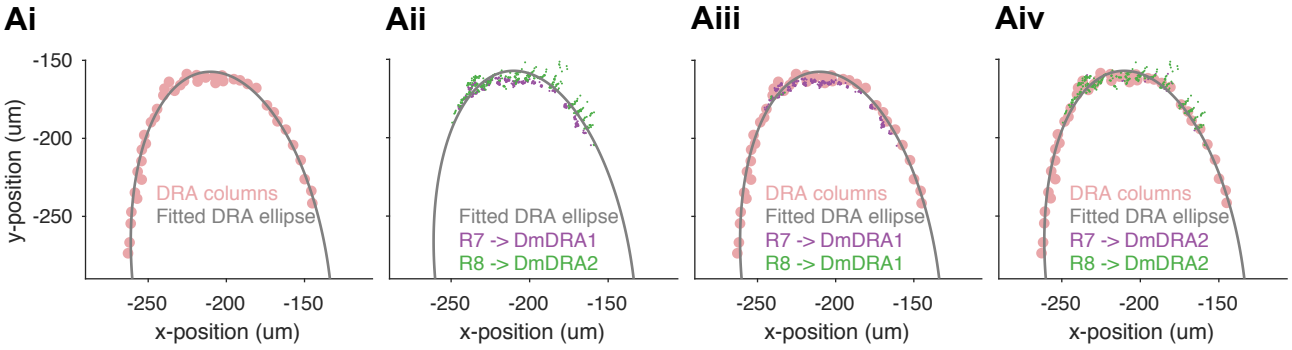

1623 Figure 7 – figure supplement 3: Fitting a linear distance of synapses along the DRA region

1624 **Ai**. The lateral locations of the 42 DRA columns (pink circles) were used to fit an ellipse (black
1625 line) along the DRA, where the lateral x- and y-coordinates are points in a plane that is
1626 approximately parallel to the medulla layers, and this plane does not take into account the
1627 curvature of the medulla. At the dorsal pole, there are DRA columns in two rows, and the
1628 ellipse passes between these. **Aii**. The alignment of R7 (purple) synapses to Dm-DRA1 cells
1629 and R8 (green) synapses to Dm-DRA2 vary along an axis that is approximately perpendicular
1630 to the ellipse, partly due to differences in the locations of the synapses, and partly an effect of
1631 the curvature of the medulla. For all the synapses, the projection onto the fitted DRA ellipse
1632 provides a good description of the location along the DRA region. **Aiii**. Synapses from R7
1633 (purple) to Dm-DRA1 cells shown with the Mi1 columns (pink circles) to appreciate their
1634 locations in the columns. The synapses are concentrated around layer 6, and this narrow
1635 depth profile generates tightly clustered synaptic locations in columns. **Aiv**. Synapses from
1636 R8 (green) to Dm-DRA2 cells shown with the DRA columns (pink circles) to appreciate their
1637 locations in the columns. The synapses are spread between the chiasm and layer 6, and this
1638 diffuse depth profile contributes to the wide, linear clusters of synapses as the medulla curves
1639 away from the plane containing the fitted DRA ellipse.

Figure 8

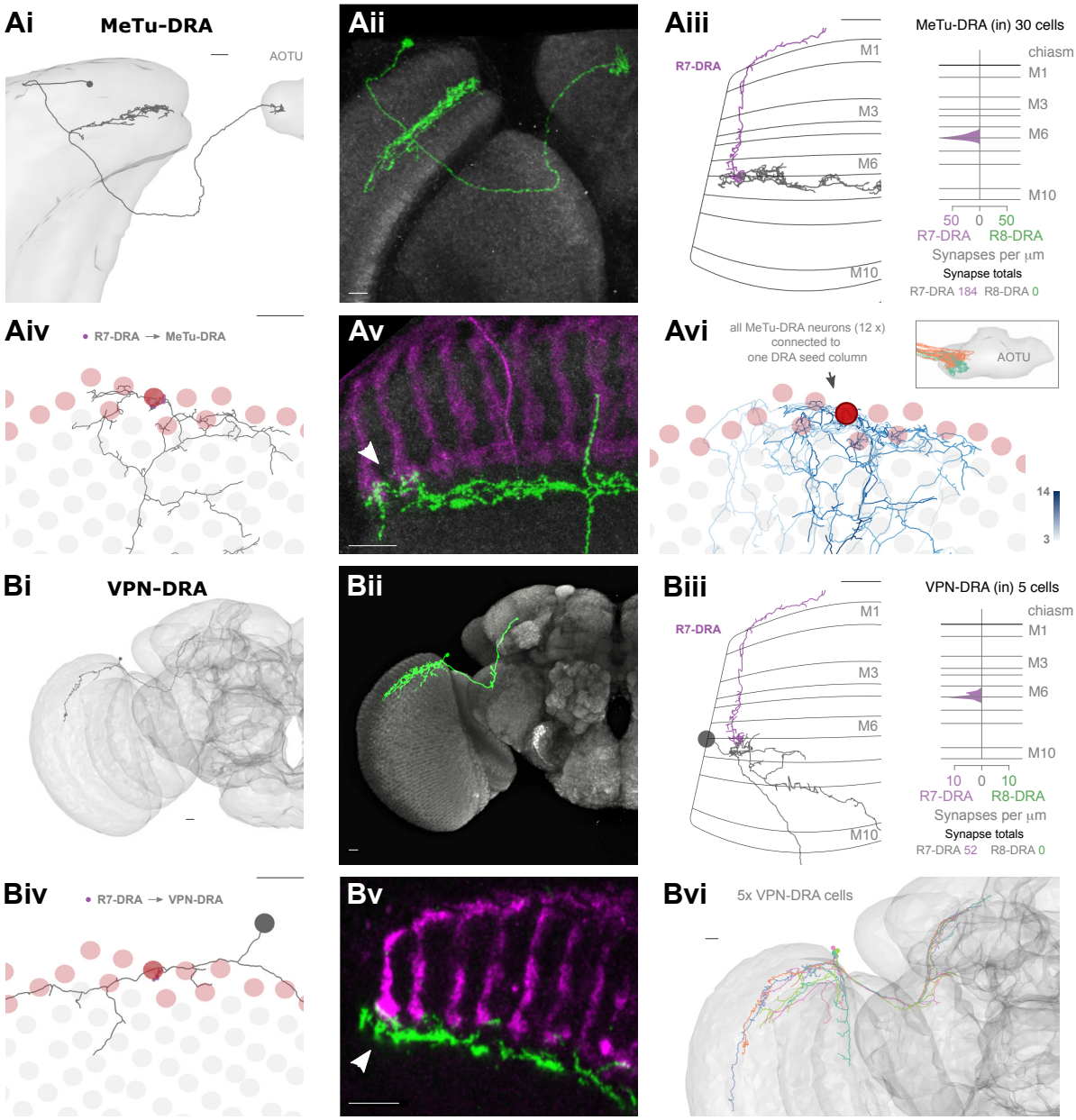
Ai
MeTu-DRA
AOTU
Aii
Aiii
R7-DRA
M1
M3
M6
M10
MeTu-DRA (in) 30 cells
chiasm
M1
M3
M6
M10
50 0 50
R7-DRA R8-DRA
Synapses per µm
Synapse totals
R7-DRA 184 R8-DRA 0
Aiv
R7-DRA → MeTu-DRA
Av
Avi
all MeTu-DRA neurons (12 x)
connected to
one DRA seed column
AOTU
14
3
Bi
VPN-DRA
Bii
Biii
R7-DRA
M1
M3
M6
M10
VPN-DRA (in) 5 cells
chiasm
M1
M3
M6
M10
10 0 10
R7-DRA R8-DRA
Synapses per µm
Synapse totals
R7-DRA 52 R8-DRA 0
Biv
R7-DRA → VPN-DRA
Bv
Bvi
5x VPN-DRA cells

1640 Figure 8: Visual projection neurons connecting R7-DRA with the central brain

1641 **A.** Synapses of R7-DRA onto MeTu-DRA cells. Ai: The complete skeleton of a fully
1642 reconstructed MeTu-DRA cell with an axon projecting to the AOTU. Aii: Light microscopic
1643 single cell clone of a MeTu-DRA cell. Aiii, Left: Side view of the same MeTu-DRA skeleton
1644 (grey) as in Ai innervated by R7-DRA (purple). Right: Layer distribution of R7-DRA synapses
1645 (purple) onto 30 MeTu-DRA cells. Aiv: Top view of the MeTu-DRA skeleton depicting its
1646 medulla processes innervating both DRA (red circles), and non-DRA columns. Avi: Light
1647 microscopic side view of a MeTu-DRA single cell clone (green) with exclusive contacts to DRA
1648 photoreceptor terminals (white arrowhead). Avi: All MeTu-DRA skeletons connected to R7-
1649 DRA in the polar seed column (circled column, arrow). The saturation of blue color indicates
1650 the strength of connectivity (from 3 to 14 synapses). Inset: MeTu-DRA axon terminations in
1651 the AOTU in orange and reconstructed MeTu cells from the central columns in cyan. **B.**
1652 Synapses between R7-DRA and visual projection neurons VPN-DRA. Bi: The entire skeleton
1653 of a reconstructed VPN-DRA cell with its axon projecting to the PLP. Bii: Light microscopic
1654 image of a VPN-DRA single cell clone shown in green and neuropil reference in grey (Nc82).
1655 Biii, Left: Side view of one VPN-DRA skeleton (grey) innervated by R7-DRA (purple). Right:
1656 Layer distribution of R7-DRA synapses onto 5 VPN-DRA cells. Biv: Top view of medulla
1657 processes formed by one reconstructed VPN-DRA skeleton (grey) with all R7-DRA synapses
1658 from the seed column (purple). Bv: Double labeling of several VPN-DRA cells (green) with R7
1659 and R8 photoreceptors (purple, anti-Chaoptin). VPN-DRA processes overlap with DRA
1660 photoreceptors (white arrowhead) but also appear to show some contacts to non-DRA
1661 photoreceptors. Bvi: Skeletons of all reconstructed VPN-DRA cells covering the dorsal
1662 medulla. (All scale bars: 10 μm).

1663

Figure 8 – figure supplement 1

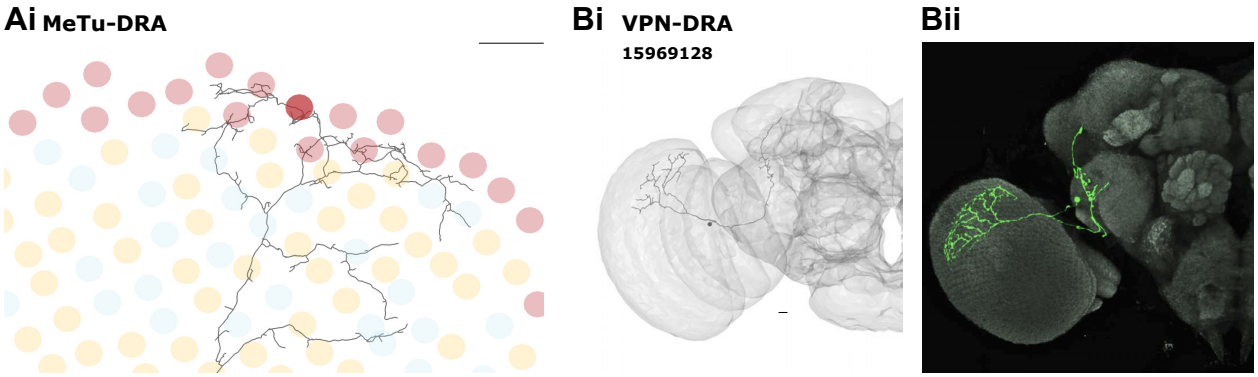

1664 Figure 8 – figure supplement 1: Visual projection neuron morphology in the DRA region

1665 **A.** Top view of the fully traced MeTu-DRA cell (same as in Figure 7A) with pale and yellow
1666 fates of all non-DRA ommatidia indicated. Medulla processes of MeTu-DRA do not seem to
1667 show any obvious preference for pale or yellow columns. Scale bar 10 µm. **B**. Reconstructed
1668 skeleton (Bi) of an unusual VPN-DRA cell with additional processes in the central brain
1669 (putative VPN-DRA2). Light microscopic image of a cell with similar morphology (Bii).

Figure 9

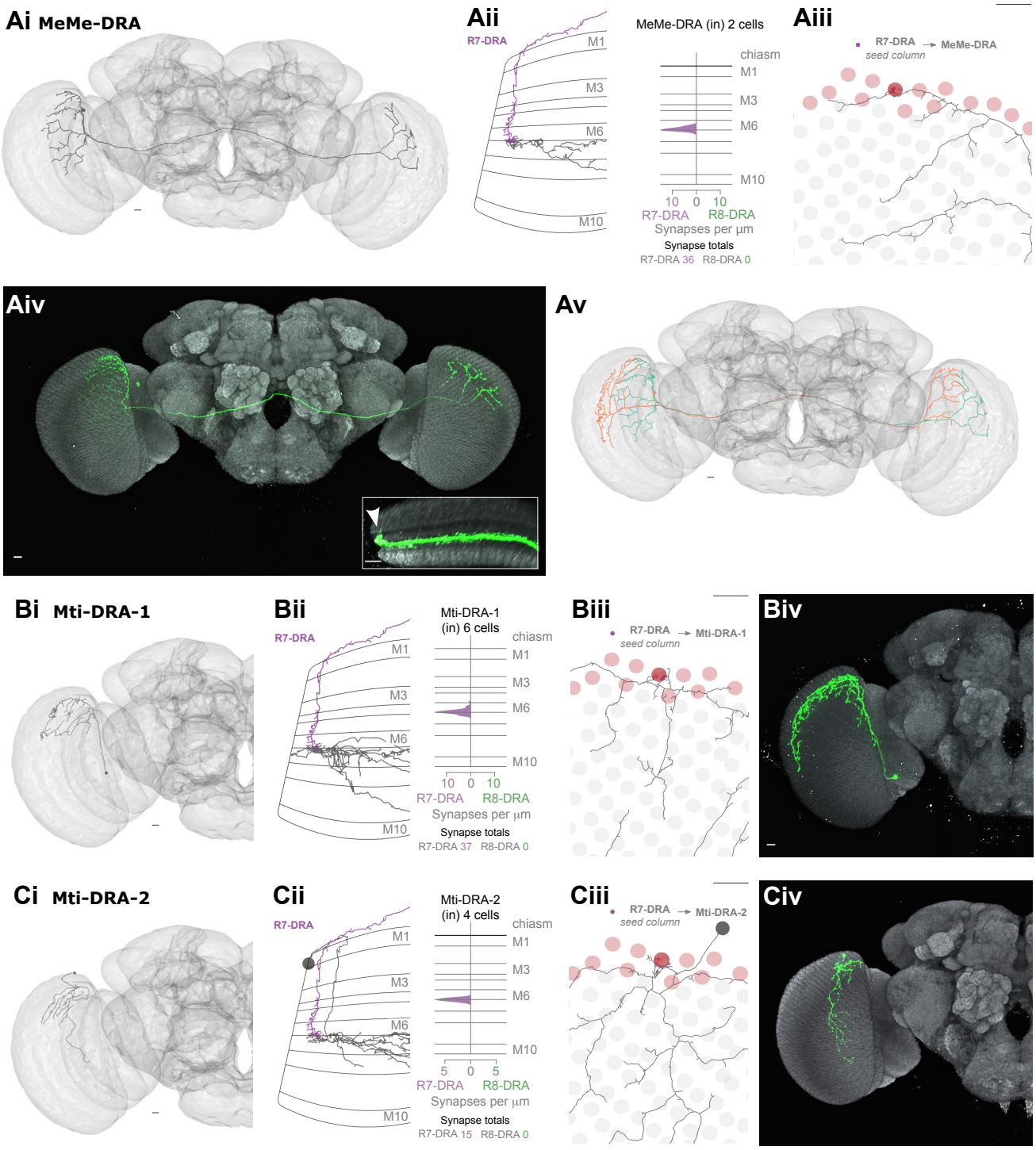
Ai MeMe-DRA
Aii
R7-DRA
M1
M3
M6
M10
MeMe-DRA (in) 2 cells
chiasm
M1
M3
M6
M10
10 0 10
R7-DRA R8-DRA
Synapses per µm
Synapse totals
R7-DRA 36 R8-DRA 0
Aiii
R7-DRA
seed column
MeMe-DRA
Aiv
Av
Bi Mti-DRA-1
Bii
R7-DRA
M1
M3
M6
M10
Mti-DRA-1
(in) 6 cells
chiasm
M1
M3
M6
M10
10 0 10
R7-DRA R8-DRA
Synapses per µm
Synapse totals
R7-DRA 37 R8-DRA 0
Biii
R7-DRA
seed column
Mti-DRA-1
Biv
Ci Mti-DRA-2
Cii
R7-DRA
M1
M3
M6
M10
Mti-DRA-2
(in) 4 cells
chiasm
M1
M3
M6
M10
5 0 5
R7-DRA R8-DRA
Synapses per µm
Synapse totals
R7-DRA 15 R8-DRA 0
Ciii
R7-DRA
seed column
Mti-DRA-2
Civ

1670 Figure 9: Other newly identified photoreceptor targets in the DRA region

1671 **A.** Synapses from R7-DRA to bilaterally projecting MeMe-DRA neurons. Ai: A reconstructed
1672 MeMe-DRA cell with projections to the dorsal periphery of the contralateral medulla. Aii, Left:
1673 Side view of one MeMe-DRA skeleton (grey) innervated by R7-DRA (purple). Right: layer
1674 distribution of R7-DRA synapses onto 2 MeMe-DRA cells. Aiii: Top view of medulla processes
1675 of the MeMe-DRA skeleton (grey) with all R7-DRA synapses from the seed columns (purple).
1676 Aiv: Light microscopic image of a MeMe-DRA single cell clone shown (in green) with
1677 processes to the contralateral medulla (neuropil reference in grey, Nc82). Inset: Medulla cross
1678 section showing branches of a MeMe-DRA cell. Note that the most dorsal arbors innervate
1679 the distal medulla (arrowhead). Av: Two reconstructed MeMe-DRA skeletons, both with cell
1680 bodies on the left-side (cyan and orange), connecting both medullas in a reciprocal manner,
1681 innervating opposite DRA regions along the anterior-posterior axis **B.** Synapses from R7-DRA
1682 onto Mti-DRA-1. Bi: A reconstructed Mti-DRA-1 cell with processes covering the dorsal
1683 periphery of the medulla. Bii, Left: Side view of one Mti-DRA-1 skeleton (grey) innervated by
1684 R7-DRA (purple). Right: Layer distribution of R7-DRA synapses onto 6 Mti-DRA-1 cells. Biii:
1685 Top view of medulla processes of one reconstructed Mti-DRA-1 cell (grey) with all R7-DRA
1686 synapses from the (polar) seed column (purple). Biv: Light microscopic image of a putative
1687 morphological single cell match of Mti-DRA-1 shown in green. C. Synapses from R7-DRA onto
1688 Mti-DRA-2. Ci: A reconstructed Mti-DRA-2 cell with processes covering dorsal parts of the
1689 medulla. Cii, Left: Side view of one Mti-DRA-2 skeleton (grey) innervated by R7-DRA (purple).
1690 Right: Layer distribution of R7-DRA synapses onto 4 Mti-DRA-2 cells. Ciii: Top view of medulla
1691 processes formed by one reconstructed Mti-DRA-2 cell (grey) with all R7-DRA synapses from
1692 the (polar) seed columns (purple). Cv: Light microscopic image of a putative morphological
1693 single cell match of Mti-DRA-2 shown in green. (All scale bars: 10 μm).

Figure 9 – figure supplement 1

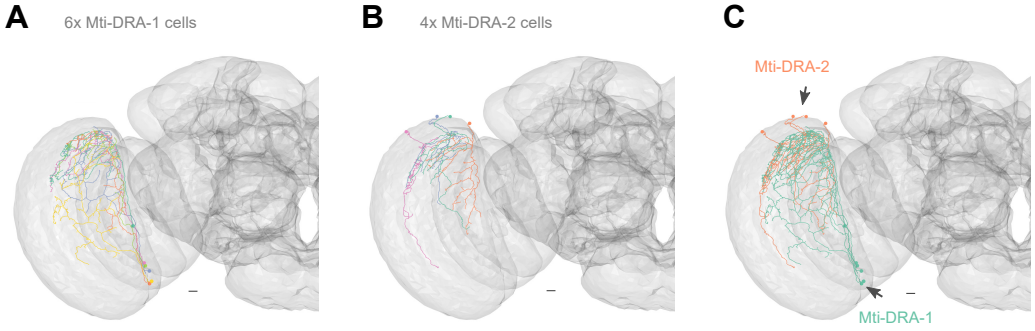

1694 Figure 9 – figure supplement 1: Mti cells in the DRA region

1695 **A**. All Mti-DRA-1 skeletons (6x) covering the dorsal medulla. **B**. All Mti-DRA-2 skeletons (4x)
1696 covering the dorsal medulla. **C**. Separation of putative Mti-DRA subtypes. One population with
1697 cell bodies located ventrally (putative cell type Mti-DRA-1, cyan, arrow), and several cells with
1698 dorsally located cell bodies (putative Mti-DRA-2, orange, arrow). (All scale bars: 10 µm).

Figure 10

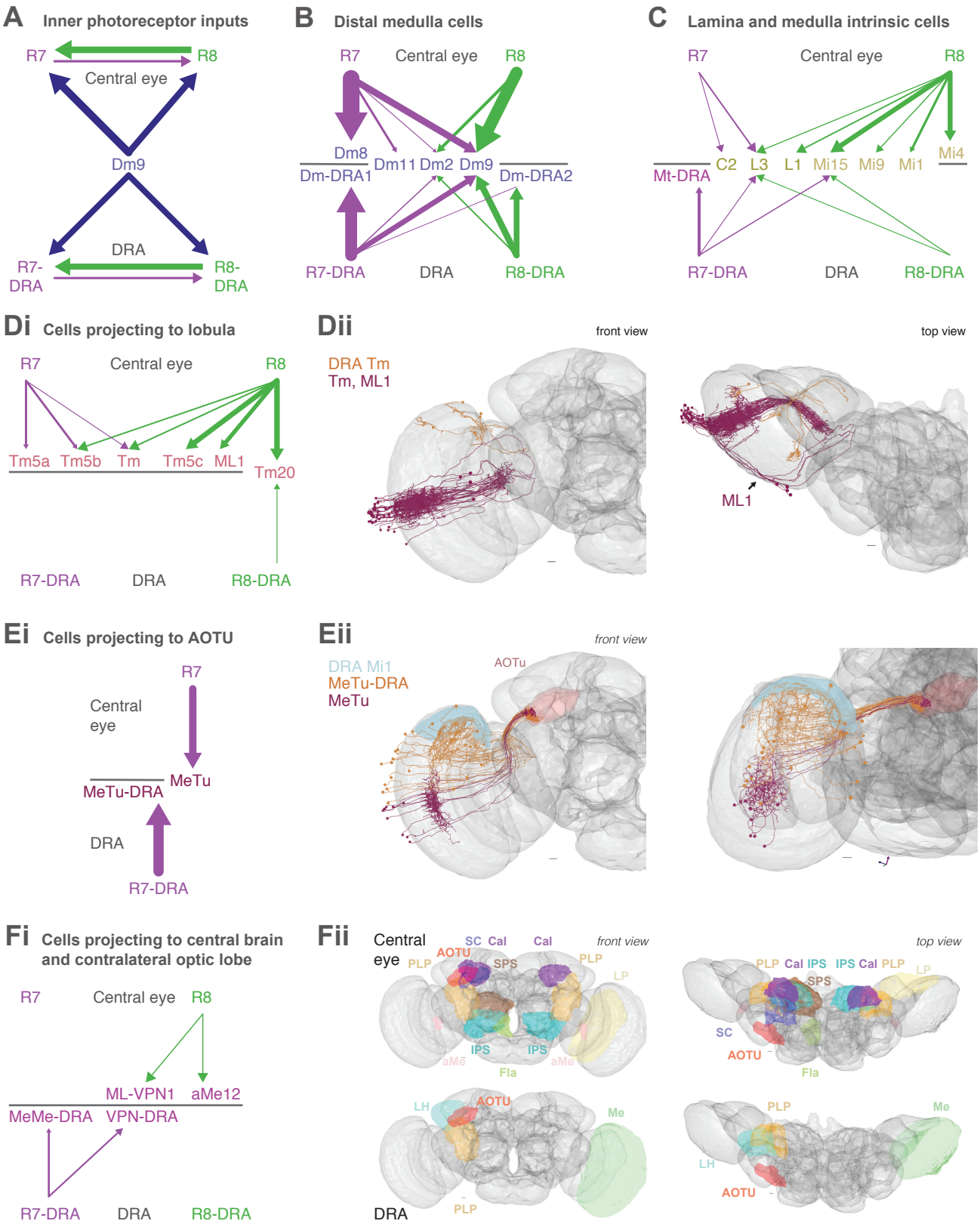
A
Inner photoreceptor inputs
R7
R8
Central eye
Dm9
DRA
R7-DRA
R8-DRA
B
Distal medulla cells
R7
Central eye
R8
Dm8
Dm11
Dm2
Dm9
Dm-DRA1
Dm-DRA2
R7-DRA
DRA
R8-DRA
C
Lamina and medulla intrinsic cells
R7
Central eye
R8
Mt-DRA
C2
L3
L1
Mi15
Mi9
Mi1
Mi4
R7-DRA
DRA
R8-DRA
Di
Cells projecting to lobula
R7
Central eye
R8
Tm5a
Tm5b
Tm
Tm5c
ML1
Tm20
R7-DRA
DRA
R8-DRA
Dii
front view
top view
DRA Tm
Tm, ML1
ML1
Ei
Cells projecting to AOTU
R7
Central eye
MeTu
MeTu-DRA
DRA
R7-DRA
Eii
front view
DRA Mi1
MeTu-DRA
MeTu
AOTu
Fi
Cells projecting to central brain and contralateral optic lobe
R7
Central eye
R8
ML-VPN1
aMe12
MeMe-DRA
VPN-DRA
R7-DRA
DRA
R8-DRA
Fii
Central eye
SC
Cal
Cal
front view
top view
AOTU
PLP
SPS
PLP
LP
IPS
IPS
aMe
Fla
PLP
Cal
IPS
IPS
Cal
PLP
LP
SPS
SC
AOTU
Fla
LH
AOTU
Me
PLP
DRA
PLP
Me
LH
AOTU

1699 Figure 10: Summary of inner photoreceptor connectivity of central and the DRA columns

1700 **A.** Schematic summary of synaptic connections between central R7-8 or R7-DRA and R8-
1701 DRA, as well as other cell types providing synaptic feedback to them (blue). In all panels of
1702 this figure, arrow widths are proportional to the numbers of synapses per seed column, and
1703 weak connections were excluded for clarity by a threshold of >4 synapses per column per
1704 photoreceptor type. Despite the differences in modality, the circuit organization of inputs to
1705 R7-8 cells is conserved in the inputs to R7-DRA and R8-DRA. **B.** Synapses between R7-8
1706 and Dm cell types in central and DRA columns. Note the presence of a second Dm8-like cell
1707 type downstream of R8 only in the DRA (Dm-DRA2). **C.** Summary of inner photoreceptor
1708 connections with lamina, Mi and Mti cells in central and DRA columns; in the central columns,
1709 the Mti connections were below the threshold of 4 synapses per column and are not shown.
1710 The connections from R8 to these cells were very reduced in the DRA. **D.** Summary of lobula
1711 connections. Di: Schematic of R7-8 versus R7-DRA and R8-DRA connections with Tm5a,
1712 Tm5b, Tm5c, Tm20, ML1 cells, and cells we identified as belonging to the Tm cell class (Tm).
1713 Note the virtual absence of lobula connectivity in the DRA region. Dii: Front view (left) and top
1714 view (right) of all reconstructed central Tm and ML1 skeletons (claret) and Tm skeletons from
1715 the DRA (orange). **E.** Summary of MeTu cell connections. Ei: Schematic of R7 and R7-DRA
1716 cells targeting different MeTu populations. Eii: Front view (left) and DRA view (right) of all
1717 central MeTu skeletons (claret) and MeTu-DRA skeletons (orange), with axons following the
1718 same tract but terminating with spatially separated axon target areas in the AOTU. **F.**
1719 Summary of other visual projection neurons. Fi: Diagram summarizing VPN connectivity in
1720 central and DRA columns. While R8 input dominates in central columns, R7 input dominates
1721 in the DRA region. Fii: Front view (left) and top view (right) of VPN target areas in the central
1722 brain. VPNs from both central and DRA columns project to the posterior lateral protocerebrum
1723 (PLP, golden yellow) and the AOTU (red). The central column VPNs additionally project
1724 ipsilaterally to the mushroom body calyx (mauve), accessory medulla (aMe, pink), superior
1725 clamp (SC, dark blue), flange (Fla, green), superior posterior slope (SPS, brown), inferior
1726 posterior slope (IPS, cyan), and contralaterally to the PLP, mushroom body calyx, aMe, and

lobula plate (LP, cream). The DRA VPNs project ipsilaterally to the AOTU, PLP, and lateral horn (LH, turquoise), and contralaterally to the medulla (Me, lime green).

Figure 11

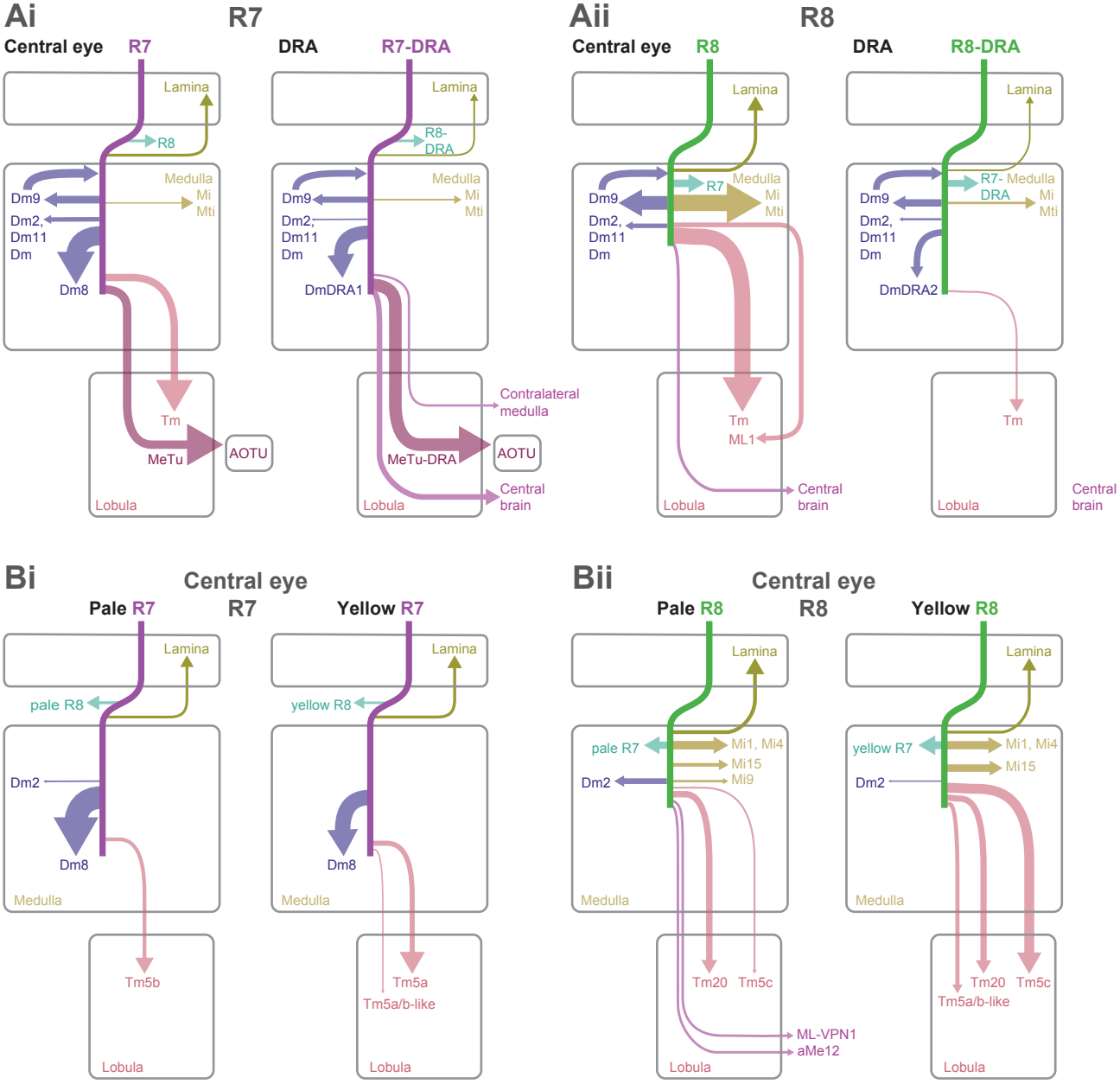
Ai
R7
Central eye
R7
DRA
R7-DRA
Lamina
R8
R8-DRA
Medulla
Mi
Mti
Dm9
Dm2,
Dm11
Dm
Dm8
DmDRA1
Tm
MeTu
AOTU
MeTu-DRA
Contralateral medulla
Central brain
Lobula
Aii
R8
Central eye
R8
DRA
R8-DRA
R7
R7- DRA
DmDRA2
ML1
Bi
Central eye
Pale R7
R7
Yellow R7
pale R8
yellow R8
Tm5b
Tm5a
Tm5a/b-like
Bii
Central eye
Pale R8
R8
Yellow R8
pale R7
yellow R7
Mi1, Mi4
Mi15
Mi9
Tm20
Tm5c
ML-VPN1
aMe12

1729 Figure 11: Comparison of central versus DRA, and pale versus yellow pathways

1730 **A.** Graphical comparison of central and DRA synaptic pathways. In all panels, the arrow widths
1731 are proportional to the numbers of synapses per seed column, and weak connections were
1732 excluded for clarity by a threshold of >4 synapses per column. Ai: Arrows indicating the relative
1733 weight of R7 connections (cell types postsynaptic to pale and yellow R7) and R7-DRA. Aii:
1734 Arrows indicating the relative weight of R8 connections (sum of pale and yellow R8) and R8-
1735 DRA region. Connections to the lobula neuropil are dominated by R8 targets in the central
1736 columns. Lobula connections are virtually absent in the DRA region (synapse numbers below
1737 1% of total synapse count), where connectivity of R8-DRA is dramatically reduced, limited to
1738 local computations in the medulla. The projections to the central brain that are not to the AOTU
1739 are driven by R8 in the central columns, but by R7-DRA in the DRA region. **B.** Graphical
1740 comparison of central pale and yellow-specific synaptic pathways. Bi: Arrows indicating the
1741 relative weight of pale R7 versus yellow R7 connections in central seed columns. Columnar
1742 cell types such as lamina cells have the capacity to preserve pale and yellow information, and
1743 Dm8 cells are most densely innervated by their home column input. Tm5a cells were selective
1744 for yellow R7, Tm5b cells were selective for pale R7, and the Tm5a-like and Tm5b-like cells
1745 were selective for yellow R8, but also received yellow R7 synapses. These diagrams omit cells
1746 such as the MeTu neurons since they receive nearly balanced input from pale and yellow R7s.
1747 Bii: Arrows indicating the relative weight of pale R8 versus yellow R8 connections in central
1748 seed columns. Columnar medulla cells that have the capacity to preserve pale and yellow
1749 information were targets of R8 cells. The aMe12 and ML-VPN1 cell types were specific for
1750 pale R8 input, while Tm5c had a strong bias for yellow R8, along with the Tm5a-like and Tm5b-
1751 like cells. ML1s are omitted from these diagrams since they received nearly balanced input
1752 from pale and yellow R8s.

Table 1: Synaptic targets of seed column R7 and R8

Type	No.	pR7	yR7	pR8	yR8	Sum	%R7	%R8	%p	%y	%Total	%Total R7	%Total R8
Dm9	6	94	66	142	143	445	36.0	64.0	53.0	47.0	16.4	13.5	18.8
Dm8	15	235	161	0	0	396	100.0	0.0	59.3	40.7	14.6	33.4	0.0
MeTu	7	82	93	0	0	175	100.0	0.0	46.9	53.1	6.5	14.7	0.0
R7	5	0	3	75	82	160	1.9	98.1	46.9	53.1	5.9	0.3	10.3
Tm5c	6	8	9	20	103	140	12.1	87.9	20.0	80.0	5.2	1.4	8.1
Tm20	4	5	3	67	65	140	5.7	94.3	51.4	48.6	5.2	0.7	8.7
Mi15	4	6	7	38	81	132	9.8	90.2	33.3	66.7	4.9	1.1	7.8
Mi4	4	0	0	58	58	116	0.0	100.0	50.0	50.0	4.3	0.0	7.6
ML1	4	0	0	58	41	99	0.0	100.0	58.6	41.4	3.7	0.0	6.5
Dm2	4	18	3	60	15	96	21.9	78.1	81.2	18.8	3.5	1.8	4.9
Dm11	2	28	27	4	4	63	87.3	12.7	50.8	49.2	2.3	4.6	0.5
L3	4	19	17	12	13	61	59.0	41.0	50.8	49.2	2.3	3.0	1.6
Mi1	4	0	0	31	28	59	0.0	100.0	52.5	47.5	2.2	0.0	3.9
R8	4	31	26	1	0	58	98.3	1.7	55.2	44.8	2.1	4.8	0.1
Tm5a	2	0	53	0	0	53	100.0	0.0	0.0	100.0	2.0	4.5	0.0
Tm5b	2	39	0	3	6	48	81.2	18.8	87.5	12.5	1.8	3.3	0.6
Tm	9	17	4	7	16	44	47.7	52.3	54.5	45.5	1.6	1.8	1.5
Tm5b-like	3	0	14	0	27	41	34.1	65.9	0.0	100.0	1.5	1.2	1.8
Mi9	4	3	9	26	1	39	30.8	69.2	74.4	25.6	1.4	1.0	1.8
L1	4	2	1	21	14	38	7.9	92.1	60.5	39.5	1.4	0.3	2.3
aMe12	2	4	0	26	0	30	13.3	86.7	100.0	0.0	1.1	0.3	1.7
Dm	5	11	7	6	5	29	62.1	37.9	58.6	41.4	1.1	1.5	0.7
ML-VPN1	3	0	0	26	1	27	0.0	100.0	96.3	3.7	1.0	0.0	1.8
C2	2	7	13	6	0	26	76.9	23.1	50.0	50.0	1.0	1.7	0.4
Mt-VPN	4	0	12	3	8	23	52.2	47.8	13.0	87.0	0.8	1.0	0.7
Mti	3	2	0	10	7	19	10.5	89.5	63.2	36.8	0.7	0.2	1.1
Tm5a-like	1	0	1	0	16	17	5.9	94.1	0.0	100.0	0.6	0.1	1.1
TmY10	1	1	0	6	0	7	14.3	85.7	100.0	0.0	0.3	0.1	0.4
Mi10	1	0	0	0	5	5	0.0	100.0	0.0	100.0	0.2	0.0	0.3
Mi	1	2	1	0	0	3	100.0	0.0	66.7	33.3	0.1	0.3	0.0
C3	1	0	0	0	3	3	0.0	100.0	0.0	100.0	0.1	0.0	0.2
Identified <3	26	5	14	14	4	37	51.4	48.6	51.4	48.6	1.4	1.6	1.2
Unidentified >=3	2	0	0	5	3	8	0.0	100.0	62.5	37.5	0.3	0.0	0.5
Unidentified <3	62	9	15	22	24	70	34.3	65.7	44.3	55.7	2.6	2.0	3.0
Total	211	628	559	747	773	2707	43.8	56.2	50.8	49.2	100.0	100.0	100.0

Table 2: Cells that synapse onto seed column R7 and R8

Type	No.	pR7	yR7	pR8	yR8	Sum	%R7	%R8	%p	%y	%Total	%Total R7	%Total R8
Dm9	6	90	92	79	72	333	54.7	45.3	50.8	49.2	57.0	51.3	65.9
R8	4	75	82	1	0	158	99.4	0.6	48.1	51.9	27.1	44.2	0.4
R7	4	0	0	31	26	57	0.0	100.0	54.4	45.6	9.8	0.0	24.9
Mt-VPN	1	0	2	0	3	5	40.0	60.0	0.0	100.0	0.9	0.6	1.3
C2	1	2	3	0	0	5	100.0	0.0	40.0	60.0	0.9	1.4	0.0
L3	1	0	0	4	0	4	0.0	100.0	100.0	0.0	0.7	0.0	1.7
Identified <3	11	4	2	4	8	18	33.3	66.7	44.4	55.6	3.1	1.7	5.2
Unidentified >=3	0	0	0	0	0	0	0.0	0.0	0.0	0.0	0.0	0.0	0.0
Unidentified <3	4	1	2	1	0	4	75.0	25.0	50.0	50.0	0.7	0.8	0.4
Total	32	172	183	120	109	584	60.8	39.2	50.0	50.0	100.0	100.0	100.0

Table 3: Synaptic targets of seed column R7-DRA and R8-DRA

Type	No.	R7-DRA	R8-DRA	Sum	%R7	%R8	%Total	%Total R7	%Total R8
Dm-DRA1	20	212	0	212	100.0	0.0	15.9	25.3	0.0
Dm9	6	95	115	210	45.2	54.8	15.7	11.3	23.0
MeTu-DRA	30	184	0	184	100.0	0.0	13.8	22.0	0.0
R7-DRA	3	1	108	109	0.9	99.1	8.2	0.1	21.6
Dm-DRA2	9	3	103	106	2.8	97.2	7.9	0.4	20.6
Dm2	4	21	27	48	43.8	56.2	3.6	2.5	5.4
R8-DRA	3	41	1	42	97.6	2.4	3.1	4.9	0.2
Mi15	4	21	18	39	53.8	46.2	2.9	2.5	3.6
Mti-DRA-1	6	37	0	37	100.0	0.0	2.8	4.4	0.0
MeMe-DRA	2	36	0	36	100.0	0.0	2.7	4.3	0.0
L3	3	16	16	32	50.0	50.0	2.4	1.9	3.2
VPN-DRA	6	30	0	30	100.0	0.0	2.2	3.6	0.0
L1	3	9	9	18	50.0	50.0	1.3	1.1	1.8
Tm20	3	0	16	16	0.0	100.0	1.2	0.0	3.2
Mti-DRA-2	4	15	0	15	100.0	0.0	1.1	1.8	0.0
Mi1	3	6	9	15	40.0	60.0	1.1	0.7	1.8
MeTu	2	13	0	13	100.0	0.0	1.0	1.6	0.0
Tm5-like	1	0	12	12	0.0	100.0	0.9	0.0	2.4
Mi9	2	0	12	12	0.0	100.0	0.9	0.0	2.4
Dm11	1	4	8	12	33.3	66.7	0.9	0.5	1.6
aMe12	1	3	1	4	75.0	25.0	0.3	0.4	0.2
TmY	1	0	3	3	0.0	100.0	0.2	0.0	0.6
ML-VPN2	1	3	0	3	100.0	0.0	0.2	0.4	0.0
C2	1	2	1	3	66.7	33.3	0.2	0.2	0.2
Identified <3	33	34	14	48	70.8	29.2	3.6	4.1	2.8
Unidentified >=3	2	5	5	10	50.0	50.0	0.7	0.6	1.0
Unidentified <3	57	46	21	67	68.7	31.3	5.0	5.5	4.2
Total	211	837	499	1336	62.6	37.4	100.0	100.0	100.0

Table 4: Cells that synapse onto seed column R7-DRA and R8-DRA

Type	No.	R7-DRA	R8-DRA	Sum	%R7	%R8	%Total	%Total R7	%Total R8
Dm9	4	105	106	211	49.8	50.2	54.7	46.1	67.1
R8-DRA	3	108	1	109	99.1	0.9	28.2	47.4	0.6
R7-DRA	3	1	41	42	2.4	97.6	10.9	0.4	25.9
C2	2	4	4	8	50.0	50.0	2.1	1.8	2.5
Mi15	1	2	2	4	50.0	50.0	1.0	0.9	1.3
Identified <3	9	6	3	9	66.7	33.3	2.3	2.6	1.9
Unidentified >=3	0	0	0	0	0.0	0.0	0.0	0.0	0.0
Unidentified <3	2	2	1	3	66.7	33.3	0.8	0.9	0.6
Total	24	228	158	386	59.1	40.9	100.0	100.0	100.0

1753 **References**

1754 Bates AS, Manton JD, Jagannathan SR, Costa M, Schlegel P, Rohlfing T, and Jefferis GS.
1755 2020. 'The natverse, a versatile toolbox for combining and analysing neuroanatomical
1756 data', *Elife*, 9:e53350.

1757 Bell ML, Earl JB, and Britt SG. 2007. 'Two types of *Drosophila* R7 photoreceptor cells are
1758 arranged randomly: a model for stochastic cell-fate determination', *J Comp Neurol*,
1759 502: 75-85.

1760 Bogovic JA, Otsuna H, Heinrich L, Ito M, Jeter J, Meissner G, Nern A, Colonell J, Malkesman
1761 O, Ito K., and Saalfeld S. 2019. 'An unbiased template of the *Drosophila* brain and
1762 ventral nerve cord': *PLoS One* 15: e0236495.

1763 Busch S, Selcho M, Ito K, and Tanimoto H.. 2009. 'A map of octopaminergic neurons in the
1764 *Drosophila* brain', *J Comp Neurol*, 513: 643-67.

1765 Chin AL, Lin CY, Fu TF, Dickson BJ, and Chiang AS. 2014. 'Diversity and wiring variability of
1766 visual local neurons in the *Drosophila* medulla M6 stratum', *J Comp Neurol*, 522: 3795-
1767 816.

1768 Chou WH, Hall KJ, Wilson DB, Wideman CL, Townson SM, Chadwell LV, and Britt SG. 1996.
1769 'Identification of a novel *Drosophila* opsin reveals specific patterning of the R7 and R8
1770 photoreceptor cells', *Neuron*, 17: 1101-15.

1771 Clements J, Dolafi T, Umayam L, Neubarth NL, Berg S, Scheffer LK, and Plaza SM. 2020.
1772 'neuPrint: Analysis Tools for EM Connectomics': *bioRxiv* 2020.01.16.909465.

1773 Courgeon M, and Desplan C. 2019. 'Coordination between stochastic and deterministic
1774 specification in the *Drosophila* visual system', *Science*, 366: eaay6727.

1775 Dacke M, and El Jundi B. 2018. 'The Dung Beetle Compass', *Curr Biol*, 28: R993-R97.

1776 Davis FP, Nern A, Picard S, Reiser MB, Rubin GM, Eddy SR, and Henry GL. 2020. 'A genetic,
1777 genomic, and computational resource for exploring neural circuit function', *Elife*, 9:
1778 e50901.

1779 Dionne H, Hibbard KL, Cavallaro A, Kao JC, and Rubin GM. 2018. 'Genetic Reagents for
1780 Making Split-GAL4 Lines in *Drosophila* ', *Genetics*, 209: 31-35.

1781 Dorkenwald S, McKellar C, Macrina T, Kemnitz N, Lee K, Lu R, Wu J, Popovych S, Mitchell
1782 E, Nehoran B, Jia Z, Bae JA, Mu S, et al. 2020. 'FlyWire: Online community for whole-
1783 brain connectomics': *bioRxiv* 2020.08.30.274225.

1784 el Jundi B, and Homberg U. 2010. 'Evidence for the possible existence of a second
1785 polarization-vision pathway in the locust brain', *J Insect Physiol*, 56: 971-9.

1786 el Jundi B, Pfeiffer K, and Homberg U. 2011. 'A distinct layer of the medulla integrates sky
1787 compass signals in the brain of an insect', *PLoS One*, 6: e27855.

1788 Feiler R, Bjornson R, Kirschfeld K, Mismer D, Rubin GM, Smith DP, Socolich M, and Zuker
1789 CS. 1992. 'Ectopic expression of ultraviolet-rhodopsins in the blue photoreceptor cells
1790 of *Drosophila*: visual physiology and photochemistry of transgenic animals', *J*
1791 *Neurosci*, 12: 3862-8.

1792 Fischbach KF, and Dittrich APM. 1989. 'The Optic Lobe of *Drosophila melanogaster* .1. A
1793 Golgi Analysis of Wild-Type Structure', *Cell Tissue Res*, 258: 441-75.

1794 Fischbach KF, and Lyly-Hunerberg I. 1983. 'Genetic dissection of the anterior optic tract of
1795 *Drosophila melanogaster*', *Cell Tissue Res*, 231: 551-63.

1796 Fortini ME, and Rubin GM. 1990. 'Analysis of Cis-Acting Requirements of the Rh3 and Rh4
1797 Genes Reveals a Bipartite Organization to Rhodopsin Promoters in *Drosophila*
1798 *melanogaster'*, *Gene Dev*, 4: 444-63.

1799 ———. 1991. 'The Optic Lobe Projection Pattern of Polarization-Sensitive Photoreceptor Cells
1800 in *Drosophila melanogaster'*, *Cell Tissue Res*, 265: 185-91.

1801 Fujita SC, Zipursky SL, Benzer S, Ferrús A, and Shotwell SL. 1982. 'Monoclonal antibodies
1802 against the *Drosophila* nervous system', *Proc Natl Acad Sci US*A, 79: 7929-33.

1803 Gao S, Takemura SY, Ting CY, Huang S, Lu Z, Luan H, Rister J, Thum AS, Yang M, Hong
1804 ST, Wang JW, Odenwald WF, White BH, Meinertzhagen IA, and Lee CH. 2008. 'The
1805 neural substrate of spectral preference in *Drosophila*', *Neuron*, 60: 328-42.

1806 Gkanias E, Risse B, Mangan M, and Webb B. 2019. 'From skylight input to behavioural output:
1807 A computational model of the insect polarised light compass', *PLoS Comput Biol*, 15:
1808 e1007123.

1809 Hardcastle BJ, Omoto JJ, Kandimalla P, Nguyen BM, Keles MF, Boyd NK, Hartenstein V, and
1810 Frye MA. 2021. 'A visual pathway for skylight polarization processing in *Drosophila*',
1811 *Elife*, 10: e63225

1812 Heath SL, Christenson MP, Oriol E, Saavedra-Weisenhaus M, Kohn JR, and Behnia R. 2020.
1813 'Circuit mechanisms underlying chromatic encoding in *Drosophila* photoreceptors'.
1814 *Curr Biol*. 30(2):264-275.e8.

1815 Heinze S. 2017. 'Unraveling the neural basis of insect navigation', *Curr Opin Insect Sci*, 24:
1816 58-67.

1817 Heisenberg M, and Buchner E. 1977. 'The role of retinula cell types in visual behavior of
1818 *Drosophila melanogaster'*, *J Comp Physiol*, 117: 127-62.

1819 Hempel de Ibarra N, Vorobyev NM, and Menzel R. 2014. 'Mechanisms, functions and ecology
1820 of colour vision in the honeybee', *J Comp Physiol A*, 200: 411-33.

1821 Hilbrant M, Almudi I, Leite DJ, Kuncheria L, Posnien N, Nunes MD, and McGregor AP. 2014.
1822 'Sexual dimorphism and natural variation within and among species in the *Drosophila*
1823 retinal mosaic', *BMC Evol Biol*, 14: 240.

1824 Homberg, U. 2015. 'Sky Compass Orientation in Desert Locusts-Evidence from Field and
1825 Laboratory Studies', *Front Behav Neurosci*, 9: 346.

1826 Huber A, Schulz S, Bentrop J, Groell C, Wolfrum U, and Paulsen R. 1997. 'Molecular cloning
1827 of *Drosophila* Rh6 rhodopsin: the visual pigment of a subset of R8 photoreceptor cells',
1828 *FEBS Lett*, 406: 6-10.

1829 Hulse BK, Haberkern H, Franconville R, Turner-Evans DB, Takemura S, Wolff T, Noorman M,
1830 Dreher M, Dan C, Parekh R, Hermundstad AN, Rubin GM, and Jayaraman V. 2020.
1831 'A connectome of the *Drosophila* central complex reveals network motifs suitable for
1832 flexible navigation and context-dependent action selection': *bioRxiv*
1833 2020.12.08.413955.

1834 Jagadish S, Barnea G, Clandinin TR, and Axel R. 2014. 'Identifying functional connections of
1835 the inner photoreceptors in *Drosophila* using Tango-Trace', *Neuron*, 83: 630-44.

1836 Jenett A, Rubin GM, Ngo TT, Shepherd D, Murphy C, Dionne H, Pfeiffer BD, Cavallaro A, Hall
1837 D, Jeter J, Iyer N, Fetter D, Hausenfluck JH, et al. 2012. 'A GAL4-driver line resource
1838 for *Drosophila* neurobiology', *Cell Rep*, 2: 991-1001.

1839 Karuppudurai T, Lin TY, Ting CY, Pursley R, Melnattur KV, Diao F, White BH, Macpherson
1840 LJ, Gallio M, Pohida T, and Lee CH. 2014. 'A hard-wired glutamatergic circuit pools

and relays UV signals to mediate spectral preference in *Drosophila*', *Neuron*, 81: 603-15.

Kind E, Belušič G, and Wernet MF. 2020. 'Retinal Mosaics Across Fly Species: Variations on a Theme.' in, *Reference Module in Neuroscience and Biobehavioral Psychology* (Elsevier).

Klapoetke NC, Murata Y, Kim SS, Pulver SR, Birdsey-Benson A, Cho YK, Morimoto TK, Chuong AS, Carpenter EJ, Tian Z, Wang J, Xie Y, Yan Z, et al. 2014. 'Independent Optical Excitement of Distinct Neural Populations', *Nat Methods*, 11: 338-346.

Konstantinides N, Kapuralin K, Fadil C, Barboza L, Satija R, and Desplan C. 2018. 'Phenotypic Convergence: Distinct Transcription Factors Regulate Common Terminal Features', *Cell*, 174: 622-35 e13.

Kurmangaliyev YZ, Yoo J, Valdes-Aleman J, Sanfilippo P, and Zipursky SL. 2020. 'Transcriptional Programs of Circuit Assembly in the *Drosophila* Visual System', *Neuron*, 108: 1045-57 e6.

Kvon EZ, Kazmar T, Stampfel G, Yanez-Cuna JO, Pagani M, Schernhuber K, Dickson BJ, and Stark A. 2014. 'Genome-scale functional characterization of *Drosophila* developmental enhancers in vivo', *Nature*, 512: 91-5.

Labhart T. 1988. 'Polarization-Opponent Interneurons in the Insect Visual-System', *Nature*, 331: 435-37.

Lazopulo S, Lazopulo A, Baker JD, and Syed S. 2019. 'Daytime colour preference in *Drosophila* depends on the circadian clock and TRP channels', *Nature*, 574: 108-11.

Li F, Lindsey JW, Marin EC, Otto N, Dreher M, Dempsey G, Stark I, Bates AS, Pleijzier MW, Schlegel P, Nern A, Takemura SY, Eckstein N, et al. 2020. 'The connectome of the adult *Drosophila* mushroom body provides insights into function', *Elife*, 9: e62576.

Li Y, Chen PJ, Lin TY, Ting CY, Muthuirulan P, Pursley R, Ilić M, Pirih P, Drews MS, Menon KP, Zinn KG, Pohida T, Borst A, and Lee CH. 2021. 'Neural mechanism of spatio-chromatic opponency in the *Drosophila* amacrine neurons', *Curr Biol*, S0960-9822(21)00615-1.

Lin TY, Luo J, Shinomiya K, Ting CY, Lu Z, Meinertzhagen IA, and Lee CH. 2016. 'Mapping chromatic pathways in the *Drosophila* visual system', *J Comp Neurol*, 524: 213-27.

Longden KD. 2016. 'Central Brain Circuitry for Color-Vision-Modulated Behaviors', *Curr Biol*, 26: R981-8.

Luo J, Ting CY, Li Y, McQueen P, Lin TY, Hsu CP, and Lee CH. 2020. 'Antagonistic regulation by insulin-like peptide and activin ensures the elaboration of appropriate dendritic field sizes of amacrine neurons', *Elife*, 9: e50568.

Mathejczyk TF, and Wernet MF. 2019. 'Heading choices of flying *Drosophila* under changing angles of polarized light', *Sci Rep*, 9: 16773.

———. 2020. 'Modular assays for the quantitative study of visually guided navigation in both flying and walking flies', *J Neurosci Methods*, 340: 108747.

Mauss AS, Vlasits A, Borst A, and Feller M. 2017. 'Visual Circuits for Direction Selectivity', *Annu Rev Neurosci*, 40: 211-30.

Mazzoni EO, Celik A, Wernet MF, Vasiliauskas D, Johnston RJ, Cook TA, Pichaud F, and Desplan C. 2008. 'Iroquois complex genes induce co-expression of rhodopsins in *Drosophila*', *PLoS Biol*, 6: e97.

1885 Meinertzhagen IA, and O'Neil SD. 1991. 'Synaptic organization of columnar elements in the
1886 lamina of the wild type in *Drosophila melanogaster*', *J Comp Neurol*, 305: 232-63.

1887 Meinertzhagen IA, Takemura SY, Lu Z, Huang S, Gao S, Ting CY, and Lee CH. 2009. 'From
1888 form to function: the ways to know a neuron', *J Neurogenet*, 23: 68-77.

1889 Meissner GW, Nern A, Singer RH, Wong AM, Malkesman O, and Long X. 2019. 'Mapping
1890 Neurotransmitter Identity in the Whole-Mount *Drosophila* Brain Using Multiplex High-
1891 Throughput Fluorescence in Situ Hybridization', *Genetics*, 211: 473-82.

1892 Melnattur KV, Pursley R, Lin TY, Ting CY, Smith PD, Pohida T, and Lee CH. 2014. 'Multiple
1893 redundant medulla projection neurons mediate color vision in *Drosophila*', *J*
1894 *Neurogenet*, 28: 374-88.

1895 Menon KP, Kulkarni V, Takemura SY, Anaya M, and Zinn K. 2019. 'Interactions between
1896 Dpr11 and DIP-gamma control selection of amacrine neurons in *Drosophila* color
1897 vision circuits', *Elife*, 8: e48935.

1898 Mollereau B, Wernet MF, Beaufils P, Killian D, Pichaud F, Kuhnlein R, and Desplan C. 2000.
1899 'A green fluorescent protein enhancer trap screen in *Drosophila* photoreceptor cells',
1900 *Mech Dev*, 93: 151-60.

1901 Morante J, and Desplan C. 2008. 'The color-vision circuit in the medulla of *Drosophila* ', *Curr*
1902 *Biol*, 18: 553-65.

1903 Mota T, Gronenberg W, Giurfa M, and Sandoz JC. 2013. 'Chromatic processing in the anterior
1904 optic tubercle of the honey bee brain', *J Neurosci*, 33: 4-16.

1905 Nern A, Pfeiffer DB, and Rubin GM. 2015. 'Optimized tools for multicolor stochastic labeling
1906 reveal diverse stereotyped cell arrangements in the fly visual system', *Proc Natl Acad*
1907 *Sci USA*, 112: E2967-76.

1908 Nilsson DE., and Warrant EJ. 1999. 'Visual discrimination: Seeing the third quality of light',
1909 *Curr Biol*, 9: R535-7.

1910 Omoto JJ, Keles MF, Nguyen BM, Bolanos C, Lovick JK, Frye MA, and Hartenstein V. 2017.
1911 'Visual Input to the *Drosophila* Central Complex by Developmentally and Functionally
1912 Distinct Neuronal Populations', *Curr Biol*, 27: 1098-110.

1913 Otsuna H, and Ito K. 2006. 'Systematic analysis of the visual projection neurons of *Drosophila*
1914 *melanogaster*. I. Lobula-specific pathways', *J Comp Neurol*, 497: 928-58.

1915 Otsuna H, Shinomiya K, and Ito K. 2014. 'Parallel neural pathways in higher visual centers of
1916 the *Drosophila* brain that mediate wavelength-specific behavior', *Front Neural Circuits*,
1917 8: 8.

1918 Ozel MN, Simon F, Jafari S, Holguera I, Chen YC, Benhra N, El-Danaf RN, Kapuralin K, Malin
1919 JA, Konstantinides N, and Desplan C. 2021. 'Neuronal diversity and convergence in a
1920 visual system developmental atlas', *Nature*, 589: 88-95.

1921 Pagni M, Haikala V, Oberhauser V, Meyer PB, Reiff DF, and Schnaitmann C. 2021.
1922 'Interaction of "chromatic" and "achromatic" circuits in *Drosophila* color opponent
1923 processing', *Curr Biol*, 31, 1687-1698.

1924 Panser K, Tirian L, Sculze F, Villalba S, Jefferis GSXE, Bühler K, and Straw AD. 2016.
1925 'Automatic Segmentation of *Drosophila* Neural Compartments Using GAL4 Expression
1926 Data Reveals Novel Visual Pathways', *Curr Biol*, 26: 1943-54.

1927 Pantazis A, Segaran A, Liu CH, Nikolaev A, Rister J, Thum AS, Roeder T, Semenov E,
1928 Juusola M, and Hardie RC. 2008. 'Distinct roles for two histamine receptors (hclA and
1929 hclB) at the *Drosophila* photoreceptor synapse', *J Neurosci*, 28: 7250-9.

1930 Papatsenko D, Sheng G, and Desplan C. 1997. 'A new rhodopsin in R8 photoreceptors of
1931 *Drosophila*: evidence for coordinate expression with Rh3 in R7 cells', *Development*,
1932 124: 1665-73.

1933 Pfeiffer BD, Jenett A, Hammonds AS, Ngo TT, Misra S, Murphy C, Scully A, Carlson JW, Wan
1934 KH, Laverty TR, Mungall C, Svirskas R, Kadonaga JT, Doe CQ, Eisen MB, Celniker
1935 SE, and Rubin GM. 2008. 'Tools for neuroanatomy and neurogenetics in *Drosophila*',
1936 *Proc Natl Acad Sci USA*, 105: 9715-20.

1937 Pfeiffer K, and Kinoshita M. 2012. 'Segregation of visual inputs from different regions of the
1938 compound eye in two parallel pathways through the anterior optic tubercle of the
1939 bumblebee (*Bombus ignitus*)', *J Comp Neurol*, 520: 212-29.

1940 Pichaud F, and Desplan C. 2001. 'A new visualization approach for identifying mutations that
1941 affect differentiation and organization of the *Drosophila* ommatidia', *Development*, 128:
1942 815-26.

1943 Pollack I, and Hofbauer A. 1991. 'Histamine-like immunoreactivity in the visual system and
1944 brain of *Drosophila melanogaster*', *Cell Tissue Res*, 266: 391-8.

1945 Rister J, and Desplan C. 2011. 'The retinal mosaics of opsin expression in invertebrates and
1946 vertebrates', *Dev Neurobiol*, 71: 1212-26.

1947 Rivera-Alba M, Vitaladevuni SN, Mishchenko Y, Lu Z, Takemura SY, Scheffer L,
1948 Meinertzhagen IA, Chklovskii DB, and de Polavieja GC. 2011. 'Wiring economy and
1949 volume exclusion determine neuronal placement in the *Drosophila* brain', *Curr Biol*,
1950 21: 2000-5.

1951 Saalfeld S, Cardona A, Hartenstein V, and Tomancak P. 2009. 'CATMAID: collaborative
1952 annotation toolkit for massive amounts of image data', *Bioinformatics*, 25: 1984-6.

1953 Salcedo E, Huber A, Henrich S, Chadwell LV, Chou WH, Paulsen R, and Britt SG. 1999. 'Blue-
1954 and green-absorbing visual pigments of *Drosophila*: ectopic expression and
1955 physiological characterization of the R8 photoreceptor cell-specific Rh5 and Rh6
1956 rhodopsins', *J Neurosci*, 19: 10716-26.

1957 Sancer G, Kind E, Plazaola-Sasieta H, Balke J, Pham T, Hasan A, Munch LO, Courgeon M,
1958 Mathejczyk TF, and Wernet MF. 2019. 'Modality-Specific Circuits for Skylight
1959 Orientation in the Fly Visual System', *Curr Biol* 29: 2812-2825.e4.

1960 Sancer G, Kind E, Uhlhorn J, Volkmann J, Hammacher J, Pham T, Plazaola-Sasieta H, and
1961 Wernet MF. 2020. 'Cellular and synaptic adaptations of neural circuits processing
1962 skylight polarization in the fly', *J Comp Physiol A*, 206: 233-46.

1963 Sancer G, and Wernet MF. 2021. 'The development and function of neuronal subtypes
1964 processing color and skylight polarization in the optic lobes of *Drosophila*
1965 *melanogaster*', *Arthropod Struct Dev*, 61: 101012.

1966 Scheffer LK, Xu CS, Januszewski M, Lu Z, Takemura SY, Hayworth KJ, Huang GB, Shinomiya
1967 K, Maitin-Shepard J, Berg S, Clements J, Hubbard P, Katz W, et al. 'A Connectome
1968 and Analysis of the Adult *Drosophila* Central Brain', *eLife* 9: e57443.

1969 Schnaitmann C, Garbers C, Wachtler T, and Tanimoto H. 2013. 'Color discrimination with
1970 broadband photoreceptors', *Curr Biol*, 23: 2375-82.

1971 Schnaitmann C, Haikala V, Abraham E, Oberhauser V, Thestrup T, Griesbeck O, and Reiff
1972 DF. 2018. 'Color Processing in the Early Visual System of *Drosophila*', *Cell*, 172: 318-
1973 30 e18.

Schneider-Mizell CM, Gerhard S, Longair M, Kazimiers T, Li F, Zwart MF, Champion A, Midgley FM, Fetter RD, Saalfeld S, and Cardona A. 2016. 'Quantitative neuroanatomy for connectomics in *Drosophila* ', *Elife*, 5: e12059.

Sharkey CR, Blanco J, Leibowitz MM, Pinto-Benito D, and Wardill TJ. 2020. 'The spectral sensitivity of *Drosophila* photoreceptors', *Sci Rep*, 10: 18242.

Shinomiya K, Karuppudurai T, Lin TY, Lu Z, Lee CH, and Meinertzhagen IA. 2014. 'Candidate neural substrates for off-edge motion detection in *Drosophila*', *Curr Biol*, 24: 1062-70.

Silies MD, Gohl M, Fisher YE, Freifeld L, Clark DA, and Clandinin TR. 2013. 'Modular use of peripheral input channels tunes motion-detecting circuitry', *Neuron*, 79: 111-27.

Strother JA, Wu ST, Wong AM, Nern A, Rogers EM, Le JQ, Rubin GM, and Reiser MB. 2017. 'The Emergence of Directional Selectivity in the Visual Motion Pathway of *Drosophila*', *Neuron*, 94: 168-82 e10.

Tahayato A, Sonneville R, Pichaud F, Wernet MF, Papatsenko D, Beaufils P, Cook T, and Desplan C. 2003. 'Otd/Crx, a dual regulator for the specification of ommatidia subtypes in the *Drosophila* retina', *Dev Cell*, 5: 391-402.

Tai CY, Chin AL, and Chiang AS. 2021. 'Comprehensive map of visual projection neurons for processing ultraviolet information in the *Drosophila* brain', *J Comp Neurol*, 529: 1988-2013.

Takemura S, Bharioke A, Lu ZY, Nern A, Vitaladevuni S, Rivlin PK, Katz WT, Olbris DJ, Plaza SM, Winston P, Zhao T, Horne JA, Fetter RD, et al. 2013. 'A visual motion detection circuit suggested by *Drosophila* connectomics', *Nature*, 500: 175-181.

Takemura SY, Lu ZY, and Meinertzhagen IA. 2008. 'Synaptic circuits of the *Drosophila* optic lobe: The input terminals to the medulla', *J Comp Neurol*, 509: 493-513.

Takemura SY, Nern A, Chklovskii DB, Scheffer LK, Rubin GM, and Meinertzhagen IA. 2017. 'The comprehensive connectome of a neural substrate for 'ON' motion detection in *Drosophila*', *Elife*, 6: e24394.

Takemura SY, Xu CS, Lu Z, Rivlin PK, Parag T, Olbris DJ, Plaza S, Zhao T, Katz WT, Umayam L, Weaver C, Hess HF, Horne JA, et al. 2015. 'Synaptic circuits and their variations within different columns in the visual system of *Drosophila* ', *Proc Natl Acad Sci USA*, 112: 13711-6.

Timaeus L, Geid L, Sancer G, Wernet MF, and Hummel T. 2020. 'Parallel visual pathways with topographic versus non-topographic organization connect the *Drosophila* eyes to the central brain', *bioRxiv*: 2020.04.11.037333.

Tirian L, and Dickson BJ. 2017. 'The VT GAL4, LexA, and split-GAL4 driver line collections for targeted expression in the *Drosophila* nervous system': *bioRxiv* 198648.

Tuthill JC, Nern A, Holtz SL, Rubin GM, and Reiser MB. 2013. 'Contributions of the 12 neuron classes in the fly lamina to motion vision', *Neuron*, 79: 128-40.

Uhlhorn J, and Wernet MF. 2020. 'Colour Vision: Self-Centered Fly Photoreceptors Communicate over Distances', *Curr Biol*, 30: R78-R81.

Vogt K, Schnaitmann C, Dylla KV, Knapek S, Aso Y, Rubin GM, and Tanimoto H. 2014. 'Shared mushroom body circuits underlie visual and olfactory memories in *Drosophila*', *Elife*. 3: e02395.

Wada S. 1974a. 'Special Marginal Ommatidia of Flies (Diptera-Brachycera) - Architecture and Distribution in Compound Eyes', *Z Morphol Tiere*, 77: 87-125.

———. 1974b. 'Spezielle randzonale ommatidien von Calliphora Erythrocephala meig. (diptera calliphoridae): Architektur der zentralen rhabdomeren-kolumne und topographie im komplexauge', *Int J Insect Morphol*, 3: 397-424.

Wagh DA, Rasse TM, Asan E, Hofbauer A, Schwenkert I, Dürrbeck H, Buchner S, Dabauvalle MC, Schmidt M, Qin G, Wichmann C, Kittel R, Sigrist SJ, Buchner E. 2006. 'Bruchpilot, a protein with homology to ELKS/CAST, is required for structural integrity and function of synaptic active zones in *Drosophila*', *Neuron*, 49: 833-44.

Wardill TJ, List O, Li X, Dongre S, McCulloch M, Ting CY, O'Kane CJ, Tang S, Lee CH, Hardie RC, and Juusola M. 2012. 'Multiple spectral inputs improve motion discrimination in the *Drosophila* visual system', *Science*, 336: 925-31.

Warren TL., Weir PT, and Dickinson MH. 2018. 'Flying *Drosophila melanogaster* maintain arbitrary but stable headings relative to the angle of polarized light', *J Exp Biol*, 221.

Wehner R, and Muller M. 1985. 'Does Interocular Transfer Occur in Visual Navigation by Ants', *Nature*, 315: 228-29.

Weir PT, and Dickinson MH. 2012. 'Flying *Drosophila* Orient to Sky Polarization', *Current Biology*, 22: 21-27.

Weir PT, Henze MJ, Bleul C, Baumann-Klausener F, Labhart T, and Dickinson MH. 2016. 'Anatomical Reconstruction and Functional Imaging Reveal an Ordered Array of Skylight Polarization Detectors in *Drosophila* ', *J Neurosci*, 36: 5397-404.

Wernet MF, Huberman AD, and Desplan C. 2014. 'So many pieces, one puzzle: cell type specification and visual circuitry in flies and mice', *Genes Dev*, 28: 2565-84.

Wernet MF, Labhart T, Baumann F, Mazzoni EO, Pichaud F, and Desplan C. 2003. 'Homothorax switches function of *Drosophila* photoreceptors from color to polarized light sensors', *Cell*, 115: 267-79.

Wernet MF, Perry MW, and Desplan C. 2015. 'The evolutionary diversity of insect retinal mosaics: common design principles and emerging molecular logic', *Trends Genet*, 31: 316-28.

Wernet MF, Velez MM, Clark DA, Baumann-Klausener F, Brown JR, Klovstad M, Labhart T, and Clandinin TR. 2012. 'Genetic dissection reveals two separate retinal substrates for polarization vision in *Drosophila* ', *Curr Biol*, 22: 12-20.

Wu M, Nern A, Williamson WR, Morimoto MM, Reiser MB, Card GM, and Rubin GM. 2016. 'Visual projection neurons in the *Drosophila* lobula link feature detection to distinct behavioral programs', *Elife*, 5: e21022.

Yamaguchi S, Wolf R, Desplan C, and Heisenberg M. 2008. 'Motion vision is independent of color in *Drosophila*', *Proc Natl Acad Sci USA*, 105: 4910-5.

Zheng Z, Lauritzen JS, Perlman E, Robinson CG, Nichols M, Milkie D, Torrens O, Price J, Fisher CB, Sharifi N, Calle-Schuler SA, Kmecova L, Ali IJ, et al. 2018. 'A Complete Electron Microscopy Volume of the Brain of Adult *Drosophila melanogaster*', *Cell*, 174: 730-43 e22.